Electrical manipulation of a single electron spin in CMOS using a micromagnet and spin-valley coupling

Bernhard Klemt

THÈSE

Pour obtenir le grade de

DOCTEUR DE L'UNIVERSITÉ GRENOBLE ALPES

École doctorale : PHYS - Physique
Spécialité : Physique de la Matière Condensée et du Rayonnement
Unité de recherche : Institut Néel

Manipulation électrique d'un spin d'électron unique dans CMOS à l'aide d'un micro-aimant et d'un couplage spin-vallée

Electrical manipulation of a single electron spin in CMOS using a micromagnet and spin-valley coupling

Présentée par :

Bernhard KLEMT

Direction de thèse :

Tristan MEUNIER DIRECTEUR DE RECHERCHE, CNRS DELEGATION ALPES	Directeur de thèse

Rapporteurs :

TAKIS KONTOS
DIRECTEUR DE RECHERCHE, CNRS DELEGATION PARIS CENTRE
DOMINIQUE BOUGEARD
PROFESSEUR, UNIVERSITÄT REGENSBURG

Thèse soutenue publiquement le **24 novembre 2023**, devant le jury composé de :

TAKIS KONTOS DIRECTEUR DE RECHERCHE, CNRS DELEGATION PARIS CENTRE	Rapporteur
DOMINIQUE BOUGEARD PROFESSEUR, UNIVERSITÄT REGENSBURG	Rapporteur
PHILIPPE GALY INGENIEUR HDR, ST MICROELECTRONICS	Examinateur
ANASUA CHATTERJEE ASSOCIATE PROFESSOR, KØBENHAVNS UNIVERSITET	Examinatrice
MAIRBEK CHSHIEV PROFESSEUR DES UNIVERSITES, UNIVERSITE GRENOBLE ALPES	Président

Invités :

MATIAS URDAMPILLETA
CHARGE DE RECHERCHE, CNRS DELEGATION ALPES

Abstract

Recent advances in quantum information gave a small insight into the potential quantum computing offers. To unveil the full power of a universal quantum computer however, millions of interconnected qubits are necessary. In this context, leveraging complementary metal-oxide-semiconductor (CMOS) technology that made the integration of billions of transistors in classical computers possible seems natural. Semiconductor spin qubits show long coherence times, high gate fidelities and they can be integrated using CMOS technology, which makes them an ideal candidate for reliable and scalable fabrication. The direct leap from academic fabrication to qubits fabricated fully by industrial CMOS standards is difficult to make without intermediate solutions. The fabrication and characterization of such intermediate solutions is at the heart of this thesis.

First, the material properties relevant for qubit use at low temperatures of an industrial fully depleted silicon-on-insulator (FD-SOI) wafer are studied. Hall bars and quantum dot structures made by academic fabrication are used for characterization. From Hall measurements at 400 mK, a percolation density of around $1\times10^{12}\,\mathrm{cm}^{-2,}$ is extracted. A peak mobility of $(2350 \pm 20)\,\mathrm{cm}^2/\mathrm{Vs}$ is reached at a density of $(3.48 \pm 0.05)\times10^{12}\,\mathrm{cm}^{-2}$, most likely limited by the oxide thickness.

In a second step, a flexible back-end-of-line (BEOL) is introduced. It allows for new functionalities such as micro-magnets or superconducting circuits that can be added in a post-CMOS process to study the physics of these devices or achieve proof of concepts with the goal to incorporate the established process in the foundry-compatible process flow. In this thesis, a single electron spin qubit in a CMOS device with a micro-magnet integrated in the flexible BEOL is studied. Relaxometry reveals a valley-splitting in the order of 60 µeV and long spin relaxation times around 400 ms. Coherent oscillations using electric dipole spin resonance (EDSR) of a single electron spin with Rabi frequencies around 1 MHz are observed. The shape of the Rabi oscillations indicates that the coherence is limited by low frequency noise originating from the remaining nuclear spins in the natural Si channel. The synthetic spin-orbit coupling (SOC) is exploited to control the qubit via electric fields and investigate the spin-valley physics in the presence of SOC where an enhancement of the Rabi frequency is shown at the spin-valley hotspot.

Finally, the high frequency noise in the system is probed using dynamical decoupling pulse sequences and charge noise is found to dominate the qubit decoherence in this range.

The work presented in this thesis provides first experimental evidence for valley enhanced EDSR and demonstrates an electron spin qubit on a FD-SOI substrate for the first time. The qubit performance is comparable to early spin qubit realizations on other material systems. The introduction of ^{28}Si is expected to greatly improve the coherence properties and valley enhanced EDSR may enable faster driving speeds for improved qubit quality.

Abstract - Français

Les récentes avancées dans le domaine de l'information quantique ont donné un bel aperçu du potentiel qu'offre l'informatique quantique. Cependant, pour révéler toute la puissance d'un ordinateur quantique universel, des millions de qubits interconnectés sont nécessaires. Dans ce contexte, il semble naturel d'utiliser de la technologie complementary metal-oxide-semiconductor (CMOS) qui a rendu possible l'intégration de milliards de transistors dans les ordinateurs classiques. Les qubits de spin semi-conducteurs présentent de longs temps de cohérence, des fidélités élevées et peuvent être intégrés à l'aide de la technologie CMOS, ce qui en fait un candidat idéal pour une fabrication fiable et à large échelle. Il est difficile de passer directement d'une fabrication académique à des qubits entièrement fabriqués selon les normes CMOS industrielles sans solutions intermédiaires. La fabrication et la caractérisation de ces solutions intermédiaires sont donc au cœur de cette thèse.
Tout d'abord, les propriétés matérielles pertinentes pour l'utilisation de qubits à basse température des dispositifs industrielle à base de fully depleted silicon-on-insulator (FD-SOI) sont étudiées. Les barres de Hall et les structures des boîtes quantiques sont utilisées pour la caractérisation. Des mesures de Hall à 400 mK, une densité de percolation d'environ $1\times10^{12}\,\mathrm{cm}^{-2,}$ est extraite. Une mobilité maximale de $2351\,\mathrm{cm}^2/\mathrm{Vs}$ est atteinte à une densité de $(3.48 \pm 0.05)\times10^{12}\,\mathrm{cm}^{-2}$, probablement limitée par l'épaisseur de l'oxyde.
Ensuite, un back-end-of-line (BEOL) flexible est introduit. Il permet de nouvelles fonctionnalités telles que des micro-aimants ou des circuits supraconducteurs qui peuvent être ajoutés dans une étape post-CMOS afin d'étudier la physique de ces dispositifs ou de réaliser une preuve de concept. Cette thèse étudie un qubit de spin à électron unique dans un dispositif CMOS avec un micro-aimant intégré dans le BEOL flexible. La relaxométrie révèle une séparation de vallée de l'ordre de 60 µeV et de longs temps de relaxation du spin autour de 400 ms. Des oscillations cohérentes utilisant la technique dite electric dipole spin resonance (EDSR) d'un spin d'électron unique avec des fréquences de Rabi autour de 1 MHz sont observées. La forme des oscillations de Rabi indique que la cohérence est limitée par le bruit à basse fréquence provenant des spins nucléaires restants dans le nanofil constitué de Si naturel.
Le couplage spin-orbite synthétique (SOC) est exploité pour contrôler le qubit via des champs électriques et étudier la physique de la vallée de spin en présence de SOC où une augmentation de la fréquence de Rabi est montrée au point de dégnérescence de la vallée et du spin.
Enfin, le bruit à haute fréquence dans le système est sondé en utilisant des séquences d'impulsions de découplage dynamique et il s'avère que le bruit de charge domine la décohérence du qubit dans cette gamme.
Les travaux présentés dans cette thèse apportent la première preuve expérimentale de

l'amélioration d'oscillations de Rabi avec la vallée et démontrent pour la première fois un qubit de spin électronique sur un substrat FD-SOI. La performance du qubit est comparable aux premières réalisations de qubits de spin sur d'autres plateformes de matériaux. L'introduction du ^{28}Si devrait améliorer considérablement les propriétés de cohérence et l'EDSR assistée par la vallée pourrait permettre des vitesses de rotation plus rapides pour améliorer la qualité du qubit.

Contents

1 Introduction **1**
1.1 Motivation . . . 1
1.2 Quantum computing . . . 2
1.2.1 Classical computing . . . 2
1.2.2 Basics principles of quantum computing . . . 2
Superposition and Measurement . . . 2
Bloch sphere . . . 3
Qubit manipulation . . . 4
Multiple qubits and entanglement . . . 5
1.3 Realizations of a quantum computer . . . 5
1.3.1 Nuclear magnetic resonance . . . 5
1.3.2 Trapped ions . . . 6
1.3.3 Superconducting qubits . . . 6
1.4 Spin qubits . . . 7
1.4.1 Spin as a qubit . . . 7
1.4.2 Spin qubit implementations . . . 7
Silicon-based spin qubits . . . 8
CMOS spin qubits . . . 9
1.5 Thesis structure . . . 12

2 Theoretical background **13**
2.1 Introduction . . . 13
2.2 Single quantum dots . . . 13
2.2.1 Electrostatic model . . . 13
2.2.2 Transport through a single quantum dot . . . 15
2.3 Double quantum dot . . . 18
2.3.1 Electrostatic model . . . 18
2.3.2 Transport through a double quantum dot . . . 19
2.4 Charge sensing . . . 22
2.4.1 Quantum point contact . . . 22
2.4.2 Single electron transistor . . . 22
2.5 Spins in quantum dots . . . 24
2.5.1 Single quantum dot . . . 25
2.5.2 Double quantum dot . . . 25
2.6 Spin measurements . . . 27
2.6.1 Energy selective spin readout . . . 28

2.6.2 Tunnel rate selective spin readout . . . 28
2.6.3 Pauli spin blockade . . . 29

3 Experimental techniques 31
3.1 Introduction . . . 31
3.2 Fabrication . . . 31
3.2.1 Principles of micro- and nanofabrication . . . 32
3.2.2 Industrial fabrication . . . 34
3.2.3 Academic fabrication . . . 36
Substrate and preprocessing . . . 37
Ohmic contacts and marks . . . 37
Isolation . . . 37
Palladium gates . . . 37
Post-fabrication annealing . . . 38
3.2.4 Post-CMOS processing . . . 38
Dicing and preparation . . . 39
Alignment . . . 39
Contact gates . . . 40
Isolation . . . 40
Micro-magnet . . . 40
Encapsulation and post-fabrication annealing . . . 41
3.3 Cryogenics . . . 42
3.3.1 Immersion refrigerator . . . 43
3.3.2 ^{3}He cryostat . . . 43
3.3.3 Dilution refrigerator . . . 43
3.4 Measurement setup . . . 44
3.4.1 Electronics . . . 44
Experiment structure . . . 44
DC voltages . . . 44
RF signals . . . 45
Data acquisition . . . 47
Magnetic field control . . . 47
3.4.2 Software . . . 47

4 Characterization 51
4.1 Introduction . . . 51
4.2 Device design . . . 51
4.2.1 Alignment marks, fanout and bond pads . . . 52
4.2.2 Hall bars . . . 52
4.2.3 Quantum dot devices . . . 53
4.3 Transistor measurements . . . 56
4.4 Hall bar measurements . . . 58
4.4.1 2 and 4 terminal resistance measurements . . . 58

4.4.2 Hall effect . . . 60
Classical Hall effect . . . 60
Quantum Hall effect . . . 61
Conductance plateaus . . . 61
Shubnikov de Haas oscillations . . . 63
Density and mobility . . . 63
4.4.3 Localization effects . . . 66
4.5 Quantum dot measurements . . . 68
4.6 Conclusion . . . 70

5 Electron spin qubit 73
5.1 Introduction . . . 73
5.2 Device design . . . 74
5.3 Quantum dot measurements . . . 77
5.3.1 Charge stability . . . 78
5.3.2 Gate lever arm and electron temperature . . . 78
5.4 Spin measurements . . . 80
5.4.1 Measurement procedure . . . 81
5.4.2 Spin relaxation . . . 84
Magnetic field dependence of the spin relaxation rate . . . 85
5.5 Spin manipulation . . . 88
5.5.1 Larmor precession . . . 88
Characterization of the micro-magnet stray field . . . 89
5.5.2 Rabi oscillations . . . 91
5.5.3 Power dependence of Rabi oscillations . . . 93
5.5.4 Valley enhanced EDSR . . . 94
Theory . . . 97
Alternative mechanisms . . . 99
5.6 Coherence . . . 102
5.7 Conclusion . . . 105

6 Conclusion and Outlook 107
6.1 Conclusion . . . 107
6.1.1 Characterization . . . 107
6.1.2 Electron spin qubit . . . 108
6.2 Outlook . . . 109

Bibliography 111

Appendix 127

Acknowledgments 127

CHAPTER 1

Introduction

1.1 Motivation

The improved understanding of quantum mechanics has lead to the first quantum revolution. Starting from the early twentieth century, major technological advances exploiting quantum effects were made. As a result, new technologies such as the laser, the global positioning system (GPS), magnetic resonance imaging (MRI), the light-emitting diode (LED) and the classical computer were developed.
Since the beginning of the twenty-first century a second quantum revolution has started [Dow03]. Here, not only existing quantum effects are exploited, but new quantum systems are engineered to enable completely new technologies. At the heart of the second quantum revolution is a new kind of computer called a quantum computer. Richard Feynman introduced the idea in 1982, when discussing the possibilities of simulating physics with computers [Fey82]. Since then quantum computing has developed into a vast field of research with an increasing number of commercial applications.
The interest in quantum computing is fueled by a predicted speedup for certain computational problems such as the Deutsch-Jozsa algorithm [Deu92], Shor's algorithm for prime number factorization [Sho97] and Grover's search algorithm [Gro96]. Coming back to Feynmans idea of simulating physics with computers, a quantum computer is also a powerful tool to simulate the physics of quantum systems [Llo96]. The approach becomes even more powerful as fault tolerant quantum computing can be achieved through quantum error correction [Fow12].
Currently, gate based quantum computing is in the noisy intermediate-scale quantum (NISQ) era, where 50 to a few hundred imperfect qubits are used to make proof of concept demonstrations and function as quantum accelerators together with classical supercomputers [Pre18]. Quantum annealers, a different approach to quantum computing, have already demonstrated their use when it comes to finding approximate solutions to optimization problems [Wil20].
For the future, the goal is to build universal quantum computers that outperform classical computers in solving useful problems. To accomplish this goal, millions of highly integrated qubits with high quality are necessary. In this context, leveraging complementary metal-oxide-semiconductor (CMOS) technology that made the integration of billions of transistors in classical computers possible seems natural. Hence, this thesis explores the potential of foundry fabricated CMOS spin qubits.

1.2 Quantum computing

In this section quantum computing is introduced as a concept. The intention is to provide a basic understanding of why a quantum computer could provide a computational advantage over a classical computer. First classical computing is introduced briefly as the baseline to compare to. Followed by an overview of the basic principles of quantum computing, where the concept of superposition, the Bloch sphere, qubit manipulation and entanglement are explained. This section can only provide a brief introduction. For a deeper discussion of the topic, the reader is referred to the following textbooks [Ihn09; Nie12].

1.2.1 Classical computing

A classical computer is based on boolean algebra where the basic unit of computation is the binary digit, short bit, where the state of a bit can be either 0 or 1. The information is encoded in the voltage applied to the logic circuit build from transistors.
The idea of a digital computing machine became first a reality with the Z3 of Konrad Zuse in 1941 [Ran75] and Alan Turing first formalized the concept of a universal computing machine [Tur37]. Early computers showed the potential, but they were typically based on large and unreliable vacuum tubes. Only replacing the vacuum tubes by transistors made computers scalable. The advances in semiconductor technology have lead to an astonishing increase in the density of transistors modeled empirically by Moore's law. It predicts that the density of transistors in an integrated circuit (IC) doubles about every two years [Moo06].
However, in recent years the increase in integration density has slowed down, showing a deviation from Moore's law [The17]. Further miniaturization of modern transistors starts to become limited by fundamental laws of physics. Currently quantum tunneling from the gate of a transistor and heat dissipation are limiting. The miniaturization will be ultimately limited by Heisenberg's uncertainty principle [Pow08]. Therefore, completely new approaches for computation, such as quantum computing and neuromorphic computing are coming to the center of attention.

1.2.2 Basics principles of quantum computing

Quantum computing extends the binary bit of a classical computer into a quantum bit (qubit). Instead of the voltage of a transistor, the quantum states $|0\rangle$ and $|1\rangle$ of a two level system are the new computational basis states.

Superposition and Measurement

The first distinction between a bit and a qubit is superposition. The two basis states are not either $|0\rangle$ or $|1\rangle$, but instead they can be a complex linear combination of both. In equation 1.1 the qubit state $|\Psi\rangle$ is expressed as a superposition of $|0\rangle$ or $|1\rangle$, with α and β being complex numbers fulfilling the condition $|\alpha|^2 + |\beta|^2 = 1$.

$$|\Psi\rangle = \alpha\,|0\rangle + \beta\,|1\rangle \tag{1.1}$$

However, in quantum mechanics a superposition can not be observed directly. The probability amplitudes α and β define the probabilities $\mathrm{p}_0 = |\alpha|^2$ and $\mathrm{p}_1 = |\beta|^2$ to observe the basis states $|0\rangle$ or $|1\rangle$ respectively. Only if the qubit state is purely in one of the basis

states meaning that $\alpha = 1$ and $\beta = 0$ or vice versa, the qubit state can be identified by a single measurement. If a state prepared in a superposition is measured, the wave function collapses and the state is projected on one of the basis states. One bit of information has been revealed by the measurement and the qubit remains in the state it was projected on. The quantum nature of the measurement poses a major challenge to the development of new algorithms for a quantum computer with a sizable speedup. It means that an efficient algorithm needs to end with the qubits being in one of the basis states [Aar08].

Bloch sphere

The superposition of the single qubit state can be rewritten as in Eq. 1.2 in spherical coordinates with the polar angle $\Theta \in [0,\pi]$ and the azimuthal angle $\Phi \in [0,2\pi)$. As a global phase has no meaning in quantum mechanics, the phase of α is chosen to be 0.

$$|\Psi\rangle = \cos\left(\frac{\Theta}{2}\right)|0\rangle + e^{i\Phi}\sin\left(\frac{\Theta}{2}\right)|1\rangle \tag{1.2}$$

This representation of the complex 2D quantum state can be visualized in 3D by a so-called Bloch sphere (Fig. 1.1).

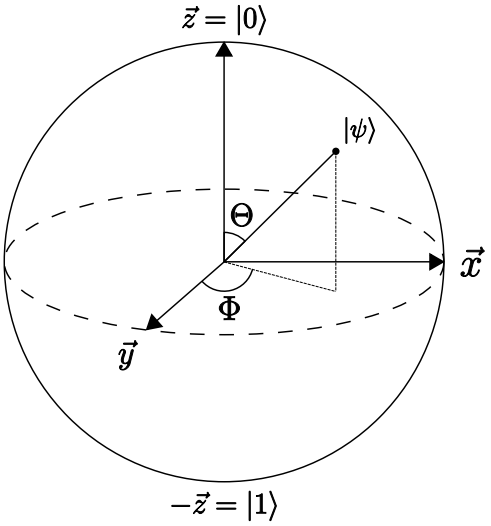

Figure 1.1: Bloch Sphere Representation of the qubit state $|\Psi\rangle$ as a vector in the Bloch sphere. The basis states $|0\rangle$ and $|1\rangle$ are on the north pole and south pole respectively. The cosine of the polar angle Θ represents the probability to measure the $|0\rangle$ or $|1\rangle$ state and the azimuthal angle Φ is the phase between the two basis states.

The qubit state is represented by a Bloch vector $\overrightarrow{r}$ of length 1. It can be expressed in Cartesian coordinates as the expectation values of the qubit state with respect to the Pauli matrices (Eq. 1.3), as shown in Eq. 1.4.

$$\sigma_x = \begin{pmatrix} 0 & 1 \\ 1 & 0 \end{pmatrix}, \qquad \sigma_y = \begin{pmatrix} 0 & -i \\ i & 0 \end{pmatrix}, \qquad \sigma_z = \begin{pmatrix} 1 & 0 \\ 0 & -1 \end{pmatrix} \tag{1.3}$$

$$\overrightarrow{r} = \begin{pmatrix} r_x \\ r_y \\ r_z \end{pmatrix} = \begin{pmatrix} \langle\Psi|\,\sigma_x\,|\Psi\rangle \\ \langle\Psi|\,\sigma_y\,|\Psi\rangle \\ \langle\Psi|\,\sigma_z\,|\Psi\rangle \end{pmatrix} \begin{pmatrix} 2\mathrm{Re}\alpha^*\beta \\ 2\mathrm{Im}\alpha^*\beta \\ |\alpha|^2 - |\beta|^2 \end{pmatrix} = \begin{pmatrix} \sin\Theta\cos\Phi \\ \sin\Theta\sin\Phi \\ \cos\Theta \end{pmatrix} \tag{1.4}$$

Qubit manipulation

Expressing the qubit state in terms of the Pauli matrices and using the Bloch sphere representation has the advantage that a manipulation of the qubit state can be seen as rotations in the Bloch sphere around the axis defined by the Pauli matrices.
Without a driving field applied, the Hamiltonian $\hat{H}_0$ is defined as in Eq. 1.5 with the resonant frequency ω_0.

$$\hat{H}_0 = \frac{\hbar}{2}\omega_0\sigma_z \tag{1.5}$$

When inserted in the Schrödinger equation 1.6, the time independent Hamiltonian leads to a stationary state where the probability to find one of the basis states remains constant. The qubit state only picks up a phase or in other words it precesses around the z-axis of the Bloch sphere.

$$\hat{H}_0\,|\Psi(t)\rangle = i\hbar\frac{\partial}{\partial t}\,|\Psi(t)\rangle \tag{1.6}$$

$$|\Psi(t)\rangle = e^{-\frac{i\hat{H}_0 t}{\hbar}}\,|\Psi(0)\rangle \tag{1.7}$$

$$= e^{-\frac{i\omega_0 t}{2}\sigma_z}\,|\Psi(0)\rangle \tag{1.8}$$

In the next step the qubit is driven by a field orthogonal to the qubit axis z with strength ω_1 and frequency ω. The corresponding interaction Hamiltonian $\hat{H}_{int}$ is shown in eq. 1.9.

$$\hat{H}_{int} = \frac{\hbar}{2}\omega_1\left(\cos(\omega t)\,\sigma_x + \sin(\omega t)\,\sigma_y\right) \tag{1.9}$$

The Schrödinger equation can be solved using the total Hamiltonian $\hat{H} = \hat{H}_0 + \hat{H}_{int}$. By transforming it in the rotating frame and applying the rotating wave approximation an analytical solution can be found. As a result, the probability to find the qubit in the excited state $|0\rangle$ oscillates with the total Rabi frequency $\Omega^2 = \omega_1^2 + (\omega - \omega_0)^2$, when being prepared initially in the ground state $|1\rangle$ (Eq. 1.10). The oscillation frequency depends on the strength of the driving ω_1 as well as the detuning $\omega - \omega_0$. The strength of the driving ω_1 corresponds to the Rabi frequency at 0 detuning.

$$P_{|0\rangle}(t) = \left(\frac{\omega_1}{\Omega}\right)\sin^2\left(\frac{\Omega t}{2}\right) \tag{1.10}$$

This formula is an important result, as it models the measurements of Larmor precession as well as Rabi oscillations in section 5.5. Applying the qubit drive for different pulse times and with different phases allows for controlled single qubit rotations on the Bloch sphere. These rotations allow to compose arbitrary single qubit gates.

Multiple qubits and entanglement

For a system with N qubits, a general multi qubit state $|\Psi\rangle$ is composed of 2^N orthogonal basis states $|J\rangle$ that can be all in superposition (Eq. 1.11).

$$|\Psi\rangle = \sum_{j_0 \dots j_N - 1 \in \{0,1\}^N} c_{j_0 \dots j_N - 1} \, |j_0 \dots j_N - 1\rangle = \sum_{J=0}^{2^N-1} c_J \, |J\rangle \tag{1.11}$$

These basis states span a 2^N-dimensional complex Hilbert space.
For two or more qubits another phenomenon called entanglement related to the quantum nature of the basis state can be exploited. Entanglement describes a quantum state that can not be factorized in a tensor product of its basis states. A typical example are the Bell states in Eq. 1.13:

$$|\Phi^{\pm}\rangle = \frac{1}{\sqrt{2}} \left(|00\rangle \pm |11\rangle\right) \tag{1.12}$$

$$|\Psi^{\pm}\rangle = \frac{1}{\sqrt{2}} \left(|01\rangle \pm |10\rangle\right) \tag{1.13}$$

As a consequence the qubits are correlated and a observation of one qubit determines the state of all the other qubits it is entangled with. Therefore, entangled qubits allow for an inherent parallelism which is the second reason why quantum computers are expected to provide a sizable speedup to certain computational problems.

1.3 Realizations of a quantum computer

Currently a multitude of approaches to build a universal gate based quantum computer are pursued. In this section, the most successful and promising physical realizations are presented to provide an overview of the state of the art in quantum computing. The working principle of each approach is briefly introduced, the advantages and disadvantages are discussed and the potential to scale-up is analyzed.

1.3.1 Nuclear magnetic resonance

In the late 1990s / early 2000s, a first quantum computer was implemented using nuclear magnetic resonance (NMR) [Van01]. The qubits are defined by spin-1/2 nuclei in a molecule that are distinguishable by NMR spectroscopy. Many of these molecules are then dissolved in a liquid to be manipulated and observed collectively resulting in a magnetic response that can be picked up by a coil at room temperature.
The NMR approach even deployed Shor's algorithm using 7 qubits to factor the number 15 into prime numbers [Van01]. However, this approach is limited in it's scalability. As the number of qubits in an NMR experiment is determined by the number of distinguishable nuclei with spin-1/2 in a molecule, scaling requires to create larger and larger molecules that eventually become unstable.

1.3.2 Trapped ions

Single ions can be trapped by time dependent electric fields inside a Paul trap. Typically, a linear array of trapped ions is used for quantum computing. Their internal electric structure is used to realize single and two qubit gates and the collective vibrational mode of the ion string is used as a bus-qubit. They can be manipulated using lasers and measured via fluorescence. A long exposure photograph of a Paul trap is shown in Fig. 1.2 a).
Trapped ions in a Paul trap can reach excellent single and two qubit fidelities beyond the threshold for error correction with error rates below 10^{-4} [Bal16]. High fidelities and long decoherence times with 10s of qubits implemented [Bru19; Fri18] make trapped ions one of the leading platforms in the current NISQ era. However, the excellent fidelities can only be reached in Paul traps which are not scalable. Scalable solutions are proposed and under investigation [Akh23; Lek17], but they still have to prove that they can provide the same fidelities as Paul traps and the overall size of a large scale ion trap quantum computer remains problematic.

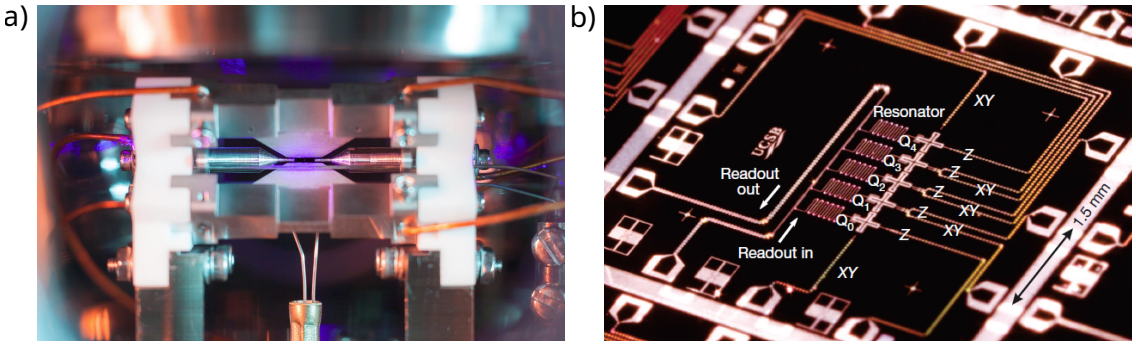

Figure 1.2: Qubit realizations a) A long exposure photograph an ion trapped in a Paul trap. The fine point in the center comes from the fluorescence of of the ion. Image credit: David Nadlinger. **b)** Picture of a device with 5 superconducting qubits. Source: [Bar14].

1.3.3 Superconducting qubits

Superconducting qubits can be implemented in different ways. A Transmon, the most common implementation, consist of superconducting islands connected by Josephson junctions. Manipulation of the qubit state is achieved by sending a microwave signal at the qubit frequency to the device and coupling the qubit to a resonator allows for readout. An example of a 5 qubit device is depicted in Fig. 1.2 b).
Superconducting qubits reach single qubit fidelities close to the ones realized in ion traps and similar two qubit fidelities [Bar14]. In contrast to the trapped ion approach, they can be arranged in a 2D-array. This has recently led to quantum error correction codes being successfully deployed bringing superconducting qubits closer to fault tolerant quantum computing [Ach23]. Quantum computers based on superconducting circuits have also claimed quantum supremacy for the first time [Aru19] by outperforming classical computers in a for a very specific task.
Superconducting qubits are currently the dominant approach with major industrial players like Google and IBM investing in the technology and many research groups dedicated to the

topic. As superconducting qubits are fabricated on chip using semiconductor fabrication techniques, they are expected to scale well for the near future. For ultimate scalability however, limiting factors are the large footprint of the superconducting circuits, their high sensitivity to noise, high frequency crosstalk and the requirement to operate at very low temperatures.

1.4 Spin qubits

Silicon-based electron spin qubits are the implementation of choice in this thesis. Hence the field of spin qubits is introduced in more detail explaining their relevance, the different implementations and their potential for building a scalable and universal quantum computer.

1.4.1 Spin as a qubit

The reason why a spin based quantum computer is so intriguing, is that a spin-$\frac{1}{2}$ in an external magnetic field is probably the most natural quantum 2 level system. Also, the spin is not susceptible to charge noise, but only to magnetic noise if no form of spin-orbit or spin-valley coupling is present.
The general model of a qubit from section 1.2 can be easily mapped to the magnetic moment of a spin-$\frac{1}{2}$ along the axis of the external magnetic field, as the two levels are split by the Zeeman effect. For a positive Landé factor g (e.g. in silicon) the ground state $|1\rangle$ corresponds to the spin pointing down $|\downarrow\rangle$ or against the direction of the external magnetic field. The exited state $|0\rangle$ corresponds to the spin pointing up $|\uparrow\rangle$ or in the direction of the external magnetic field. The magnetic moment $\overrightarrow{\mu}$ associated to an electron spin $\overrightarrow{S} = \frac{\hbar}{2}\overrightarrow{\sigma}$ is described by Eq. 1.14. $\overrightarrow{\sigma}$ is the vector of Pauli matrices, e the electron charge, m_e the electron mass and $\mu_B = \frac{\hbar e}{2m_e}$ the Bohr magneton.

$$\overrightarrow{\mu} = -\frac{ge}{2m_e}\overrightarrow{S} = -\frac{g\mu_B}{2}\overrightarrow{\sigma} \tag{1.14}$$

For a static external magnetic field applied along the z-axis $\overrightarrow{B} = B_0\overrightarrow{e_z}$ the resulting Hamiltonian is given by Eq. 1.15.

$$\hat{H}_0 = -\overrightarrow{\mu}\cdot\overrightarrow{B} = \frac{g\mu_B B_0}{2}\sigma_z \tag{1.15}$$

In analogy to Eq. 1.5 the frequency of Larmor precession $\omega_0 = \frac{g\mu B_0}{\hbar}$ is defined.
For a driving field B_1 orthogonal to the external magnetic field with frequency ω, the Hamiltonian can be extended by an interaction Hamiltonian as in Eq. 1.16.

$$\hat{H} = -\overrightarrow{\mu}\cdot\overrightarrow{B} = \frac{g\mu_B B_0}{2}\sigma_z + \frac{g\mu_B B_1}{2}\left(\cos(\omega t)\,\sigma_x + \sin(\omega t)\,\sigma_y\right) \tag{1.16}$$

In analogy to Eq. 1.9 the Rabi frequency at zero detuning is defined as $\omega_1 = \frac{g\mu B_1}{\hbar}$.

1.4.2 Spin qubit implementations

Already in 1998 Loss and DiVincenzo proposed a spin quantum computer based on single-electron quantum dots [Los98]. In the same year, a silicon-based nuclear spin quantum

computer was proposed by Kane [Kan98]. Since then, a variety of spin qubits has been proposed and realized.
Implementations based on nitrogen vacancy centers are omitted in this discussion, as they are not candidates for scalable quantum computing. However, they play a major role in quantum communication and quantum cryptography due to their coupling to visible light [Chi13].
Here, the focus is on spin qubits that are based on heterostructures in a broader sense, as they can potentially benefit from the same advanced semiconductor technology that allowed for the integration of billions of classical transistors [Van13].
Historically, electron spin qubits using gate defined quantum dots in a GaAs/(Al,Ga)As heterostructure [Kou97] have pioneered the development of many key building blocks for spin based qubits. Single shot spin readout has been first measured in 2004 [Elz04] and in 2005 the first singlet-triplet qubit was demonstrated [Pet05]. The first single spin qubit using electron spin resonance (ESR) has been demonstrated in 2006 [Kop06] and using electron dipole spin resonance (EDSR) in 2008 [Pio08]. This approach is still in use today for proof of concept demonstrations such as coherent spin control in 2D quantum dot arrays [Mor21a; Mor21b], distant spin entanglement [Jad21] and new readout schemes [Nur23]. However, the raw electron spin coherence in GaAs/(Al,Ga)As heterostructure based qubits is limited to 10s of nanoseconds by the Overhauser field generated by the nuclear spin bath [Blu10; Blu11].

Silicon-based spin qubits

Silicon-based spin qubits came to the center of attention, as they offer to isotopically purify the host material with isotopes that are nuclear spin free [Ito14]. Additional advantages are that they are compatible with CMOS foundry technology, as presented later. The negligible spin-orbit coupling of electrons in silicon can be interpreted as an advantage, because it protects the spin from decoherence due to charge noise.
However, the lack of spin-orbit coupling makes a stripline for spin manipulation via ESR or a micro-magnet for spin manipulation via EDSR necessary, which adds additional complexity to the fabrication process. The fabrication is further complexified by the large effective mass of electrons in silicon leading to smaller and therefore harder to control quantum dots. The presence of valleys in the conduction band leads to a spin-valley relaxation hot spot that can prevent spin readout and manipulation, but also leads to a cold spot for optimal qubit operation [Hos21]. Finally, silicon has an indirect band gap, which makes optical coupling and therefore the transfer of quantum information over long distances difficult.
Different approaches to build silicon-based spin qubits are pursued currently. First, there are spin qubits using the electron and nuclear spin of a phosphorus dopant implanted in a silicon substrate, following the proposal of Kane [Kan98]. These qubits shine with excellent coherence times [Muh14] as well as single and two qubit fidelities beyond the threshold for error correction [Mad22; Muh15]. They have also contributed significantly to the field of silicon spin qubits by demonstrating the first single shot spin readout in silicon [Mor10] and the single electron qubit in silicon using ESR [Pla12]. However, their scalability is limited because of the statistical nature of the implantation.

Quantum dot based electron spin qubits with a silicon quantum well can be formed either in a Si/SiGe or a Si-metal-oxide-semiconductor (Si-MOS) heterostructure. First single qubit implementations where reported in 2014 [Kaw14; Vel14] and one year later two qubit gates were demonstrated [Vel15]. Since then devices based on isotopically purified ^{28}Si have reached single and two qubit fidelities beyond the threshold for error correction [Mil22; Noi22; Xue22; Yon18]. Beyond these milestones, control over a quantum processor with up to six qubits has been reported [Phi22]. Qubit operation readout and operation has been shown at elevated temperatures of 1 K [Yan20]. Strong coupling of a single electron spin and a single microwave photon has been demonstrated [Mi17; Sam18] leading to the demonstration of long range two qubit gates [Bor20].
When replacing the n-doped leads in a Si-MOS heterostructure by p-doped ones, a 2D hole gas can be induced. Similarly holes can be induced in a Ge/SiGe heterostructure with a germanium well. The hole spin is another possibility to form a spin qubit. These qubits often suffer from short coherence times, however progress in this regard has been made recently [Pio22]. Also, hole spin qubits have demonstrated similar achievements as electron spin qubits, with single qubit operation [Hen20b], two qubit gates [Pet22] and the demonstration of a four qubit processor [Hen21]. This makes them a good candidate for spin based quantum computation, as well.

CMOS spin qubits

Silicon-based spin qubits all show a certain compatibility with advanced semiconductor fabrication technologies. However, making the leap from academic fabrication to qubits fabricated fully by industrial CMOS standards remains difficult. Academic fabrication typically relies on electron beam lithography (EBL) and metal lift-off techniques for gate pattering, offering a fast and flexible design/process flow, as well as great freedom in materials, processes and design. On the flip side, the academic approach is known for its high variability and therefore questionable scalability.
When transitioning to industrial CMOS fabrication, this freedom needs to be restricted in order to adhere to CMOS design rules, processes and materials. In combination with long turnaround times for changes in design or process, the challenges related to industrial qubit fabrication become apparent. At the same time, foundry based semiconductor fabrication is the only known technology able to build millions of nanometer scale devices [Van13]. It shines when it comes to the scalability, reproducibility and throughput of devices. Therefore foundry fabricated CMOS quantum dots are the ideal candidates to build a large scale universal quantum computer in the future.
In order to realize the potential, a consortium of the semiconductor research facility CEA-Leti and the research laboratories of CEA-Irig and the CNRS Institut Néel based in Grenoble has formed. Leading to pioneering work in the field demonstrating the formation of a single electron transistor (SET) in a CMOS device [Hof06] and the first CMOS hole spin qubit [Mau16]. Followed by the demonstration of electron spin resonance mediated by spin-valley-orbit coupling [Cor18], single-shot detection of electron spin states [Cir21; Nie22; Spe22; Urd19] and electron manipulation in small arrays [Ans20; Cha20; Gil20]. Recently, a collaboration between the semiconductor chip manufacturer Intel and TU Delft has successfully implemented single qubit operation using ESR an industrially processed

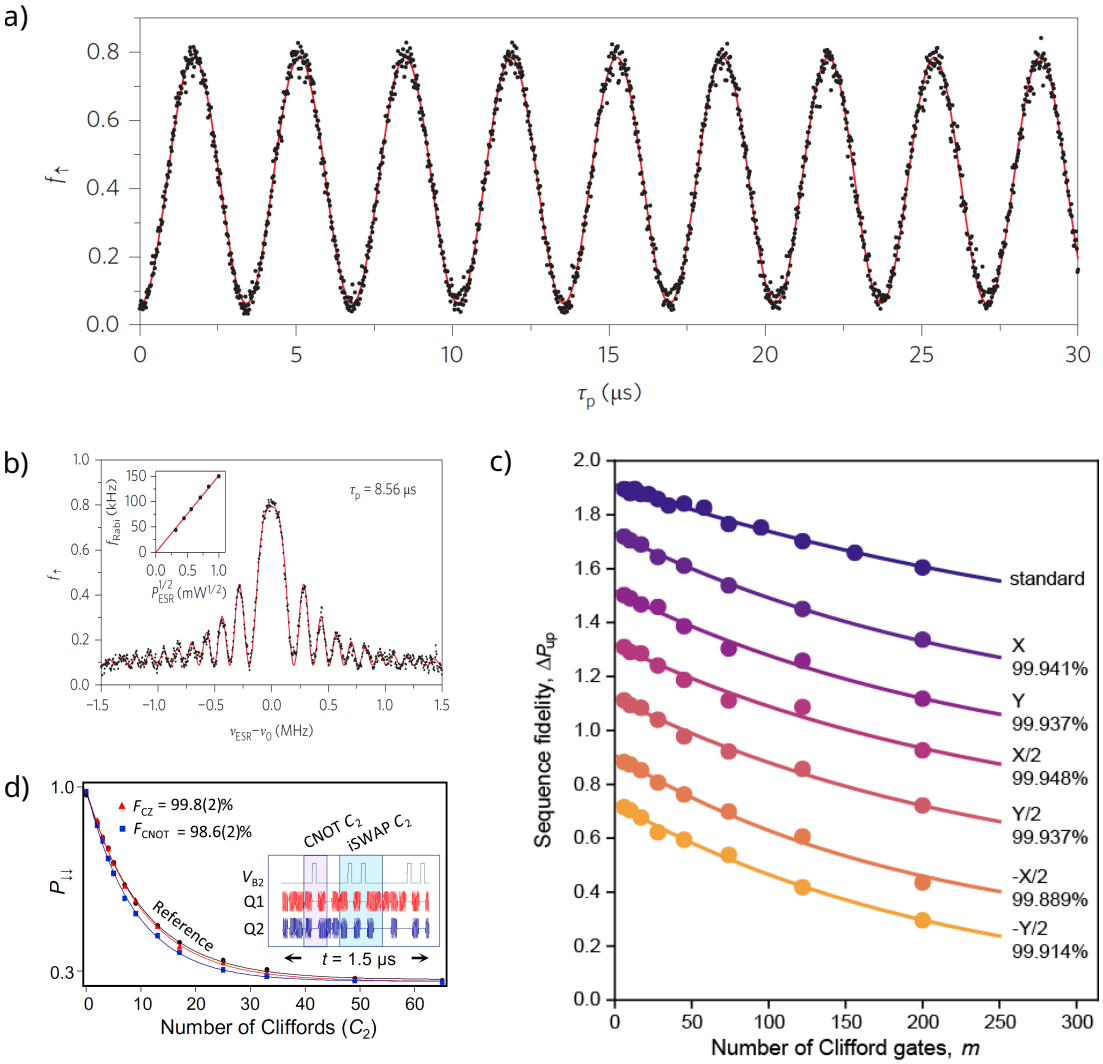

Figure 1.3: Silicon spin qubits: State of the art a) Rabi oscillations measured in a Si-MOS device using ESR. Source: [Vel14] **b)** Spin up fraction around the Larmor frequency using ESR. Source: [Vel14] **c)** Single qubit fidelities for different single qubit rotations. Source: [Yon18] **d)** Two qubit fidelities for the CZ gate and the CNOT gate. Source: [Mil22]

device [Zwe22].

However, making the direct leap from academic fabrication to qubits fabricated fully by industrial CMOS standards can still be difficult without intermediate solutions. An important step is to process all the parts of the qubits that are compatible with CMOS technology on an industrial level. Only adding the components that are not yet compatible with large scale integration by post-CMOS processing in an academic clean room. This approach allows exploring the physics of these spin qubits and characterize new modules before their integration. Among the different modules, the development of superconducting

resonators integrated in the post-CMOS process has proven to be successful in the coupling of photons with a hole spin qubit [Yu22] or for the readout of a quantum dot [Elh23]. Following the same principle, fabrication of magnetic materials for electric-dipole spin resonance (EDSR) could also be integrated in post-CMOS processing.

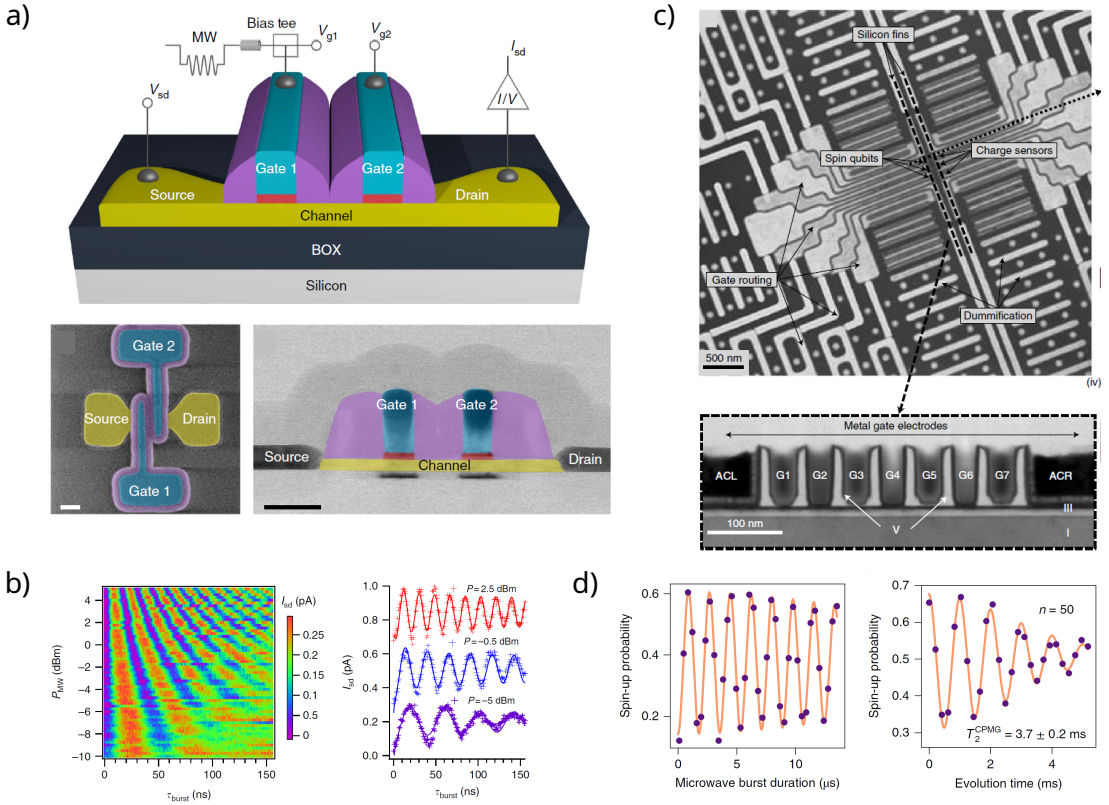

Figure 1.4: CMOS spin qubits a) Schematic, SEM and TEM image of the first CMOS hole spin qubit device from Grenoble. Source: [Mau16] **b)** Measurement of Rabi oscillations for different input powers on the device from a). Source: [Mau16] **c)** SEM and TEM image of the CMOS electron spin qubit device from Intel/TU Delft. Source: [Zwe22] **d)** Measurement of Rabi oscillations and CPMG experiment on the device from c). Source: [Zwe22]

1.5 Thesis structure

As discussed above, foundry fabricated CMOS quantum dots offer a great opportunity to build high quality spin qubit devices with the prospect of creating a scalable quantum computer [Gon21; Vel17]. However, the direct leap from academic fabrication to qubits fabricated fully by industrial CMOS standards is difficult without intermediate solutions. In this thesis, such intermediate solutions are explored for material characterization and the creation of proof of concepts. A single electron spin qubit in a CMOS device with a micro-magnet integrated in a flexible back-end-of-line (BEOL) is studied extensively. The synthetic spin orbit coupling (SOC) is exploited to control the qubit via electric fields and the spin-valley physics are investigated in the presence of SOC where an enhancement of the Rabi frequency at the spin-valley hot spot is shown [Kle23].

After this introduction, the charge and spin states of single and double quantum dots are modeled theoretically and different options for spin readout and charge sensing are discussed in **Chapter 2**.

In **Chapter 3** the device fabrication and the experimental setup is presented. After an introduction to the basic principles of micro- and nanofabrication, an overview of the industrial qubit device fabrication at CEA-Leti is given. The academic fabrication of Hall bars and quantum dot devices for material characterization is described in detail, followed by a successful demonstration of post-processing an industrially fabricated qubit device in an academic clean room. The industrial device is contacted and a FeCo micro-magnet for spin manipulation via EDSR is added to the device. Next, the different cryogenic setups for characterization and advanced measurements are shown and finally the measurement hardware and software necessary to perform quantum dot measurements as well as spin readout and manipulation are presented.

Chapter 4 covers the low temperature characterization of material properties relevant for qubits. The electron density and mobility is characterized via the quantum Hall effect on Hall bars fabricated on the same substrate the industrial fabrication uses. In the following, the charge stability is compared between devices made purely by academic fabrication and post-processed devices as well as the effect of post-fabrication annealing is investigated.

In **Chapter 5** a single electron spin qubit device with a micro-magnet added in post-processing is characterized. Spin readout is performed via energy selective spin readout and the spin relaxation is characterized. Spin manipulation is realized using EDSR, exploiting the synthetic SOC provided by the micro-magnet. In addition, an enhancement of the Rabi frequency is observed in close proximity to the spin relaxation hot spot.

CHAPTER 2

Theoretical background

2.1 Introduction

For electron spin qubits it is crucial to control the charge and the spin of single electrons. As gate defined quantum dots can be engineered with modern fabrication techniques and provide a high level of control, they are the method of choice to realize an electron spin qubit in this thesis.
In this chapter the general concept of quantum dots is explained. The idea is to provide a basic understanding of the physics and models behind the measurements presented in chapter 4 and 5. The discussion is based on the review articles [Han07; Wie02; Zwa13], which can also serve as an excellent source for further reading. As the electron spin in a quantum dot is a textbook example of a quantum two level system, spin manipulation is not discussed in this chapter. The reader is instead refereed to section 1.2 and 1.4 of the introduction, where the concept of qubit manipulation in general and how it can be applied to spins is explained. Advanced concepts specific to the discussion of certain measurements are introduced directly in chapter 4 and 5.
First, the charge in single quantum dot is described with an electrostatic model, then the transport of electrons through the quantum dot is described in Sec. 2.2. In the same way, the double quantum dot is introduced in Sec. 2.3. Next, techniques to sense the charge state of quantum dots via a quantum point contact (QPC) or a single electron transistor (SET) are described in Sec. 2.4. In the following section 2.5 the spin states in single quantum dots and double quantum dots are discussed with and without the presence of a magnetic field. Last, different possibilities to measure the spin are presented in Sec. 2.6, where energy and tunnel rate selective readout, as well as Pauli blockade readout are discussed.

2.2 Single quantum dots

In this section a single quantum dot is first described classically using a capacitor model and then orbital states are introduced in order to explain the behavior of a single quantum dot when probed in a transport experiment.

2.2.1 Electrostatic model

A quantum dot is generally speaking an artificial potential well that can trap electrons or holes. It can be seen as a small island for charges that is only capacitively coupled to its environment. A simple way to model a quantum dot is the capacitor model also known as the constant interaction model [Bee91; Ful87; Gor51]. In this model the quantum dot is coupled to its environment capacitively, assuming constant capacitances and negligible

electron-electron interaction. The model is visualized in Fig. 2.1. The environment is typically modeled by two electron reservoirs called source and drain as well as a gate. The connections between the reservoirs and the quantum dot is described by leaking capacitors, as electrons can tunnel through these connections. However, the tunneling resistance needs to remain larger than the inverse conductance quantum $R > \frac{h}{2e^2}$ in order to ensure a sufficient localization.
From this model, the electrostatic energy can be estimated starting from Eq. 2.1.

$$E = \frac{1}{2}CV^2 \tag{2.1}$$

The formula gives an expression for the electrostatic energy E of a capacitor depending on the total capacitance C and the voltage V. The total capacitance of the quantum dot is the sum of all capacitances $C = C_S + C_D + C_G$. The voltages and capacitances are defined as in Fig. 2.1 and e is the electron charge. The subscript S stands for source, D for drain and G for gate.
Charge quantization imposes that the charge on the quantum dot is an integer multiple of the elementary charge. Hence, the voltage can be calculated from the number of electrons in the quantum dot N as depicted in Eq. 2.2.

$$-Ne = C_S(V - V_S) + C_D(V - V_D) + C_G(V - V_G) \tag{2.2}$$

In combination with Eq. 2.1 the electrostatic energy can be expressed as in Eq. 2.3.

$$E = \frac{(-Ne + C_S V_S + C_D V_D + C_G V_G)^2}{2C} \tag{2.3}$$

When the size of the quantum dot is smaller than the Fermi wavelengths quantized energy levels can be observed in addition. In analogy to atoms they are orbital states. Due to their low electron density compared to metals, two dimensional electron gases (2DEGs) in semiconductor heterostructures have a large Fermi wavelength in the order of 10 nm to 100 nm, while the Fermi wavelength of metals is below 1 nm [Iba09]. This makes 2DEGs in semiconductor heterostructures ideal for engineering quantum dots as the required dimensions can be realized with modern lithography techniques. Therefore, the contribution of the orbitals has to be taken into account in addition to the classical electrostatic energy. According to the Pauli exclusion principle, each orbital can only contain a limited number of electrons depending on the spin and valley degeneracy. Once an orbital is occupied, the next orbital at higher energy is filled. Thereby, an additional energy cost for each orbital that is filled has to be taken into consideration.
As the energy cost of the orbitals depends on the material and the details of the confining potential, the orbital energy contribution is taken into account as the sum over the energy costs for each orbital.
More important than the total energy of the system is the energy to add an electron to the system. The energy to add the Nth electron is defined as the electrochemical potential μ. Eq. 2.4 shows the electrochemical potential as a function of the electron number. The formula is derived from Eq. 2.3 together with the orbital contribution to add the Nth

electron E_N.

$$\mu(N) = E(N) - E(N-1) = \left(N - \frac{1}{2}\right)\frac{e^2}{C} + E_N + \frac{C_G}{C}V_G = \left(N - \frac{1}{2}\right)E_C + \alpha V_G \quad (2.4)$$

$E_C = \frac{e^2}{C}$ is the charging energy and $\alpha = \frac{C_G}{C}$ is the α-factor or lever arm, the conversion factor between gate voltage and energy. Thanks to the small size of quantum dots, their capacitance remains small resulting in a large charging energy in the order of 0.1-10 meV. Hence, charging effects as well as the effect of orbital states can be observed in transport experiments at cryogenic temperatures.

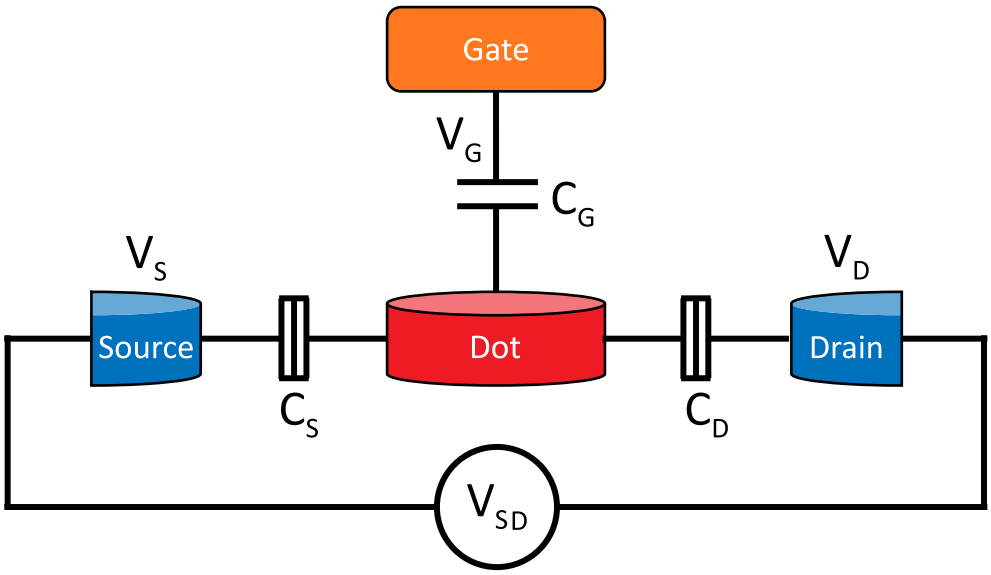

Figure 2.1: Electrostatic model of a single quantum dot. The quantum dot is modeled as a charged island coupled to the reservoirs named source and drain via a leaking capacitors C_S and C_D. The difference between the voltage applied to the drain V_D and source V_S defines the bias voltage V_{SD}. The gate is only capacitively coupled with capacity C_G and the gate voltage V_G controls the charge occupancy of the quantum dot.

2.2.2 Transport through a single quantum dot

The model from Fig. 2.1 is translated into an energy band diagram in Fig. 2.2 a) with the help of the previous considerations. The quantum dot is depicted as a potential well (gray) in the between source and drain reservoirs (blue), formed by tunnel barriers to the reservoirs. The source and drain reservoir have a slightly different electrochemical potentials opening a bias window of size V_{SD}. The depth of the quantum well can be varied by the gate voltage, thereby changing the position of the energy levels. The energy levels are visualized in green inside the potential well.
When an energy level aligns with the bias window it is possible to drive a current through the quantum dot. When the Nth energy level sits in between the electrochemical potential

of source and drain an electron can tunnel inside the quantum dot from the source. Due to the change in electrostatics associated with filling the Nth energy level, the level is shifted up in energy blocking additional electrons from tunneling from the source. However, the electron can tunnel out of the quantum dot to the drain and reseting the Nth energy level to its initial position. Only a single electron is flowing from source to drain at once, resulting in a measurable current.
If no energy level is situated inside the bias window, no current is flowing. All levels of the quantum dot below the drain electrochemical potential are occupied and there is no vacant state available to tunnel to. Energy levels in the quantum dot that are above the source electrochemical potential are empty, but no electron from the reservoirs can tunnel on this energy level. This situation is called Coulomb blockade.
The description above requires low temperatures and bias voltages V_{SD} small compared to the charging energy in order to be valid ($eV_{SD}, k_BT << E_C$). This ensures that electrons can not overcome the potential barriers or reach a higher energy level by thermal excitations. Coulomb blockade can be probed by varying the gate voltage and measuring the current flowing through the quantum dot. Fig 2.2 b) depicts the dependence of the conductance on the gate voltage. The current remains blocked, except for a small window, where an energy levels sits inside the bias window. The resulting peaks, shown in blue, are called Coulomb peaks.
For larger biases, conductance is possible for a larger window of gate voltages. Therefore, the Coulomb peaks become broader and eventually the bias becomes large enough to lift the Coulomb blockade. The interplay between source drain bias and the gate voltage is sketched in Fig. 2.2 c). The white areas depict the blocked regime with no current, while a current is flowing in the gray area. Due to the shape of the blocked regimes, they are called Coulomb diamonds. The size of the diamond in the bias direction is a measure of the charging energy plus the orbital contribution $eV_{SD} = \Delta E_N + E_C$. The extension of the diamond in gate voltage is also a measure of charging energy plus the orbital contribution but multiplied with the gate lever arm a_G $eV_G = \frac{1}{a_G}(\Delta E_N + E_C)$. Therefore, the gate lever arm can be extracted from both dimensions of the diamond, allowing to convert gate voltage into energy.

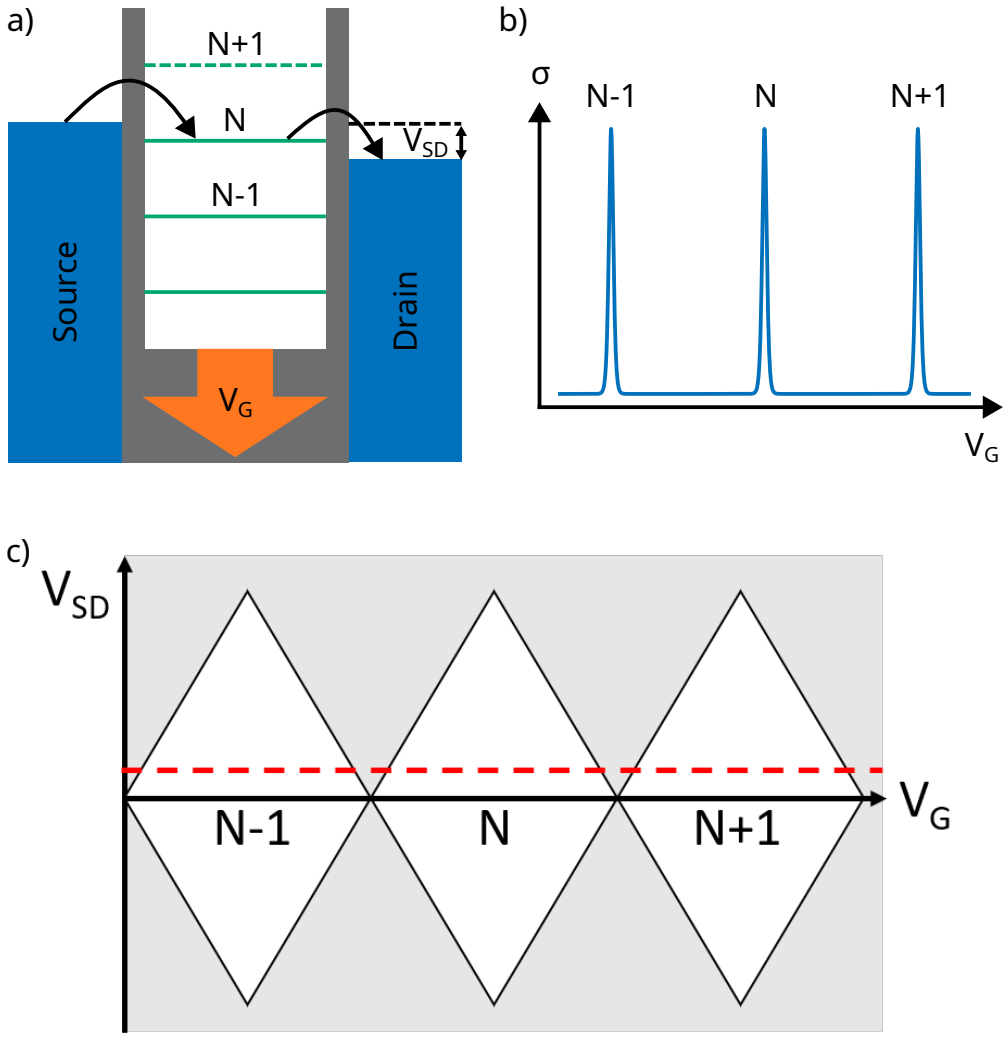

Figure 2.2: Transport through a single quantum dot. a) Energy levels in a quantum dot for a small source drain voltage V_{SD}. When the Nth energy level sits in between the electrochemical potential of source and drain an electron can tunnel inside the quantum dot from the source and it can tunnel out of the quantum dot to the drain. **b)** Conductance σ depending on the gate voltage V_G. The current remains blocked, except for a small window, where an energy levels sits inside the bias window. The resulting peaks, shown in blue, are called Coulomb peaks. **c)** Conductance (in grayscale) depending on the gate voltage V_G and the source drain voltage V_{SD}. In the gray area conductance is possible and the white area the current is blocked. Due to the shape of the blocked regimes, they are called Coulomb diamonds. The red dashed line corresponds to the cut shown in panel b).

2.3 Double quantum dot

A double quantum dot consists of two quantum dots coupled to each other. Depending on the coupling strength between the two quantum dots, behavior ranging from two separate quantum dots to a single large quantum dot can be observed. This transitions and the charge states of the double quantum dot in general can be mapped in a stability diagram. In this section, the stability diagram is discussed, as well as the electrostatic calculation of the charging energy and the electrochemical potential.

2.3.1 Electrostatic model

The electrostatic model of the single quantum dot can be extended to describe a double quantum dot. An additional quantum dot and gate needs to be included. The coupling between the two quantum dots is also modeled with a leaking capacitor C_m. The system is illustrated in Fig. 2.3. First, the electrostatic energy of the system is calculated in Eq.

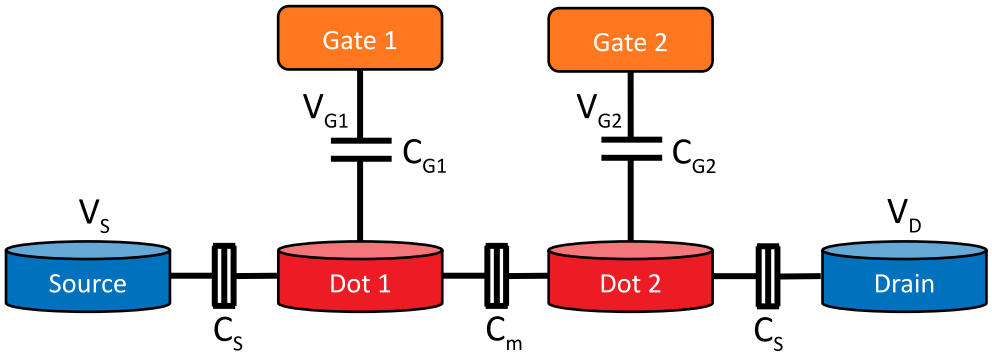

Figure 2.3: Electrostatic model of a double quantum dot. The capacitor model can be extended to a double quantum dot by introducing a coupling capacitance C_m coupling the two quantum dots. Each quantum dot is controlled by a separate gate with capacitance $C_{G1(2)}$ and voltage $V_{G1(2)}$.

2.5. The equation consists of the contribution of each quantum dot, a coupling term and an additional term that is independent of the electron numbers N_1 and N_2.

$$E(N_1,N_2) = \frac{1}{2}N_1^2 E_{C1} + \frac{1}{2}N_2^2 E_{C2} + N_1 N_2 E_{Cm} + f(V_{g1},V_{g2}) \tag{2.5}$$

E_{C1} (E_{C2}) is the charging energy of quantum dot one (quantum dot two). E_{Cm} is the coupling energy. It takes into account that if the electron number changes in one quantum dot, the energy of the other quantum dot changes. The formulas for these energies is given in Eq. 2.6. Here, the capacitances $C_1(C_2)$ of the quantum dots are defined as the sum of all capacitances directly connected to the quantum dot.

$$E_{C_1} = \frac{e^2}{C_1}\left(\frac{1}{1-\frac{C_m^2}{C_1 C_2}}\right) \quad E_{C_2} = \frac{e^2}{C_2}\left(\frac{1}{1-\frac{C_m^2}{C_1 C_2}}\right) \quad E_{C_m} = \frac{e^2}{C_m}\left(\frac{1}{1-\frac{C_1 C_2}{C_m^2}}\right) \tag{2.6}$$

Next, the electrochemical potential of each quantum dot can be calculated from the electrostatic energy of the system. Here, the last term of Eq. 2.5 cancels out. The formula for the electrochemical potentials is shown in Eq. 2.7 and 2.8. It includes the contribution of the quantum dot itself in the first part, a coupling term in the second part and a third part that is independent of the electron numbers.

$$\begin{aligned}\mu_1(N_1,N_2) &= E(N_1,N_2) - E(N_1-1,N_2) \\ &= \left(N_1 - \frac{1}{2}\right) E_{C1} + N_2 E_{Cm} - \frac{1}{|e|}(C_{g1}V_{g1}E_{C1} + C_{g2}V_{g2}E_{Cm})\end{aligned} \tag{2.7}$$

$$\begin{aligned}\mu_2(N_1,N_2) &= E(N_1,N_2) - E(N_1,N_2-1) \\ &= \left(N_2 - \frac{1}{2}\right) E_{C2} + N_1 E_{Cm} - \frac{1}{|e|}(C_{g2}V_{g2}E_{C2} + C_{g1}V_{g1}E_{Cm})\end{aligned} \tag{2.8}$$

2.3.2 Transport through a double quantum dot

From the electrochemical potential of the two quantum dots the stability diagram can be constructed. The stability diagram depicts the conductance through the double quantum dot plotted against the two gate voltages V_{g1} and V_{g2}. Each time, the electrochemical potentials of the two quantum dots is in between the electrochemical potentials of the source and drain, an electron can tunnel through the double quantum dot and conductance is possible. For negligible coupling between the two quantum dots, the voltage applied on a gate only influences the quantum dot below the gate and the coupling to the neighboring quantum dot is negligible. The result are lines perpendicular to the gate voltage axis that correspond to the Coulomb peaks discussed in the previous section. This situation is displayed in Fig. 2.4 a).
In the case of a strong coupling between the quantum dots, a large single quantum dot is formed. For a 45 ° cut through the stability diagram the Coulomb peaks of the large quantum dot can be recovered, as both gates control the electrochemical potential of the large quantum dot equally in this case. A sketch of the case of dominant coupling is shown in Fig. 2.4 c).
In an intermediate situation, a honeycomb pattern is formed. Fig. 2.4 b) shows this situation. Each quantum dot is mainly influenced by its own gate. However, the slope of the almost horizontal and almost vertical lines shows the coupling to the neighboring quantum dot. For theses lines an electron is exchanged with the reservoirs.
In addition, interdot transitions become visible. Here, electrons are exchanged between one quantum dot and the other, without exchanging an electron with the reservoirs. From Eq. 2.7 and 2.8 the size of the honeycomb pattern can be calculated. Quantized states $\Delta E = E_m - E_n$ are taken in to account in addition to the classical considerations discussed so far. Fig. 2.4 d) shows the situation and defines the relevant dimensions. Eq. 2.9 and 2.10 expresses how to calculate the dimensions of the honeycomb pattern within the model

discussed before.

$$\Delta V_{g1(2)} = \frac{|e|}{C_{g1(2)}} \left(1 + \frac{\Delta E}{E_{C1(2)}}\right) \tag{2.9}$$

$$\Delta V^{m}_{g1(2)} = \frac{|e| C_m}{C_{g1(2)} C_{1(2)}} \left(1 + \frac{\Delta E}{E_{Cm}}\right) \tag{2.10}$$

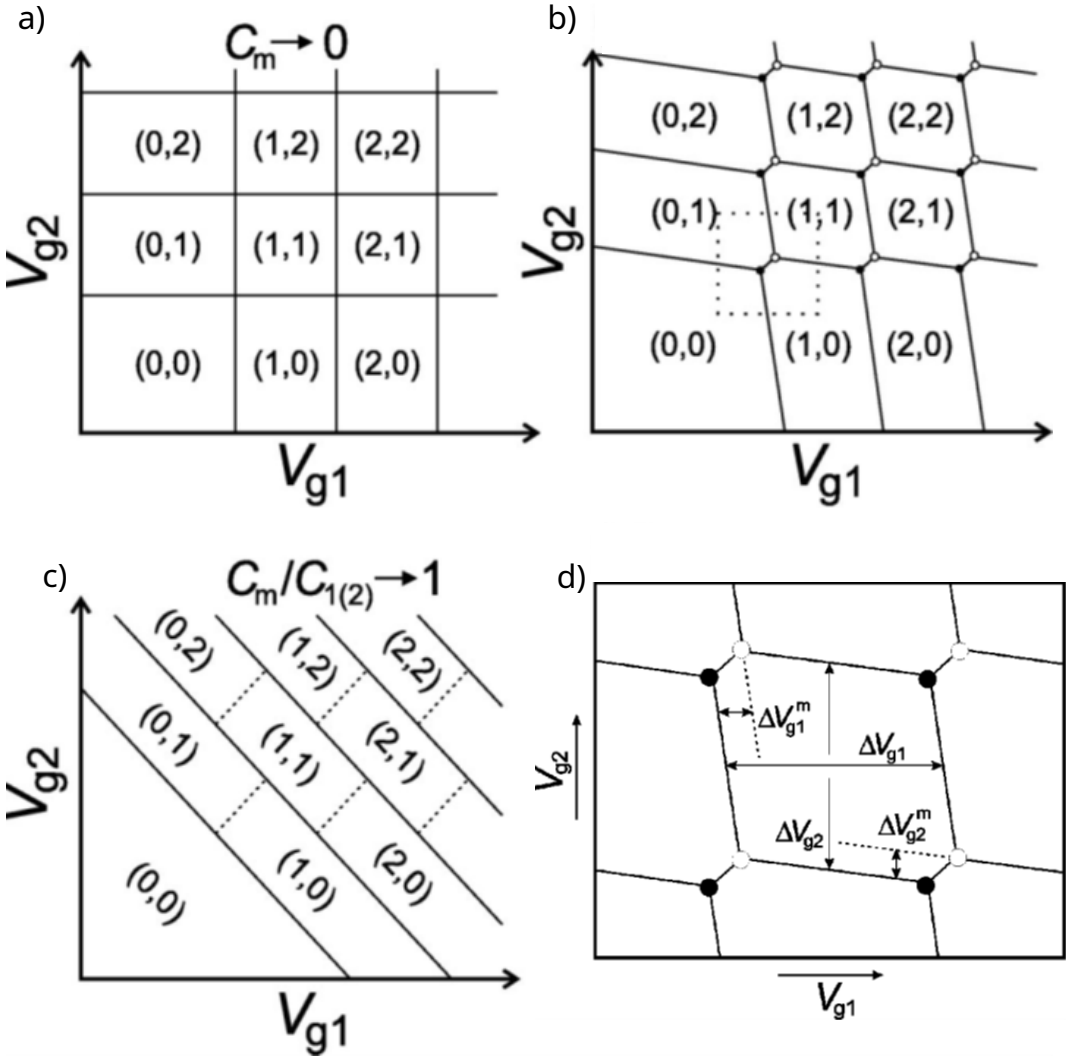

Figure 2.4: Stability diagram in different regimes. **a)** Stability diagram for zero coupling capacitance. The result are lines perpendicular to the gate voltage axis $V_{g1}(V_{g2})$ where current can flow that correspond to the Coulomb peaks of the respective quantum dot. **b)** In an intermediate situation, a honeycomb pattern is formed. Each quantum dot is mainly influenced by its own gate. However, the slope of the almost horizontal and almost vertical lines shows the coupling to the neighboring quantum dot. **c)** In the case of a strong coupling between the quantum dots, a large single quantum dot with equal influence from both gates is formed. **d)** Zoom into the honeycomb structure. The size of the honeycomb structure is determined by $\Delta V_{g1(2)}$ and the interdot coupling by $\Delta V_{g1(2)}^m$. Source: [Wie02]

2.4 Charge sensing

So far, the discussion was limited to effects visible, when a current is flowing through the quantum dot. The charge state of a quantum dot can also be probed remotely by an electrometer. Either a quantum point contact (QPC) or a single electron transistor (SET) is placed close to the quantum dot.
Remote charge sensing techniques make it possible to monitor the charge state of the quantum dot in regimes where transport through the quantum dot is not possible. For instance at low electron numbers, the tunnel barriers to the reservoirs and between quantum dots typically become opaque. In this situation, charge sensing is necessary to monitor the charge state down to the last electron.

2.4.1 Quantum point contact

A QPC is a small constriction for the current. At low temperatures and for a constriction comparable to the Fermi wavelength the conductance becomes quantized [Wee88]. When recording the current as a function of the constricting voltage, conductance plateaus are observed, as sketched in Fig. 2.5 a). In between plateaus the conductance rises sharply and is very sensitive to voltage variations, i.e. its electrostatic environment. The reason for this sensitivity is that the charge of the electrons in a nearby quantum dot couples capacitively to the QPC by changing the constriction. The red dot in Fig. 2.5 a) indicates the measurement position for charge sensing.
Monitoring the conductance while sweeping the gate voltage of the quantum dot probed results in a general slope due to capacitive coupling of the gate and the QPC. In addition, jumps occur every time an electron enters or leaves the quantum dot, as shown in Fig. 2.5 c). When the derivative of the conductance with respect to the gate voltage is plotted, the capacitive effect of the gate is removed and the changes in charge configuration of the quantum dot are highlighted. This result is sketched in Fig. 2.5 d). The jumps are converted into peaks that correspond to the Coulomb peaks of the probed quantum dot.

2.4.2 Single electron transistor

A SET is a single quantum dot that is probed in transport as presented previously in section 2.2. For remote charge sensing it is placed close to the probed quantum dot. The aim is to increase the capacitive coupling, while avoiding tunnel coupling. For charge sensing the SET is tuned on the edge of a Coulomb peak indicated by the red dot in Fig. 2.5 b). Similar to the QPC, the conductance of the SET becomes very sensitive to electrostatic changes nearby. In the case of the SET, the alignment of an energy level with the source or drain reservoir is influenced by the electrostatic changes induced by the probed quantum dot. Again, the derivative of the conductance with respect to the gate voltage reveals changes in the charge configuration of the quantum dot.
The advantage of a SET is the increased sensitivity compared to a QPC, as the Coulomb peaks are steeper. Hence, the charge sensitivity and the signal-to-noise ratio (SNR) at the measurement point is increased. A 30 times increase sensitivity and a three times increase in SNR is reported in the literature [Bar10]. However, a SET is typically more complicated to fabricate and harder to tune. In addition, the dynamic range of gate voltage in which the SET stays sensitive to its environment is smaller. The trade-off between sensitivity

and dynamic range can be tuned by broadening the Coulomb peak with an increased bias. The sensitivity and bandwidth of both the QPC and the SET can be improved when integrated into a resonant circuit. A RF-QPC or RF-SET probes the amplitude or phase of the reflected signal the charge state. It measures the charge state without the frequency limitations from the RC cutoff caused by the resistance and capacitance of the device and setup. The need for an external electrometer can be avoided by gate or source reflectometry of the probed dot. However, these advanced techniques require additional tuning and a dedicated setup. In this thesis a DC-SET is will be used to measure the charge and spin configuration of nearby quantum dot that serves as a spin qubit. The next sections explain how spin measurements can be performed by monitoring the charge state.

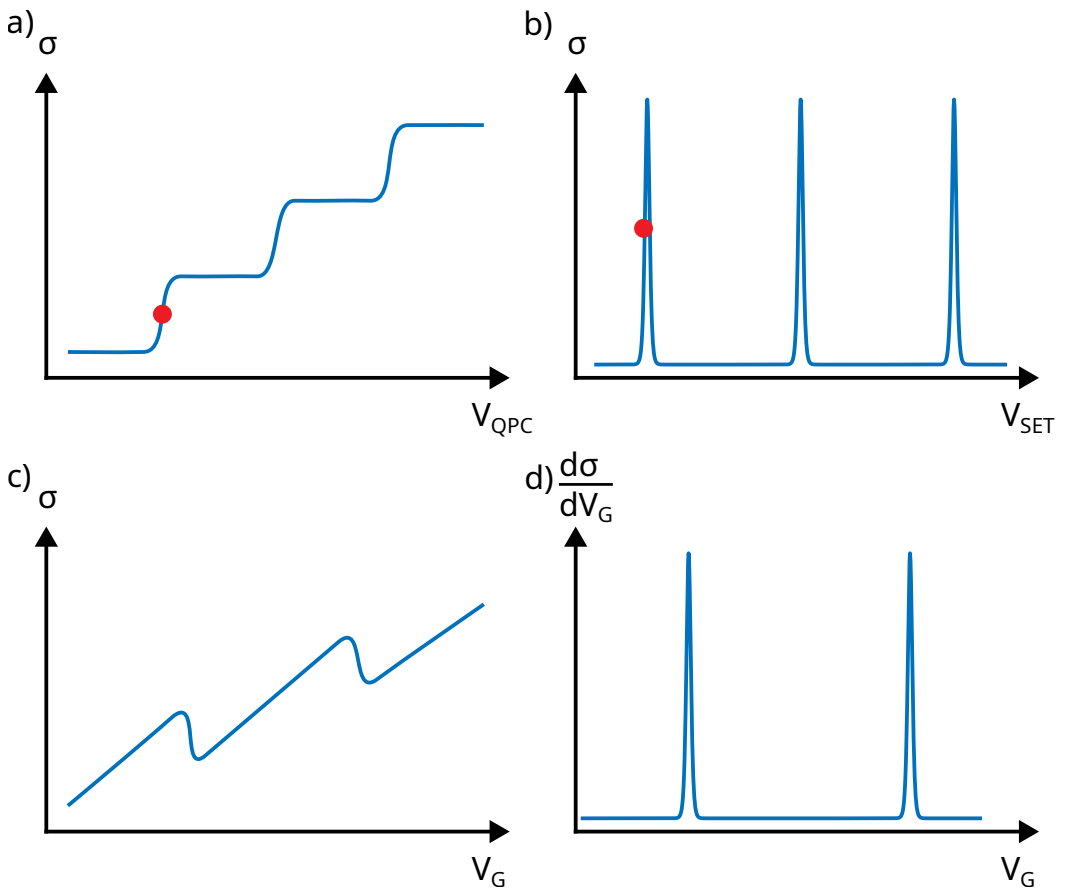

Figure 2.5: Charge sensing via a QPC and a SET a) Quantized conductance σ through the QPC with respect to the QPC gate voltage V_{QPC}. The red dot indicates the measurement position for charge sensing. **b)** Coulomb peaks of a SET with respect to the SET gate voltage V_{SET}. The red dot indicates the measurement position for charge sensing. **c)** Conductance σ of the QPC/SET at the measurement position depending on the gate voltage V_g of the quantum dot probed. A general slope due to capacitive coupling of the QPC/SET to the gate of the quantum dot is visible. Two distinct jumps are visible where an electron enters or leaves the quantum dot. **d)** Derivative of the conductance $\frac{d\sigma}{dV_g}$ of the QPC/SET with respect to the gate voltage V_g of the quantum dot probed. The capacitive effect of the gate is removed and the changes in charge configuration of the probed quantum dot are highlighted.

2.5 Spins in quantum dots

After a discussion of the charge states in quantum dots, the spin states are now introduced. The possible spin states for a single and a double quantum dot containing one or two electrons are introduced. The reason why the spin is of particular interest for qubit applications is that the electron spin is a natural two level quantum system that is well protected from charge noise, as it only directly couples to a magnetic field.

2.5.1 Single quantum dot

The simplest case to describe spins in quantum dots, is a single spin in a single quantum dot. The spin can either face up $|\uparrow\rangle$ or down $|\downarrow\rangle$. Without the presence of a magnetic field, these two eigenstates are degenerate. In the presence of a magnetic field the states are split in energy by the Zeeman splitting. The splitting can be calculated from Eq. 2.11.

$$\Delta E_Z = g\mu_B B \tag{2.11}$$

The energy difference between the $|\uparrow\rangle$ state and the $|\downarrow\rangle$ state is denoted with ΔE_Z. The Landé factor g is a material dependent constant that determines the slope of the spitting and which state is lower/higher in energy. mu_B is the Bohr magneton and B is the magnetic field.
Next, two spins in a single quantum dot are discussed. For two spins the Pauli exclusion principle has to be taken into account. The wave function of two fermions has to be antisymmetric with respect to the exchange of the two particles. Therefore, either the orbital or the spin part of the wave function has to be antisymmetric. When both electrons occupy the charge ground state $|g\rangle$, the spins have to have opposite direction. This state is called singlet S and is shown in Eq. 2.12. It is characterized by a total spin s of 0 and a spin quantum number m_s of 0.

$$|S\rangle = |gg\rangle \otimes \frac{|\uparrow\downarrow\rangle - |\downarrow\uparrow\rangle}{\sqrt{2}} \tag{2.12}$$

For a triplet state, the orbital part of the wave function is antisymmetric and the spin part is symmetric. In order to obtain an antisymmetric orbital part, the exited charge state $|e\rangle$ has to be occupied. The triplet states are characterized by a total spin s of 1. When both spins are pointing up, the state is called T_+ as the spin quantum number m_s is equal to +1 (see Eq. 2.13). For both spins pointing down the state is called T_- with a spin quantum number m_s is equal to -1 (see Eq. 2.14). For a symmetric superposition of up and down the state is called T_0, as the spin quantum number m_s is equal to 0 (see Eq. 2.15).

$$|T_+\rangle = \frac{|ge\rangle - |eg\rangle}{\sqrt{2}} \otimes |\uparrow\uparrow\rangle \tag{2.13}$$

$$|T_-\rangle = \frac{|ge\rangle - |eg\rangle}{\sqrt{2}} \otimes |\downarrow\downarrow\rangle \tag{2.14}$$

$$|T_0\rangle = \frac{|ge\rangle - |eg\rangle}{\sqrt{2}} \otimes \frac{|\uparrow\downarrow\rangle + |\uparrow\downarrow\rangle}{\sqrt{2}} \tag{2.15}$$

Without a magnetic field, the triplet states are degenerate in energy. In the presence of an magnetic field, this degeneracy is lifted by the Zeeman splitting.

2.5.2 Double quantum dot

In Sec. 2.3 the different regimes of coupling in a double quantum dot are discussed. For an uncoupled double quantum dot with $t_c = 0$ two electrons can either be in the left dot

(2,0) or in the right dot (0,2) or one electron in each dot (1,1). Which configuration is preferred, is determined by the difference in potential energy between the to dots that is called detuning ε.
The spin states are defined in analogy to two electrons in a single quantum dot and the charge configuration is noted in addition. A singlet state can either be $|S(2,0)\rangle$, $|S(0,2)\rangle$ or $|S(1,1)\rangle$. The triplet state without the presence of an magnetic field can be $|T(2,0)\rangle$, $|T(0,2)\rangle$ or $|T(1,1)\rangle$. In contrast to the single dot, $|T(1,1)\rangle$ does not need to occupy an exited orbital state.
The situation for $t_c = 0$ is displayed in Fig. 2.6 a). Singlet and Triplet in the (1,1) charge state are the energetically favorable state around zero detuning and they remain constant in energy. In the (1,1) charge configuration the charging energy needs to be overcome in each quantum dot and the total energy cost is the charging energy independent of the detuning. For the S(2,0) or S(0,2) state the charging energy needs to be overcome twice. These states start at higher energies, but they become more and more favorable in energy with stronger detuning and cross the S(1,1) and T(1,1) state. The detuning deepens the potential well of one quantum dot while the potential of the other quantum dot becomes more shallow. Eventually the cost to fill the deep quantum dot with two electrons becomes lower than the the cost to fill both quantum dots equally. For even stronger detuning, the T(2,0) and T(0,2) states cross the (1,1) states as well. The same mechanism as described before lowers the energy of the T(2,0) and T(0,2) states, but they start at higher energies due to the additional energy cost for forming a triplet state.
For a tunnel coupling larger than 0, the crossings discussed before become avoided crossings. A gap between the S(1,1) (T(1,1)) and the S(2,0)/S(0,2) (T(2,0)/T(0,2)) opens. Theoretical calculations show that the gap between S(1,1) and S(0,2) is twice the tunnel coupling. Also, a small energy gap of $\frac{4t_c^2}{E_C}$ opens between the S(1,1) and the T(1,1) state. The situation for a finite tunnel coupling is shown in Fig. 2.6 b).
In the presence of a magnetic field, the triplet states split up into T_+, T_- and T_0. As the splitting depends on the Landé factor and therefore on the material.

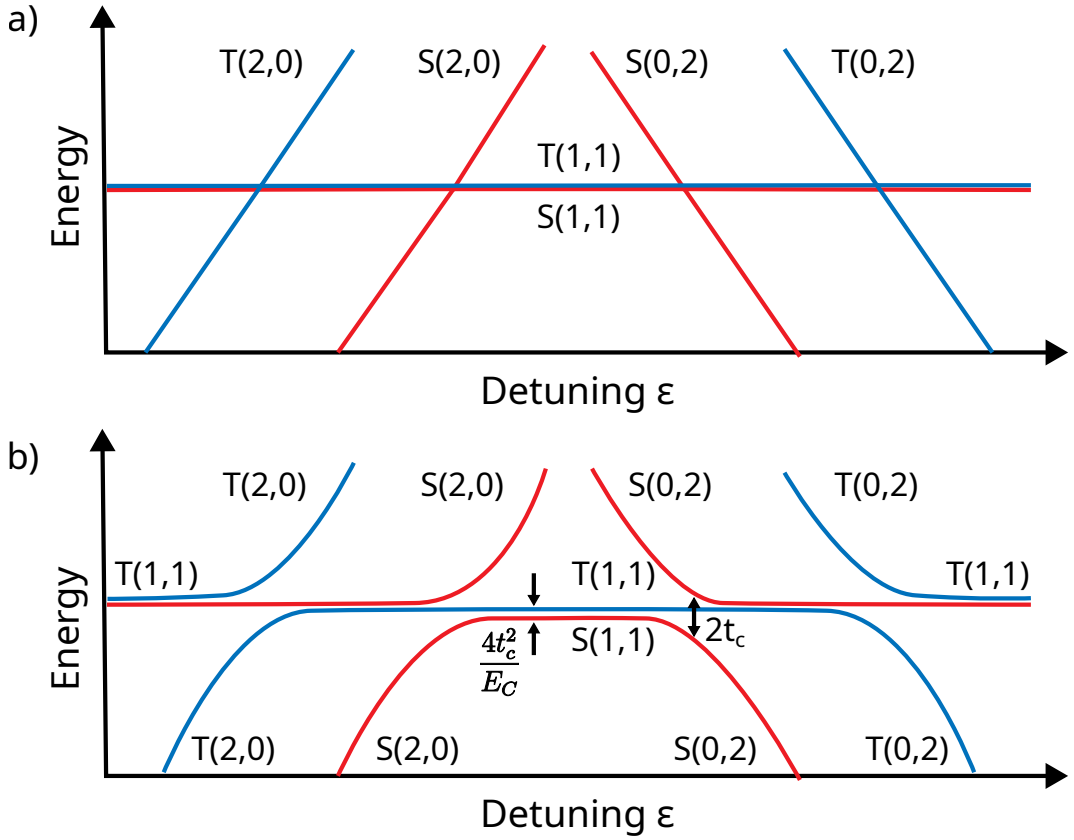

Figure 2.6: Energy band diagram of two spins in a double quantum dot a) For an uncoupled double quantum dot with $t_c = 0$ two electrons can either be in the left dot (2,0) or in the right dot (0,2) or one electron in each dot (1,1). Which configuration is preferred, is determined by the difference in potential energy between the to dots that is called detuning ε. **b)** For a tunnel coupling larger than 0, the crossings become avoided crossings. A gap of $2t_c$ opens between the S(1,1) (T(1,1)) states and the S(2,0)/S(0,2) (T(2,0)/T(0,2)). A second smaller gap of $\frac{4t_c^2}{E_C}$ opens between the S(1,1) and T(1,1) state.

2.6 Spin measurements

Measuring the magnetic moment of a single electron spin directly is difficult. Therefore, a common method to readout the spin state of a quantum dot is spin-to-charge conversion. The spin state is mapped via a spin dependent tunneling process to a charge state that can be read out with one of the techniques discussed in Sec. 2.4. In this section different implementations of spin measurements using spin-to-charge conversion via a spin dependent tunneling are discussed. First energy selective spin readout and tunnel rate selective spin readout are presented to read out the spin state of a single quantum dot, followed by Pauli spin blockade to read out the spin state of a double quantum dot.

2.6.1 Energy selective spin readout

For a single quantum dot the spin state can be read out via spin dependent tunneling with a reservoir. The first is energy selective spin readout is discussed. When the Fermi level of the reservoir lies between the ground and exited spin state, an electron occupying the ground spin state can not tunnel to the reservoir. On the other hand, an electron occupying the exited spin state can tunnel to the reservoir and another electron from the reservoir is able to tunnel into the quantum dot occupying the ground state. If the exited spin has tunneled out of the quantum dot, but the new electron has not yet tunneled to the ground state, the quantum dot contains one electron less. This change in the electron number can be detected with a charge sensor, indicating that the exited spin state was occupied. This method is depicted in Fig. 2.7 for a single spin in a single quantum dot. Here, the spin up state represents the exited state and the spin down state the ground state.
Several challenges have to be overcome in order to realize energy selective spin readout. First, a large magnetic field is typically required. The resulting Zeeman splitting of the two spin states needs to be much lager than spread of the Fermi level. The Fermi level of the reservoirs thermally broadened with the Fermi-Dirac distribution. Hence, the the temperature needs to be much smaller then the Zeeman energy ($k_BT << E_z$).
Second, the Fermi level needs to be placed in between the two energy levels with high precision. Charge noise present in the proximity of the quantum dot can cause the spin states to shift and thereby make energy selective spin readout impossible. In addition, the tunnel rate needs to be tuned in order to make sure that the exited spin can tunnel out before relaxing to the ground state. At the same time, an electron from the reservoir needs to tunnel slow enough to the quantum dot that the temporary change in electron number can be detected.

2.6.2 Tunnel rate selective spin readout

The challenge of positioning the Fermi level in between the two spin states is a major limitation for the energy selective spin readout. In order to circumvent this challenge, both energy levels can be placed above the Fermi level and a difference in the tunnel rate can be exploited.
One state tunnels earlier out of the dot than the other. The tunnel event can be recorded with an external charge sensor as discussed before. Therefore, a threshold in time can be defined to distinguish between the spin states.
For two electrons in a single quantum dot, the triplet tunnels out first, as its wave function is more distributed to the sides of the quantum dots.
The limitations of this approach are similar to the energy selective readout, except for the positioning of the Fermi level. A new challenge arises that the system needs to be tuned in a configuration where the tunnel rate difference is sufficient to be detected.
In addition to the discussed limitations, energy and tunnel selective spin readout have the disadvantage that an electron is lost to the reservoir during the process. Therefore, the quantum state of the electron is destroyed.

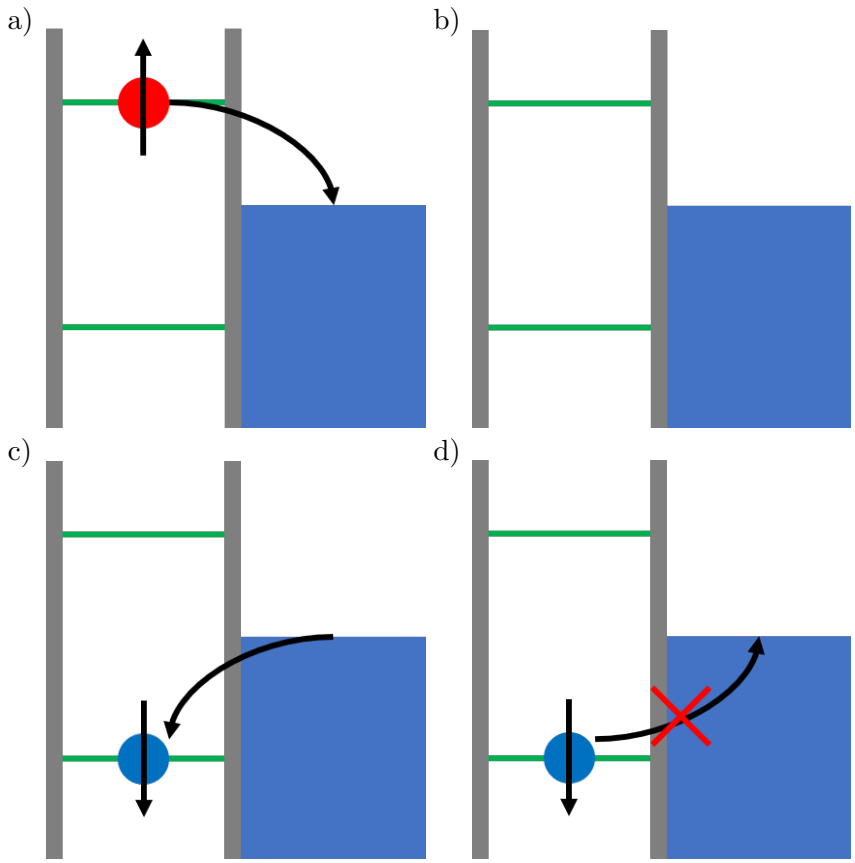

Figure 2.7: Energy selective spin readout. a) Exited spin state is initially occupied. **b)** The spin up electron can tunnel to the reservoir, leaving the quantum dot empty for a short time. **c)** Another electron with spin down orientation can can tunnel from the reservoir into the quantum dot. **d)** If the ground spin state was occupied initially, the electron can not tunnel to the reservoir.

2.6.3 Pauli spin blockade

In a single quantum dot spin readout via spin-to-charge conversion is possible, but suffers several limitations as discussed before. Spin readout double quantum dot of a can be realized using Pauli spin blockade (PSB).
The double quantum dot is initially in the (1,1) charge configuration and either in the S(1,1) or in the T(1,1) spin configuration. Then the double quantum dot potential is detuned until the S(2,0) configuration is energetically favorable, while the T(2,0) configuration is still blocked. This situation is described in Fig 2.8. The readout requires that the spin orientation of the first electron (depicted in blue) is fixed in the ground state. The spin state of the second electron (depicted in green or red) can then be mapped to the (2,0) charge state for the singlet configuration and to the (1,1) charge state for the triplet configuration. This configuration remains until the triplet relaxes to the singlet configuration. The difference in charge configuration can be detected via an external charge sensor that is

most sensitive to one of the quantum dots.
A disadvantage of this approach is that an additional quantum dot with an electron in the ground state is required. Also, distinguishing between the (1,1) and the (2,0) configuration can be challenging, as the total electron number in the double quantum dot remains constant.

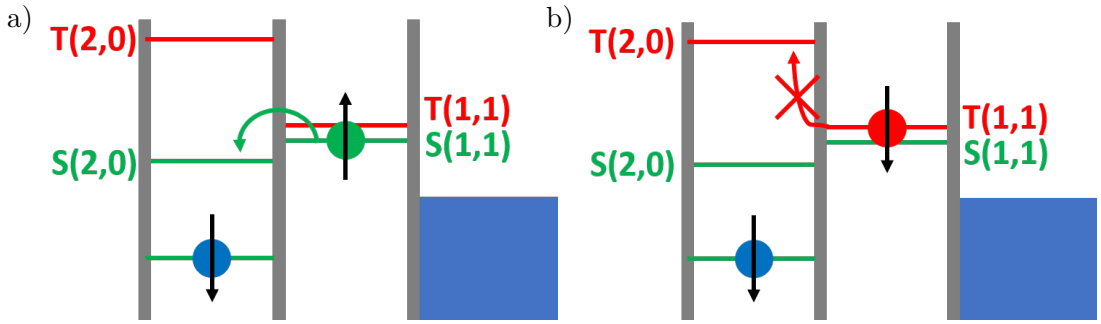

Figure 2.8: Schematic of PSB. a) The S(1,1) singlet can tunnel to the S(2,0) configuration. **b)** The T(1,1) triplet remains blocked in the (1,1) configuration.

CHAPTER 3

Experimental techniques

3.1 Introduction

Making industrial spin qubit devices and post-processing them in an academic clean room, requires many advanced semiconductor fabrication techniques. Measuring spin qubits typically requires very low temperatures only achievable in dilution cryostats and a complicated electronic setup is necessary to readout and control the spin.
In this chapter the industrial and academic fabrication of the devices measured in this thesis is explained in Sec. 3.2, the cryostats used for characterization and advanced measurements are presented in Sec. 3.3 and the measurement setup for spin readout and manipulation is described in Sec. 3.4.

3.2 Fabrication

Exploring the charge and spin properties of single electrons in a Si quantum dot requires devices on the scale of tens of nanometers to be fabricated. A tight confinement separates the charge states of the quantum dot so that single quantum levels can be addressed at low temperatures. While confinement in the z-direction is achieved by the growth of the heterostructure, the in plane confinement needs to be engineered by patterning the nanowire and by using metallic gates. Therefore, advanced techniques of micro- and nanofabrication are necessary to accomplish this goal. In addition, the purity of these devices needs to be on a very high level to probe only the intended quantum states. Hence, the material quality, as well as a clean room environment are crucial for processing.
These conditions are matched by industrial semiconductor processing. Where the industrial fabrication shines when it comes to the scalability, reproducibility and throughput of devices. However, industrial fabrication has a long turnaround time, design rules need to be respected and it is limited to CMOS processes only. Academic fabrication on the other hand has a fast and flexible design/process flow plus it offers a great freedom in materials, processes and design. At the same time, the academic approach is known for its high variability and its scalability is questionable.
A key element of this thesis is to combine the advantages of both approaches to a hybrid fabrication process. As a result, the industrial platform can be characterized in new ways and proof of principle devices can be created. The material quality of the industrial process regarding its properties at low temperatures can be assessed using Hall bars and simple quantum dot structures. The potential of industrially fabricated quantum dot devices as qubits can be tested by post-processing them after the frontend. Here, superconducting, magnetic or custom structures can be added where an easy integration into the industrial

fabrication process would not be possible.
In this section the general principles of micro- and nanofabrication are introduced first. Then, the fabrication of the industrial device is presented. Next, the production of Hall bars and simple quantum dot devices for material characterization is shown. Finally, the fabrication of a qubit device using post-processing is discussed.

3.2.1 Principles of micro- and nanofabrication

In this subsection the basic principles of micro- and nanofabrication are presented. The aim is to engineer gate structures down to the scale of tens of nanometers in order to achieve electrical control of single electrons. This goal can be accomplished with tools, processes and materials available in an academic clean room, which are presented in the following.

Cleaning The devices are cleaned before every lithography step and every time the device has been taken out of the clean room (e.g. SEM analysis, ALD deposition). The standard procedure consists of two consecutive baths in acetone followed by a bath in isopropyl alcohol for 5 min with 1 min of ultra sound cleaning for each step. Finally, the device is dried with compressed nitrogen.

Cleaving and dicing In a hybrid academic/industrial fabrication process the starting point for the academic part is a 300 mm wafer used in industrial semiconductor manufacturing. First the wafer is cleaved into pieces small enough for sawing using special pliers. Next, these pieces are spin coated with a thick resist for protection. The protected pieces are sawed into dies small enough for processing in an academic clean room using a DISCO dicing saw. Finally, the resit is removed. After the entire fabrication process another sawing step is necessary. The devices are subdiced into smaller pieces to fit into the PCB for measurement.

Lithography The general purpose of a lithography is to transfer a pattern into a resist.
In a first step, the substrate is cleaned and then a dehydration bake is performed to remove any water or solvents that might be still on the surface. The process is depicted in Fig. 3.1 a). Subsequently, the prepared surface is cooled down back to room temperature and the resist is spin coated on the device. A soft bake is performed afterwards in order to remove the solvents from the resist as shown in Fig. 3.1 b). The sample is now prepared for the exposure either with UV light or with an electron beam as presented in Fig. 3.1 c). The type of resist, the bake temperatures and bake times depend on the type of exposure.
Traditionally, the pattern is transfered using a mask aligner that shines UV light on a mask exposing only part of the resist to the UV light. In this thesis however, all devices are fabricated maskless. This means that the pattern is written either by a laser oder by an electron beam into the resist. The advantage of a maskless lithography is that the design can be changed without creating a new mask.
For the optical lithography the DWL66FS laser lithography system from Heidelberg Instruments is used. A laser with a wavelength of 405-410 nm exposes only the parts of resist that correspond to the pattern. The laser lithography is used to define pattern down

to a few microns.
For smaller patterns the NanoBeam NB5 electron beam lithography (EBL) system is used. The EBL transfers a pattern into a resist using an electron beam instead of laser light. Thereby, the resolution of the lithography is no longer limited by the wavelength of light. In principle the De Broglie wavelength of the electrons is now limiting. However, practically the beam focusing, scattering of electrons and the lift-off process are limiting the resolution to a few tens of nanometers.
The last step of the lithography is the development. It is depicted in Fig. 3.1 d). The exposure makes the resist soluble for the developer, while the unexposed resist can not be dissolved by the developer. The developer is specific for the resist that was used. A 1:1 mixture of Mircodeposit developer and Di-Water is used for the laser lithography, while a 1:3 mixture of of methyl isobutyl ketone (MIBK) and isopropyl alcohol (IPA) is used for the EBL. The result of the lithographic process is shown in Fig. 3.1 e).

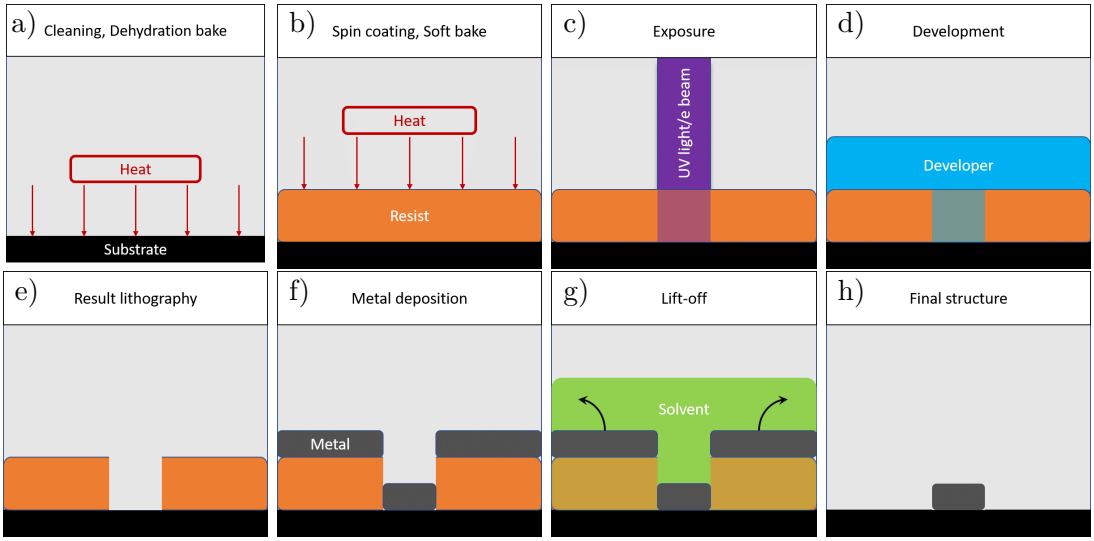

Figure 3.1: Lithography and Lift-off process a) The cleaned substrate is heated to remove all remaining water and solvents. **b)** A layer of resit is spin coated onto the substrate and is heated to remove all solvents from the resist. The resist is hardened in this step. **c)** The resist is exposed by UV light or an electron beam. **d)** During the development the exposed resit dissolves. **e)** The pattern is transfered into the resist. **f)** A layer of metal is deposited on top of the resist. **g)** A solvent dissolves the resit causing the redundant metal to lift-off. **h)** Final gate structure.

Evaporation and lift-off Starting with a sample after Lithography, the patten in the resist needs to be transferred into a metallic gate structure. Therefore, metal is deposited on the entire chip with the Plassys MEB550S e-beam evaporator as depicted in Fig. 3.1 f). Subsequently, the resit is dissolved with a solvent and the redundant metal is lifted with it. N-Methyl-2-pyrrolidon (NMP) or acetone with an ultrasonic bath is used to support the lift-off. This step is presented in Fig. 3.1 g). The final result is a metallic gate structure as shown in Fig. 3.1 h). Optionally, the surface can be prepared with ion milling before

metal deposition. Here, the surface is hit with Ar^+ ions to remove contaminations or small layers of oxide.

Atomic Layer deposition In order to overlap multiple gate structures, they have to be isolated from each other. The isolation is achieved via an atomic layer deposition (ALD) of Al_2O_3. The machine used is a Cambridge Nanotech Savannah S100 for thermal deposition. The Al_2O_3 is grown atomic layer by atomic layer using alternating pulses of trimethylaluminum (TMA) as a precursor and water.
For improved device quality plasma enhanced ALD using the machine Fiji 200 from Ultratech is applied. Here, the water pulse is replaced by an O_2 plasma for an increased reactivity with the precursor. For optimal quality the process chamber is always heated to 250 °C and the entire device is coated with a film of Al_2O_3.

Wet etching For the devices made with academic fabrication methods, the SiO_2 is wet etched prior to the deposition of the ohmic contacts in order to make a direct contact between the metal and the implanted silicon. Buffered hydrofluoric acid (BHF) with a concentration of 7:1 is used for this task. The BHF also provides selective etching between SiO_2 and Si, as well as a hydrogen passivation of the Si surface.

Annealing For the silicidation process of the ohmic contacts, as well as for the post fabrication annealing a rapid thermal annealer (RTP) is used. The Jipelec JetFirst RTP Furnace heats the device following precise temperature ramps using halogen lamps for heating. The device can be either kept under vacuum or a process gas with a controlled flow can be let into the device chamber.
First, the device chamber is pumped to evacuate the remaining air, subsequently forming gas (95 % Ar, 5 % H_2) is injected with the maximum flow rate to create a forming gas atmosphere. Then the device is heated to 350 °C in a 10 s long ramp. The temperature of 350 °C is held for either 30 min or 5 min depending on the process. Finally, the forming gas is evacuated again from the chamber and the device cools down before the chamber is purged with Ar gas.

3.2.2 Industrial fabrication

In this part, the fabrication of qubit devices at CEA-Leti is described. They are CMOS-fabricated silicon nanowire devices based on FD-SOI technology from CEA Leti on 300 mm wafers. These devices have been successfully used for the creation of quantum dot arrays[Ans20; Cha20; Gil20], electron spin readout [Nie22; Spe22; Urd19] and for demonstrating a hole spin qubit [Mau16]. Also post-processing has been successfully adopted to demonstrate strong coupling between a photon and a hole spin [Yu22] or for the readout of a quantum dot [Elh23]. The fabrication of the frontend and the first step of contact formation as part of the backend is presented. The remaining steps of the backend are omitted, as the wafer is transferred to the academic clean room before for post-processing.
The starting point is a commercial 300 mm FD-SOI wafer from Soitec shown in Fig. 3.2 a). It is composed of a first layer of 775 µm of undoped Si, a buried oxide layer (BOX) of 145 nm and a top layer of undoped silicon. The top layer is thinned down to 12.8 nm in

order to obtain the desired Si and SiO_2 thickness after oxidation.
In the next step, the active is patterned forming a dog bone shaped nanowire of width 90 nm trimmed to 80 nm. It is illustrated in gray in Fig. 3.2 b). This task is accomplished using deep UV (DUV) lithography and etching. In the following, the remaining active is thermally oxidized to obtain a channel thickness of 10 nm of Si and a SiO_2 gate oxide of 6 nm shown in Fig. 3.2 c). After thermal oxidation the gate stack of 5 nm TiN and 50 nm polysilicon is deposited as pictured in Fig. 3.2 d). The TiN layer tunes the work function and therefore the threshold voltage and the polysilicon serves as the gate metal. Subsequently, the gate is patterned using DUV lithography and is trimmed using EBL. In Fig. 3.2 e) the olive green pattern corresponds to the DUV lithography and the light purple areas the ones that are trimmed using EBL. The EBL step finalizes the size of the gates and defines the cut between split gates as well as neighboring gates in the case of multi gate devices. The device discussed in this thesis has a single pair of split gates with a gate length L_G of 50 nm and a gate separation S_V of 50 nm.
Next SiN is deposited isotropically over the device. With an anisotropic etch the SiN film is removed from the sample except for a small area of 31.5 nm length around the gate. The remaining SiN structures are called spacers and are depicted in dark purple in Fig. 3.2 f). The spacers protect the small area around the gate from in situ doping in the next step. Thereby, a potential barrier between the quantum dot and the reservoir is formed. The reservoirs are formed by in situ doping (ISD). The unprotected areas of the channel are removed and replaced by Si in situ doped with phosphorous as depicted in Fig. 3.2 g). Fig. 3.2 h) shows a top view of the device after the frontend.
Before the device is post-processed in an academic clean room, the first step of the backend is performed to create contacts to the gates and reservoirs. The device is buried under 200 nm of SiO_2 with tungsten vias to contact the gates and reservoirs. A hole with high aspect ratio is etched into the SiO_2 and tungsten is deposited isotropically to fill the holes and establish contact in Fig. 3.2 i). The top layer of tungsten (light green) that has formed is removed by chemical mechanical polishing (CMP). Like this only the contacts (dark green) remain on a flat surface ready for contacting. In the complete process the contacts would be connected to a metal layer leading to bond pads. The process of contact formation and metal layer creation would repeated for as many metal layers as necessary to contact a given device.
A post-fabrication annealing is performed as final step of the CMOS process. For the complete process this step would take place after all metal layers are defined. For post-processing it is performed as well to heal potential damages due to the exposure to EBL.

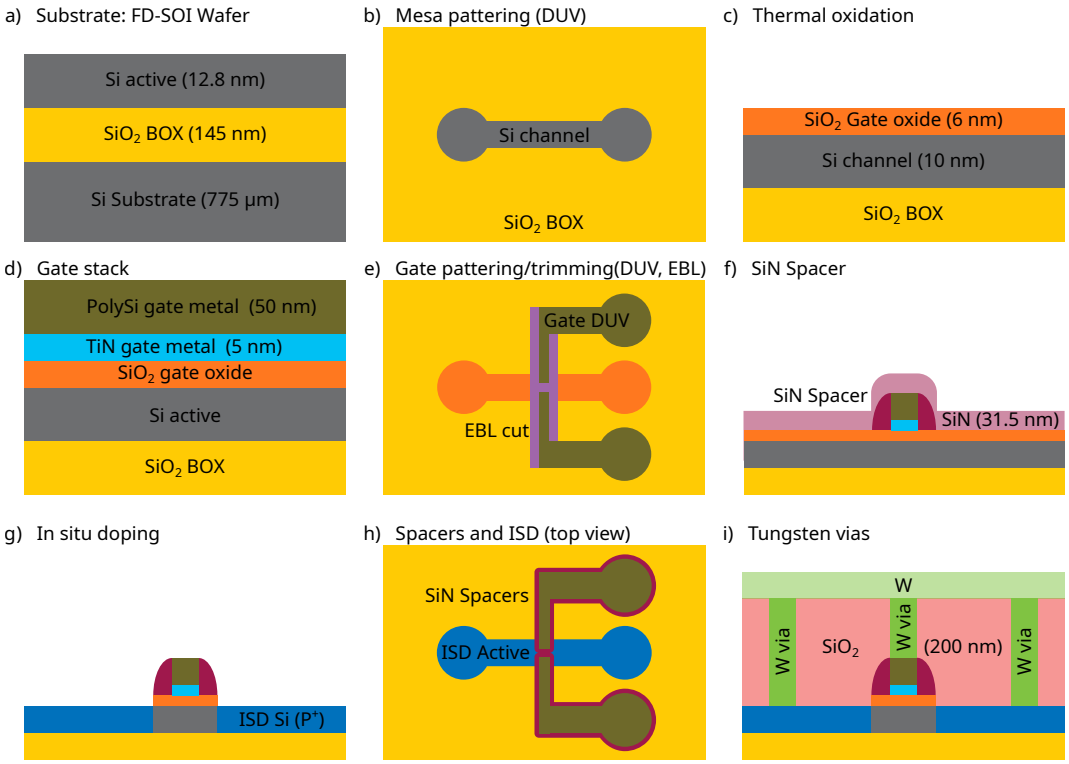

Figure 3.2: Industrial process a) The starting point is a FD-SOI wafer with the top Si layer thinned down. **b)** Active Mesa pattering using DUV to form the nanowire. **c)** Thermal oxidation to create the Si active and the gate oxide. **d)** Deposition of the gate stack. 5 nm TiN are deposited first to tune the work function, then 50 nm of polysilicon are deposited. **e)** Pattering and trimming of the gates using DUV (olive green) and EBL (light purple). **f)** Deposition and etching of the SiN spacers. A 31.5 nm thick layer of SiN grown isotropically, followed by an anisotropic etch leaving only the SiN spacers (dark purple) around the gates. **g)** In situ doping of the reservoirs. The active area that is not protected by the spacers is etched and replaced in situ by silicon doped with phosphorous. **h)** Resulting structure after the frontend is completed. **i)** Formation of tungsten vias. First, 200 nm SiO_2 are deposited, followed by etching holes through the oxide where a contact is established. The holes are filled with tungsten and the excess tungsten is removed using CMP (light green).

3.2.3 Academic fabrication

The industrial fabrication process can be interrupted earlier to assess the material quality. Test structures such as Hall bars which are not present on the mask set for the CMOS process are fabricated in an academic clean room. Hall bars give access to the electron density and mobility of the 2DEG. Simple quantum dot devices are processed to compare the performance of the industrial substrate with academic devices build with similar techniques.

In this section the formation of ohmic contacts and alignment marks is discussed. The contacts are isolated from palladium gates fabricated in the next layer. Finally, the post-fabrication annealing is discussed.

Substrate and preprocessing

The industrial fabrication process is stopped in this case after mesa patterning and thermal oxidation. The mesa of the relevant devices is not a dogbone shaped nanowire, but instead a 15 µm by 15 µm square. The mesa coresponds to the dark gray square in Fig. 3.3 a). It allows for devices with a planar gate structure similar to other academic approaches. In addition, areas of high dopant concentration are formed via ion implantation of phosphorous dopants before thermal oxidation. The crystal structure is healed from implantation damage and the dopants are incorporated in the crystal at the same time as the thermal oxidation takes place.
In order to fit in all machines of the academic clean room, the wafer is cleaved and diced to a size of 10 mm by 12.5 mm. As a last step before processing, the samples are cleaned thoroughly.

Ohmic contacts and marks

In a fist step, ohmic contacts and alignment marks are defined. The design of the ohmic contacts and markers will be presented in 4.2. For this layer EBL is used to transfer the pattern into the resist. A 200 nm thick PMMA with a polymer chain length of 50 k is used. In order to form ohmic contacts, the gate oxide is etched with buffered hydrofluoric acid (BHF) and a metal stack of 10 nm titanium and 50 nm platinum is evaporated. For some devices an additional layer of nickel was used. The layer stack for these devices is 25 nm nickel 5 nm titanium and 30 nm platinum. The final layer of platinum, thanks to it's density of 21.45 $\frac{g}{cm^3}$, makes the markers created in this layer well visible for the EBL. The metal deposition has to take place as soon as possible, as the BHF passivates the surface only for a short time.
After metal deposition, the titanium or the nickel needs to diffuse into the doped area to form an ohmic contact. Therefore, the sample is annealed at 350 ° C for 30 min in the case of titanium as a contact metal and for 1 min in the case of nickel as contact metal. The annealing takes place in a forming gas atmosphere (95 % argon 5 % hydrogen) with the maximum available flow of 2000 sccm. The forming gas is already annealing the device as it will be discussed in a following paragraph about post-fabrication annealing. The ohmic contact gates are false colored in olive green and the implanted areas are depicted by the dashed squares in Fig. 3.3.

Isolation

The isolation to the substrate, between the gates and an encapsulation layer consists of Al_2O_3 grown by thermal ALD. The chamber temperature is 250 °C and an Al_2O_3 layer of either 10 nm or 3 nm is grown. The Al_2O_3 is deposited over the entire chip without any resist applied in order to use a high chamber temperature for a high quality deposition.

Palladium gates

The depletion gates as well as the accumulation gates are made out of palladium and they are separated by an Al_2O_3 isolation layer. Their design, for the different devices, will be presented in Sec. 4.2. For this layer EBL is used to transfer the pattern into the resist. A 70 nm thick PMMA with a polymer chain length of 50 k is spin coated on the device. Each

layer of palladium has a thickness of 30 nm and is deposited via electron beam evaporation. It is shown in purple in Fig. 3.3.
Palladium gates, in contrast to the established aluminum gates, offer a smaller grain size and palladium does not form a native oxide. The smaller grain size enables smaller gate features. The absence of a native oxide especially below the gate reduces strain and thereby the formation of unintentional quantum dots. Palladium gates have been first used in the context of Si/SiO_2 spin qubits by [Bra18]. Different groups have already adopted palladium gates successfully in their recent experiments [Law20; Zha19].

Post-fabrication annealing

As a last step, the device undergoes a post-fabrication annealing. It has the purpose of passivating dangling bonds on the Si/SiO_2 interface with hydrogen provided by the forming gas and by hydrogen present in the ALD. The device is annealed at 350 ° C for 5 min in a forming gas atmosphere (95 % argon 5 % hydrogen) with the maximum available flow of 2000 sccm. A post-fabrication annealing was first suggested in the context of Si/SiO_2 spin qubits by [Spr16] and has is been established since as a standard step in the fabrication of silicon-based qubits.

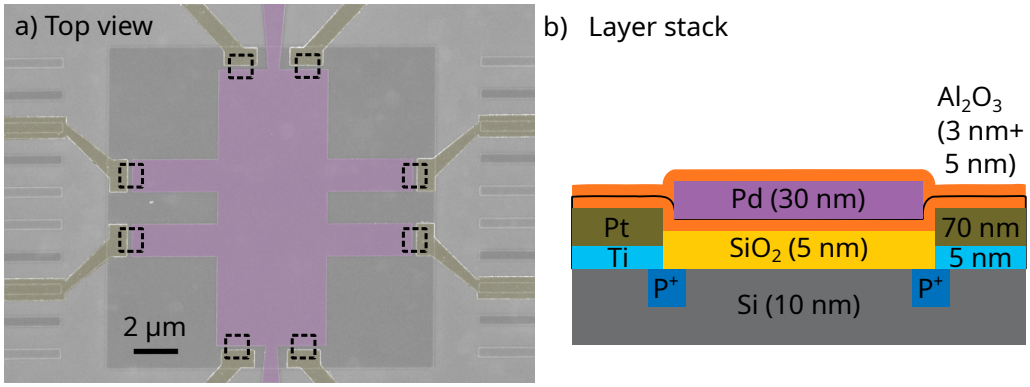

Figure 3.3: Academic process a) Top view of a hall bar used for characterization of the material properties. Gates made from Ti and Pt (light grey) lead to the ohmic contacts. The ohmic contacts are depicted with dashed lines as they are not well visible in the picture. The accumulation gate is false colored in purple. **b)** Layer stack of the academic process. Based on a FD-SOI wafer with doped areas already predefined in the industrial process, ohmic contacts are formed using 5 nm Ti and 70 nm Pt. A accumulation gate is fabricated from 30 nm Pd. The different layers are isolated with 3 nm Al_2O_3 from the substrate and 5 nm for encapsulation.

3.2.4 Post-CMOS processing

In order to test the feasibility of the industrially fabricated devices as an electron spin qubit, either a superconducting stripline or a micro-magnet have to be added to the CMOS-fabricated device described in Sec. 3.2.2. As the intrinsic spin-orbit coupling in these devices is too weak to resolve coherent oscillations [Cor18], extrinsic spin-orbit coupling needs to be engineered via a micro-magnet. Alternatively, an AC magnetic field can to be generated using a superconducting stripline. Both types of structures require non-CMOS materials and processes. An integration into the industrial process might

be possible. However, the time required is much longer and the financial and personal effort much greater compared to post-processing. Therefore, post-processing is ideal to test the feasibility of different approaches by creating proof of principle devices. Based on their success the most promising approach for integration can be chosen. In addition, post-processed devices can provide valuable feedback on quantities such as coherence times and qubit driving speeds long before a CMOS compatible method for spin manipulations is implemented.
In the following, post-processing of a CMOS-fabricated device in an academic clean room is described. Solutions to the challenges of aligning the CMOS device with the tools available in an academic clean room and establishing contact are presented. A micro-magnet for efficient spin driving is added in the last layer.

Dicing and preparation

After the CMOS process described in Sec. 3.2.2, the wafer is transferred to the academic clean room. As a first step the 300 mm wafer is cleaved and diced as described in Sec. 3.2.1. The devices are thoroughly cleaned before post-processing.

Alignment

Alignment for mask based lithography such as the DUV lithography, used in the CMOS fabrication of the nanowire devices described earlier, rely on the overlap of the mask with existing alignment marks. The marks are detected using visible light aligning an entire die at once. For EBL the mark is detected using the electron beam in line scans and a built-in SEM. Global marks are used for coarse alignment and to create a focus map. The fine alignment is performed repeatedly with local marks in the vicinity of each device. The local mark needs to be contained in the same main field as the device. A main field is the area where only the electron beam is deflected, but the mechanical stage is not moved. It has typically the size of 500 µm by 500 µm. Due to the different requirements for marks used in DUV lithography and EBL, the existing marks are not suitable for precise EBL. Therefore, new alignment marks adapted for EBL have to be deposited.
8 µm by 8 µm square marks are defined for global alignment on the side of the die. Local alignment marks for EBL are placed approximately 100 µm away from the device, well within the main field. In addition, four marks sized 70 nm by 70 nm are placed approximately 1 µm away from the device (olive green in Fig. 3.4 a)). The misalignment of these new marks adapted to EBL with respect to the existing device is measured using a SEM with high resolution. In order to see the tungsten vias of the device (light green in Fig. 3.4 a)), the SEM is set to an acceleration voltage of 20 keV. As a result, a misalignment in the vertical and horizontal direction of up to 400 nm is detected. A correction is then applied to the following lithography steps that makes use of the new marks adapted for EBL.
The marks are patterned with EBL using a 200 nm thick PMMA resist with a polymer chain length of 950 k. The metalization consists of a first layer of 10 nm Ti for adhesion and a second layer of 70 nm Pt that is well visible for the EBL machine. Pt has a high density of 21.45 $\frac{\mathrm{g}}{\mathrm{cm}^3}$ and a small grain size making a great choise for EBL marks.

Contact gates

With the help of the correction found previously the CMOS device can be contacted. The tungsten vias have a pitch of 340 nm and a nominal size of 90 nm. They are therefore relatively easy to contact with EBL, however the dimensions are beyond the capabilities of the optical lithography system available in the academic clean room. As alignment remains the main challenge, squares of 250 nm size and spaced by 90 nm are patterned on top of the vias. This ensures contact even if some misalignment is still present after correction. From the squares gates that lead to bondpads are created. The gates are visible in light gray in Fig. 3.4.
The contact gates are patterned with EBL using a 200 nm thick PMMA resist with a polymer chain length of 950 k. Prior to metalization the surface is prepared with argon ion milling for a duration of 1.5 min with 250 V acceleration voltage, a beam current of 7 mA and an argon flow of 15 sccm. The gate stack consists of a first layer of 10 nm Ti for adhesion and contact plus a second layer of 70 nm Al as a gate metal for compatibility with Al wire bonding.

Isolation

Once contact to the CMOS device is established, the contact gates need to be isolated from the following layer. 12.5 nm of Al_2O_3 are deposited using plasma enhanced ALD for isolation. A thicker layer would increase the distance of the micro-magnet to the devices and therefore reducing its magnetic field gradient at the position of the quantum dot.

Micro-magnet

In order to control the electron spin via an AC electric field, the electric excitation needs to be coupled to the magnetic moment of the spin. Coupling can be achieved via a strong intrinsic spin-orbit coupling such as in silicon hole spin qubits [Mau16; Pio22]. As the intrinsic spin-orbit coupling for electrons in silicon is weak, an extrinsic spin-orbit coupling needs to be engineered. A micro-magnet provides a magnetic field gradient at the position of the electron converting the movement of the electron into an AC magnetic field in the frame of reference of the electron.
For an optimal gradient, a thick micro-magnet with a small gap is fabricated. It is connected to a bondpad so that the electrical potential of the magnet can be controlled. The bonding takes place directly on the FeCo. The micro-magnet is shown in Fig. 3.4 c).
The micro-magnet is patterned with EBL using a 350 nm thick PMMA resist with a polymer chain length of 950 k. The metalization consists of a first layer of 5 nm Ti for adhesion and a second layer of 300 nm FeCo, forming the micro-magnet. A particularity of cobalt as well as FeCo evaporation is that ionized metal atoms can be deflected onto the resist walls causing shadow evaporation and fences [Vol21]. In order to mitigate this problem the resist is only slightly thicker than the metalization in this case. This allows the lift-off to still work, while minimizing the hight of the fences that can build up. In addition, the evaporation was performed with a high deposition rate of 0.5 nm/s for improved directivity.
FeCo with a composition of $Fe_{40}Co_{60}$ is used as the ferromagnetic material of the micro-magnet. In the literature, the FeCo alloy Permendur is commonly described. It is defined

by Fe_xCo_{1-x} ($0.5 < x < 0.65$) with a magnetization at saturation of $J_S = 2.45\,T$. Permendur was not available for this work, however a large magnetization value can be assumed for the available alloy, as well.

Encapsulation and post-fabrication annealing

The devices are encapsulated in 5 nm Al_2O_3 grown by plasma enhanced ALD, subdiced and finally a post-fabrication annealing is performed. The encapsulation ensures that there is no deformation of the micro-magnet during the annealing and prevents the micro-magnet from oxidizing. The structures are verified after each lithography step using a SEM. The final check is preformed before the annealing to ensure that any damage from the exposure to high energy electrons is healed. Before the final annealing step, the device is subdiced into 3 mm by 3 mm pieces to fit into the experimental setup. One cut is made as close as possible to the gate that is connected to the RF line for minimal signal losses due to the bondwires.
Finally, the device is annealed for 5 min at 350 °C in a forming gas atmosphere. On test devices the importance of the post-fabrication annealing has been verified. A significant improvement in the overall charge stability is observed in agreement with [Spr16]. However, it remains unclear, why the annealing shows an important effect in this case. In ref. [Spr16] the effect is explained by hydrogen trapped in the ALD grown Al_2O_3 that passivates defects present in the Si/SiO_2 interface. The Si/SiO_2 interface in the case of post-processing is buried under 200 nm SiO_2, the gate stack and the spacers. Therefore, the hydrogen can not reach the interface. In addition, an annealing step has been included at the end of the CMOS process passivating the Si/SiO_2 interface already. The effect in this case might come from healing defects at the interface between the contact gates and the SiO_2 polished by CMP or from curing damages due to ebeam exposure. Alternatively, an incomplete annealing at the end of the CMOS process could explain the effect.

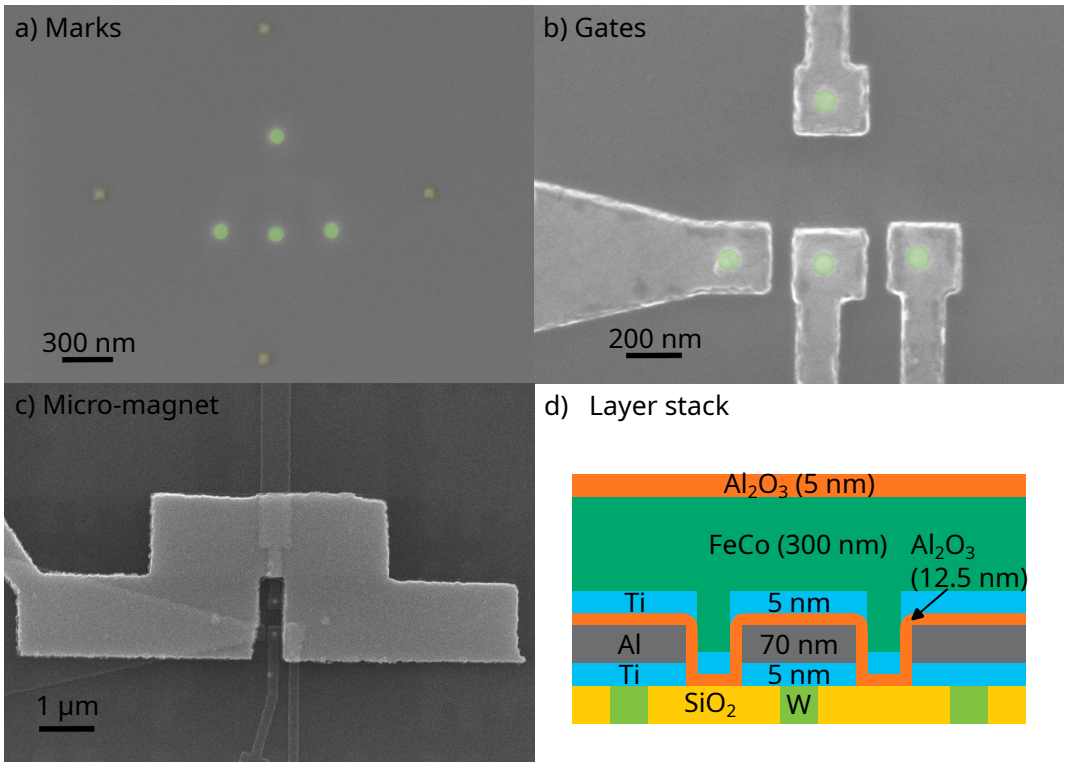

Figure 3.4: Post-processing a) Marks and alignment. The tungsten vias from the CMOS process are highlighted in light green. The marks are post-processed from Ti and Pt and are false colored in olive green. **b)** Using the shift determined with the marks in a), Ti/Al gates are deposited on top of the vias (light gray). **c)** After isolation with ALD grown Al_2O_3, a Ti/FeCo micro-magnet is deposited. **d)** Layer stack of the post-processed device including isolation/encapsulation layers.

3.3 Cryogenics

The energy scales probed when investigating quantum effects are typically much smaller than the thermal energy at room temperature of about 25 meV. For quantum dot based spin qubits, the first quantum effect that can be observed is Coulomb blockade. Here, the charging energy E_C needs to be much larger than the thermal energy k_BT. For typical charging energies of a few meV Coulomb blockade becomes visible starting from 10 K. In order to measure the spin state of an electron via energy selective readout, the Zeeman energy E_Z needs to fulfill $E_Z \gg k_BT$. For large magnetic fields this requirement is already fulfilled at temperatures of about 1 K. However, for smaller magnetic fields lower temperatures are required. Therefore, the devices need to be cooled down in special cryostats which are presented in this section. A simple immersion refrigerator is used for short cool downs, a ^{3}He cryostat is used for in-depth characterization and a dilution refrigerator is used for spin measurements and spin manipulation. Here, only a short introduction into working principle of the cryostats is given. More information can be found in Ref. [Zu22].

3.3.1 Immersion refrigerator

The simplest cryostat used in this thesis is a immersion refrigerator also called dipstick. It consists of a long rod with a sample holder attached to it. It is then inserted into a tube which is evacuated subsequently. The dipstick is immersed into a dewar filled with liquid ^{4}He and thermalization is achieved by adding He as an exchange gas into the tube. A minimum temperature of 4.2 K can be reached, corresponding to a thermal energy $k_\mathrm{b}T = 0.36\,\mathrm{meV}$. Typical charging energies are in the range of a few meV. As a result Coulomb blockade can be observed, however the features of the stability diagram remain broadened by temperature.
The advantage of the immersion refrigerator is the fast turnover speed, as a device can be cooled down in less than 1 h. This setup has been used to prescreen devices, characterize charge stability and to validate the post-fabrication annealing. However, the temperature is insufficient for spin related measurements and no magnetic field is available.

3.3.2 ^{3}He cryostat

For an in-depth charge characterization of the academic quantum dot devices and for the measurement of the quantum Hall effect, a ^{3}He cryostat is used. ^{3}He enters the cryostat and it is pre-cooled at the 1 K pot using pumped ^{4}He. Thereby, the ^{3}He is liquefied and it is collected in the ^{3}He pot. Evaporative cooling is exploited to cool down the sample by pumping the liquid ^{3}He using a primary pump and a turbo pump.
A theoretical temperature of 250 mK can be achieved with this technique. For the measurements in this thesis however, a temperature of about 400 mK has been reached. This temperature allows for charge sensing and stability diagrams can be resolved in great detail. For the quantum Hall effect the temperature is less critical. However, the possibility to apply a strong out of plane magnetic field up to 6 T makes this cryostat ideal for the observation of the quantum Hall effect. An additional advantage of this cryostat is a relatively fast cool down of about 1 day. The cool down time is slow compared to the immersion refrigerator, but fast compared to a dilution refrigerator.

3.3.3 Dilution refrigerator

To reach even lower temperatures, a ^{3}He/^{4}He dilution refrigerator is utilized. It uses a mixture of ^{3}He and ^{4}He that is circulated similarly to the ^{3}He cryostat. The mixture helps to overcome the limitations imposed by the vapor pressure. The dilution refrigerator used in this thesis is a KelvinoxMX from Oxford Instruments reaching a base temperature of 120 mK. The electron temperature is estimated to be around 400 mK (see Sec. 5.3).
In order to measure the spin via energy selective spin readout, while maintaining a Larmor frequency compatible with the RF setup, an external magnetic field of 0.6 T or lower is desirable. The temperature associated with 0.6 T is $\frac{g\mu_B B}{k_B} = 0.8\,\mathrm{K}$. The spin manipulation itself is less critical regarding the temperature. In addition to the low temperature, the 3D vector magnet is important for spin manipulation, as it allows to apply an in plane magnetic field of up to 3 T along the direction of the micro-magnet. Therefore, this cryostat has been used for spin measurements and spin manipulation.

3.4 Measurement setup

In order to control the charge occupation of a quantum dot down to the last electron, readout the spin state of an electron and manipulate the spin coherently, a multitude of control signals needs to be send to the device. For charge control a small bias voltage (0.1-1 mV) needs to be applied to the source of the device. Larger voltages in the range of a few volts are applied to the gates. However, small deviations need to be precisely controlled as well. Finally, large constant voltages up to 5 V need to be applied to the micro-magnet and the back gate. These DC voltages need to be set in synchronization with the RF pulses for spin manipulation. In addition, current flowing through the device has to be recorded in a synchronized manner as well.
In this section the electronics and the software necessary to fulfill these requirements are discussed. The electronics to generate DC voltages and RF signals are shown first. The data acquisition is explained next and the magnetic field control is discussed. Last, the measurement and analysis software is presented.

3.4.1 Electronics

The electronic setup is shown in Fig. 3.5 as a flow chart. The exact setup varies between the different cryostats. For instance characterization experiments do not require RF signals and the data acquisition is realized with a different instrument when using the immersion refrigerator. Here, the electronic setup of the dilution refrigerator for coherent spin manipulations (see chapter 5) is presented.

Experiment structure

An experiment is defined on the computer, which sends the desired configuration to the RF source, the arbitrary waveform generator (AWG) and the field-programmable gate array (FPGA). The FPGA then triggers the AWG to send pulse sequences, starts the analog-to-digital converter (ADC) for data acquisition and sets the digital-to-analog converter (DAC). The FPGA therefore has a central role in synchronizing the different parts of the experiment. It works with a clock cycle of 16 µs setting a lower time limit to each step in the experiment. Faster pulse sequences necessary for spin manipulation are realized with the AWG that modulates the signal generated by the RF source via an IQ mixer. The current flowing through the device is converted and amplified with an IV-converter. The resulting voltage is digitized via an ADC triggered by the FPGA.

DC voltages

The DC voltages for the source, the gates, the micro-magnet, the back gate and the LED are applied via an in-house build (DAC). It is based on the LTC2642 modules from Linear Technology. The DAC is set by the FPGA enabling to set constant voltages, voltage ramps and arbitrary voltage pulses.
Values inside a range of ±5 V can be set with a resolution of 153 µV. For a finer resolution a voltage divider or adder can be used. The DAC can be set fast with a rate of 2.5 V/µs while maintaining a noise level of $25\,\mathrm{nV}/\sqrt{\mathrm{Hz}}$. All DC voltages applied to the device are filtered by two low pass filters before entering the cryostat. The filters are the models VLFX-80 and SLP-1.9+ from Mini-Circuits with cutoff frequencies of 80 MHz and 1.9 MHz

respectively.
The signal send to the source is divided by 100 using a voltage divider to set a small bias voltage. The gate voltages B_1 and T_1 are composed of two DAC channels (V_1, V_2) combined via a $V_1 + \frac{1}{50}V_2$ voltage adder. With the adder a large voltage can be combined with a small deviation necessary for precise to charge control. The potential of the micro-magnet, as well as the back gate are controlled directly by a DAC output. In addition, a LED is mounted on the PCB that is controlled via an unfiltered DAC output.
Up to 40 DC lines are available in the cryostat to bring signals from room temperature to the device at 120 mK. Two types of cables are used to connect the device. Constantan wires composed of a copper-nickel alloy are used for the source, the drain and the micro-magnet. They have an almost constant resistivity from room temperature to cryogenic temperatures and they can be thermally anchored easily. As the wires are integrated into a capillary filled with Ecosorb powder for filtering, the constantan wires are prone to crosstalk at frequencies above 1 MHz. Thermocoax coaxial cables are used for the gates and the back gate. These cables enable fast changes in of the gate voltages within a bandwidth from DC to 100 MHz. Additionally, crosstalk is suppressed as the cables are shielded and separated. The DC voltages are delivered via spring loaded pin contacts to a PCB. Aluminium bondwires then connect the device to the PCB. For the gate B_1 not only a DC voltage is applied, but also RF signals are send to this gate using a bias tee. The bias tee consists of a capacitor of 100 pF and a resistor of 1 kΩ resulting in a cutoff frequency of $f_c = \frac{1}{2\pi RC} = 1.6\,\text{MHz}$.

RF signals

For spin manipulation pulsed RF signals in the range of 15 GHz to 17 GHz need to be send to the device. A continuous carrier signal is generated by the SMB 100A signal generator from Rohde & Schwarz. The amplitude and frequency are directly controlled by the measurement software. The signal is fed into the local oscillator (LO) port of the AM150175A IQ mixer from Polyphase Microwave. The signal is modulated via pulses generated by a Tektronix AWG5014C. Two channels are used to control the in-phase I and quadrature component Q of the mixer. The resulting RF signal is send to the cryostat, where silver-plated stainless steel RF cables bring the signal from room temperature to the mixing chamber. The signal is attenuated by 10 dB at the 4.2 K stage and by 1 dB at the mixing chamber (120 mK) for thermalization. Attenuators for cryogenic applications from XMA corporation are used.
The attenuated signal reaches the RF connector on the PCB where it is guided to the device via bias tee. The bias tee consists of a capacitor of 100 pF and a resistor of 1 kΩ resulting in a cutoff frequency of $f_c = \frac{1}{2\pi RC} = 1.6\,\text{MHz}$. The RF signal is then transmitted to the device using two bondwires for optimal transmission.

Thermalization From the attenuators placed in the cryostat and the attenuation of the cables, the thermal noise at the sample can be calculated and the electron temperature can be predicted. The noise created by the thermal movement of the charge carriers in a resistor is described by Johnson–Nyquist noise. The root mean square (RMS) of the

voltage fluctuation v_n is given by eqn. 3.1.

$$v_n = \sqrt{4k_BTRB} = \sqrt{4k_B \cdot 293.15\,\mathrm{K} \cdot 50\,\Omega \cdot 20\,\mathrm{GHz}} = 127\,\mu\mathrm{V} \tag{3.1}$$

With k_B being the Boltzmann constant, T the temperature, R the resistance or the impedance for high frequencies and B the bandwidth. For a room temperature of 20 °C, an impedance of 50 Ω and a bandwidth of 20 GHz v_n equates to 127 µV. The bandwidth is set to 20 GHz, as the attenuators are rated for up to 18 GHz and the cables inside the cryostat are rated for up to 20 GHz. Next the voltage fluctuation is converted into power P using eqn. 3.2.

$$P = \frac{v_n^2}{R} = 4k_BTB \tag{3.2}$$

The attenuation $Att(f)$ inside the cryostat is expressed by eqn. 3.3. The frequency dependent part describes the attenuation coming from the cables and the constant 11 dB can be attributed to the attenuators. The frequency dependence measured at room temperature with a vector network analyser (VNA) up to a frequency of 13.6 GHz. The contribution of the PCB to the attenuation is not taken into account and the dependence is interpolated for frequencies larger than 13.6 GHz.

$$Att(f) = -\frac{7\,\mathrm{dB}}{6\,\mathrm{GHz}} f - 11\,\mathrm{dB} \tag{3.3}$$

Using the power at room temperature $P(T_{RT})$ as a reference, the power spectral density $S_{att}(f)$ after attenuation can be calculated with eqn. 3.5.

$$S_{att}(f) = P(T_{RT})/B 10^{\frac{Att(f)}{10}} = 4k_BT_{RT}10^{\frac{Att(f)}{10}} \tag{3.4}$$

By integrating eqn. 3.4 over the bandwidth, the total power after attenuation can be calculated (eqn. 3.5).

$$P_{tot} = 4k_BT_{RT}\int_0^B 10^{\frac{Att(f)}{10}}\,df \tag{3.5}$$

When transforming the power back to the total voltage fluctuation after attenuation eqn. 3.6 gives $v_{n,tot} = 15.4\,\mu\mathrm{V}$.

$$v_{n,tot} = \sqrt{P_{tot}R} = 15.4\,\mu\mathrm{V} \tag{3.6}$$

In a last step, the voltage fluctuation is transformed into temperature. In order to estimate the resulting electron temperature the voltage fluctuation is multiplied by the gate lever arm α_G. Hence, only the noise felt by the electrons and not by the gate is taken into consideration. With $\alpha = 0.28\,\mathrm{V/eV}$ determined experimentally in Sec. 5.3, the electron temperature is estimated to be 50 mK.

$$T_e = \frac{\alpha_G e v_{n,tot}}{k_B} = 50\,\mathrm{mK} \tag{3.7}$$

The value for the electron temperature is much lower than the value of 400 mK determined

experimentally in Sec. 5.3. As the base temperature of the cryostat is at 120 mK, the electron temperature is not limited by thermal noise. However, the thermalization of the inner conductor of the RF cable can be still problematic. The temperature gradient from room temperature to cryogenic temperatures may cause the sample to heat up, the attenuators do not conduct heat sufficiently or their thermal anchoring is insufficient. The thermalization might be improved by adding more attenuation in the cryostat. However, the signal strength arriving at the sample would decrease accordingly and therefore reduce the Rabi frequency further. Also, a bandpass filter could be installed at low temperatures. This way only relevant frequencies for the experiments from 15 GHz to 17 GHz would contribute to the thermal noise and the electron temperature, at the same time longer RF pulses would be degraded significantly by the filtering.

Data acquisition

The current flowing through the device is measured at the drain D. The current signal is converted into a voltage signal and amplified using a custom made IV-converter based on the operational amplifier OPA141. An amplification of 10^7 V/A is chosen as a compromise between the bandwidth of 100 kHz and the SNR obtained in the experiment. The voltage signal is measured and digitized using the National Instruments USB-6229 ADC card. The maximum sampling rate of 250 kS/s is used before averaging over the desired measurement time of 50 µs per point. The acquisition is triggered by a trigger pulse from the FPGA. The results are temporarily stored in a buffer for the first measurement dimension and then returned to the computer to be saved permanently. The measured voltage is transformed back into a current on the computer.

Magnetic field control

The dilution refrigerator is equipped with a 3D vector magnet with a maximum magnetic field of 6 T out of plane and 3 T in plane. For this experiment only the in plane axis that is aligned with the micro-magnet is used. The coils are controlled by a MercuryiPS magnet power supply from Oxford Instruments. The field is set to a constant value for each experiment. The coil is separated from the leads and the current in the leads is ramped to 0 A after each change in magnetic field to minimize noise.

3.4.2 Software

A custom measurement software is used to control and measure the device. In a Python program the experiment is defined. The parameters for the RF source and the waveforms for the AWG are directly send from the Python program to the instruments. The experiment itself can be composed of time traces, voltage ramps, arbitrary pulses and trigger events. The experiment is stored in a so called batch file and then send to a LabVIEW program. The LabVIEW program then programs the FPGA and reads the buffer of the ADC.
In addition, a feedback loop to recalibrate the Larmor frequency has been implemented for this thesis. A flag in the LabVIEW program informs the python program that the experiment has finished and that a new experiment or a calibration measurement can be launched. This method is currently limited by the time it takes to acquire enough data for a meaningful measurement of the Larmor frequency. However, with an improved SNR and reflectrometry readout one can envision much faster acquisition speeds. Then

the communication between the LabVIEW program and the FPGA in the order of a few seconds becomes limiting. A direct communication between the Python program and the FPGA is currently under development. This will reduce the communication time to a few microseconds.
The data is saved in a Hierarchical Data Format (.h5) for efficient storage. The results are analyzed using Python in particular the libraries Matplotlib, NumPy and SciPy. In addition, a MATLAB based program is used for a first visualization of the results.

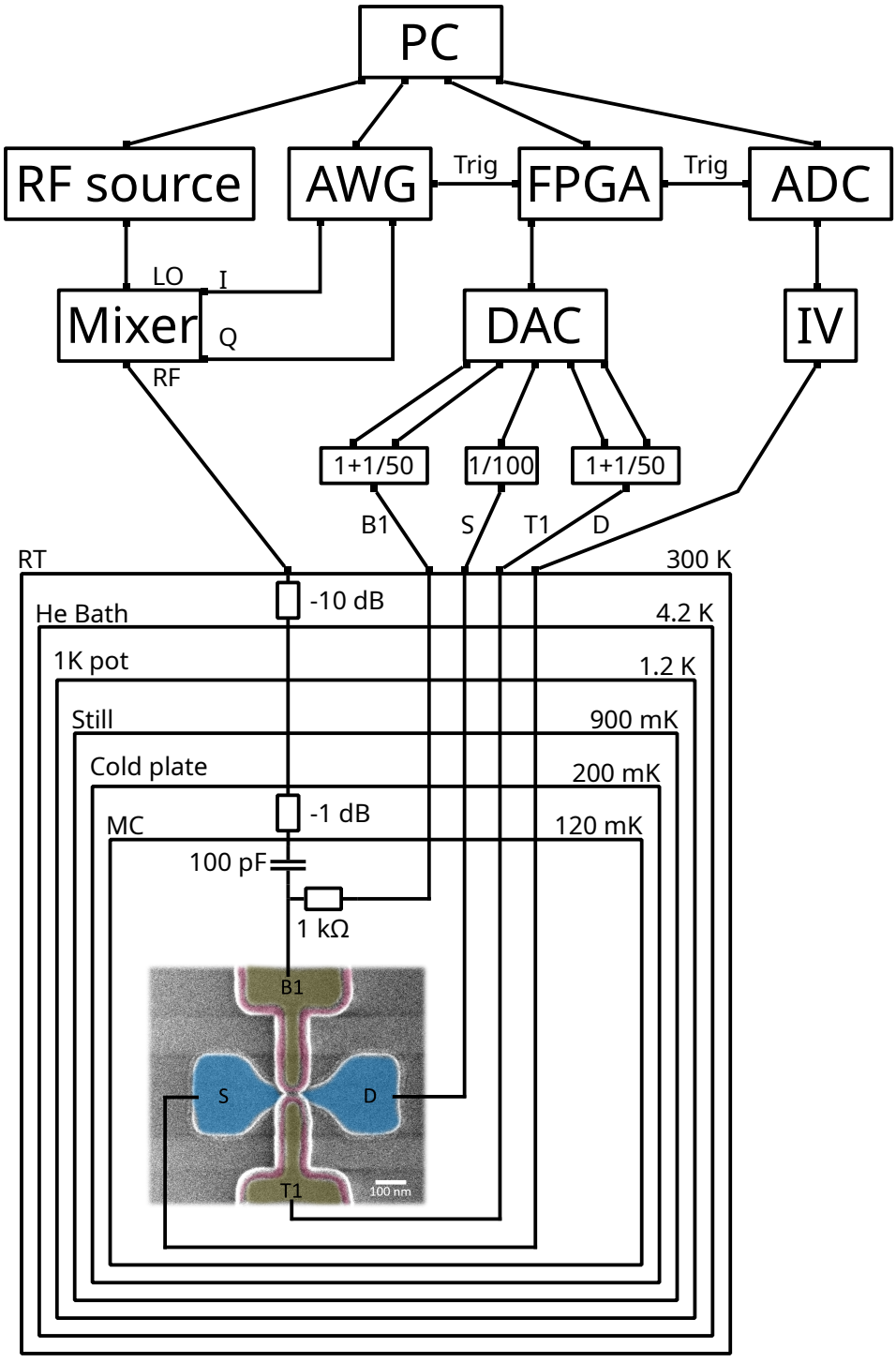

Figure 3.5: Measurement setup An experiment is defined on the computer, which sends the desired configuration to the RF source, the AWG and the FPGA. The FPGA then triggers the AWG to send pulse sequences, starts the ADC for data acquisition and sets the DAC. Faster pulse sequences are realized with the AWG that modulates the signal generated by the RF source via an IQ mixer. The current flowing through the device is converted and amplified with an IV-converter. The resulting voltage is digitized via an ADC.

CHAPTER 4

Characterization

4.1 Introduction

During the development of new devices, tests need to be carried out in order to characterize their basic properties and ensure the reproducibility and scalability of the process. The fabrication of classical CMOS devices is usually monitored by parametric tests at room temperature using probe stations. These tests reveal transistor characteristics such as the threshold voltage, subthreshold slope and leakages. For quantum devices however many relevant properties only become visible when measured at low temperatures and high magnetic fields. Also many of the transistor characteristics change at low temperatures. Hence, qubit devices need to be characterized with different methods and in particular at low temperatures.
At CEA-Leti this problem is approached with cryogenic probe stations. A small and manual cryogenic probe station is available for low volume characterization at die level from room temperature to 4 K. Recently, CEA-Leti acquired a cryogenic wafer prober that allows for high volume characterization at wafer level at temperatures as low as 2 K. With these probe stations parametric testing can be performed at low temperatures. In addition, basic quantum dot measurements and noise measurements can be performed [Con22].
Measurements requiring large magnetic fields are not possible prohibiting spin readout and manipulation, but also quantum Hall measurements. For this type of characterizations single devices measured in research cryostats using wire bonding are the only option. This approach is pursued in this thesis using an immersion refrigerator at a temperature of 4 K and ^{3}He cryostat with a magnetic field up to 5.5 T at a temperature of 400 K presented in Sec. 3.3.1 and 3.3.2.
In this chapter the design of Hall bars and quantum dot devices based on the same substrate as the industrial devices, but made with academic fabrication techniques are shown in Sec. 4.2. Basic transistor characteristics at different temperatures are extracted in Sec. 4.3. Properties related to the quantum Hall effect are characterized in Sec. 4.4. Finally, quantum dot measurements are performed on the devices made by academic fabrication and the results are compared to post-processed industrial devices in Sec. 4.5.

4.2 Device design

In this section the fanout of coarse gates common to all devices is presented first. Then the design of Hall bars, followed by the design of quantum dots devices is presented. The intention is to motivate the gate design taking the constraints of the existing structures into account and explain how the devices work.

4.2.1 Alignment marks, fanout and bond pads

All devices are based on an FD-SOI wafer introduced in Sec. 3.2.2. It is preprocessed by CEA-Leti creating an active area of 15 µm by 15 µm and 16 implanted areas for ohmic contacts of 1 µm by 1 µm. The active area is encircled by a dotted line with the implanted areas marked by dashed lines as shown in Fig. 4.1 a). The implanted areas are not visible in the SEM picture. The fabrication steps to pattern the active area and implant the doped areas are shown in Sec. 3.2. In addition, lines are patterned by CEA-Leti in active silicon intended for fanout, visible in dark gray on the right and left side of Fig. 4.1 a). However, these lines are not conductive enough to be used.
While the design of the devices is different inside the active area, all devices share in common that the contacts and gates are connected to bond pads far outside of the active area. Metal gates are defined connecting ohmic contacts and gates to the bond pads, taking the constrains of the existing structures into account. They follow generally every other existing silicon line mentioned before, but with a larger gate width to minimize the risk of failure for those gates. Square alignment marks of size 8 µm by 8 µm are defined to align all following layers. Fig. 4.1 c) shows the alignment marks, the fanout of gates and the bonding pads exemplary for a Hall bar.
Ohmic contacts are designed following the same principle for all devices illustrated in Fig. 4.1 a). The ohmic contact gates only contact half of the implanted area where the current enters the heterostructure. The other half overlaps with the top gate, which is isolated from the implanted area. The current can pass the small gap between ohmic contact gate and top gate due to the implantation, before the field effect of the top gate provides conductivity.

4.2.2 Hall bars

In order to study the properties and quality of the substrate and the gate layer stack, Hall bars are fabricated. They can be used to determine the resistance of the ohmic contacts and the 2DEG separately. Further they give insight in the transistor characteristics without confinement of electrons in the xy-plane. Finally, a Hall bar can be used to observe the quantum Hall effect.
A Hall bar is basically a rectangular area of active with 6 contacts. Typically, Hall bars are defined by etching the active area of a doped heterostructure such as GaAs/(Al,Ga)As. The Hall bars discussed here differ from this approach. They are defined by a top gate that accumulates electrons forming 2DEG via a positive gate voltage. In the areas where there is no gate, no voltage is applied and no 2DEG is formed as the active area is undoped. As a consequence, the edges of the Hall bar are not defined by etching, but instead by the pattering of the gate. Using a gate adds complexity to the fabrication and the measurement, but it is without alternative for an undoped heterostructure. At the same time advantages are that the influence of a realistic gate stack on the mobility can be tested and that the electron density can be tuned by the top gate voltage.
The principle of a Hall measurement is as follows: A constant current flows through the device from top to bottom. The two contacts on the top and the two contacts at the bottom are operated as one, due to the given constraints of the preprocessed wafer. The contacts on the side are used to measure the longitudinal voltage U_{xx} and the transversal

voltage U_{xy}. The longitudinal voltage is measured between the two contacts of the same side and the transversal voltage is measured between two contacts facing each other. In Fig. 4.1 a) the top gate is shown in purple and the gates for the ohmic contact are shown in olive green. The fabrication follows the description in section 3.2.
The Hall bar is designed on the limited space of the active area. It has a length of 12.8 µm, a width of 5 µm and the distance between the contacts of 3 µm. Most Hall bars in the literature are significantly longer, with a much smaller aspect ratio. For a given mobility, the width and the distance between contacts of a Hall bar influences the voltage drop of that is measured. Therefore, alternative Hall bar designs (e.g. 4.1 b)) were fabricated with widths of 5 µm or 10 µm and the distance between contacts of 3 µm or 9 µm. The main results however were obtained on the type of Hall bar presented in 4.1 a).

4.2.3 Quantum dot devices

In a next step, single and double quantum dots facing each other were designed. They are intended to demonstrate Coulomb blockade and charge sensing. On one side a single electron transistor (SET) is formed as a sensor and on the other side either a single or double quantum dot is probed. With the help of these devices the transistor characteristics for a realistic quantum dot device at low temperature can be measured and the stability diagram reveals charge traps and two level fluctuators. An example of a two single quantum dots facing each other is shown in Fig. 4.2. Panel a) is a zoom on the fine structure and panel b) shows an overview over the entire active area. The fabrication follows the description in section 3.2.
In a first layer 4 ohmic contacts for source and drain of each quantum dot are formed by the olive green gates. In layer two the quantum dot is confined by two depletion gates with a pitch of 90 nm shown in purple. Accumulation gates depicted in red create a 2DEG to bring the electrons from the ohmic contacts to the reservoirs of the quantum dot in a third layer. The same accumulation gate also controls the quantum dot potential, by overlapping with the depletion gates. In order to have independent control over each dot, the accumulation gate for the double quantum dot is split in two. Additionally, a coupling gate is added in the same layer. It couples or uncouples the two SETs in order to achieve capacitive sensing between them.

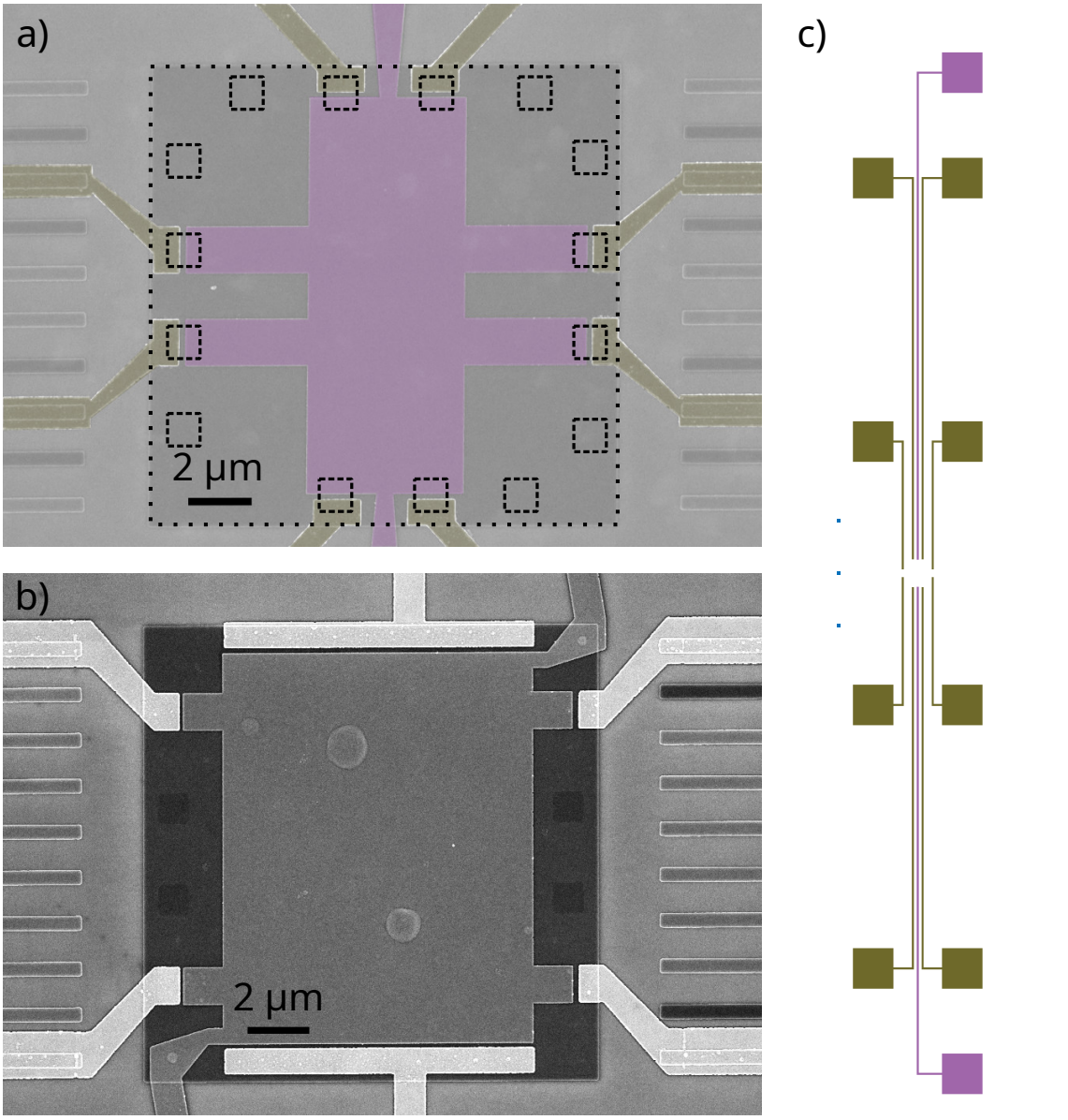

Figure 4.1: Design Hall bar a) False colored SEM image of the Hall bar used for characterization. The active area is encircled by a dotted line and the implanted areas for ohmic contacts are highlighted with dashed lines. The accumulation gate is shown in purple and the ohmic contact gates in olive green. The ohmic contact gates only contact half of the implanted area where the current enters the heterostructure. The other half overlaps with the accumulation gate, which is isolated from the implanted area. The current can pass the small gap between ohmic contact gate and accumulation gate due to the implantation, before the field effect of the accumulation gate provides conductivity. **b)** Alternative Hall bar design with a maximum width and a maximum distance between the contacts. **c)** Fanout of gates to the bonding pads for the example of a Hall bar. The accumulation gate is shown in purple, the ohmic contacts in olive green and the alignment marks are visible on the left side in blue.

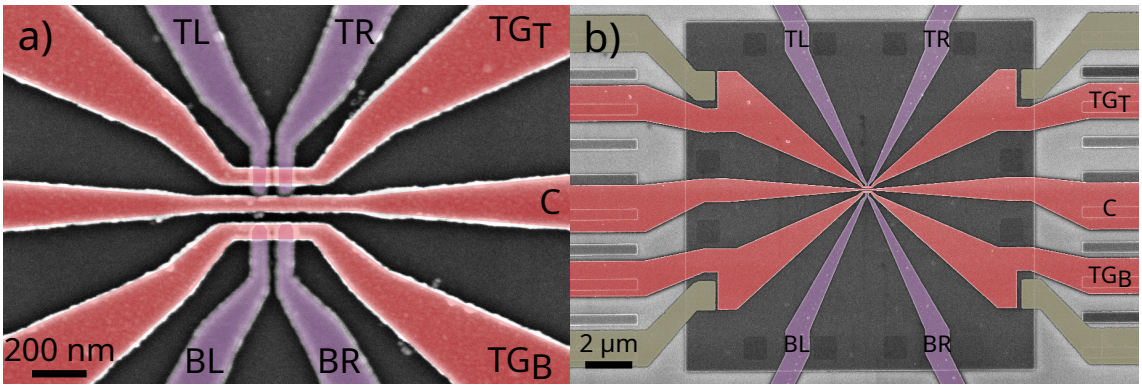

Figure 4.2: Design quantum dots a) False colored SEM image of a quantum dot device with two single quantum dots facing each other. The depletion gates TL, TR, BL, BR are depicted in purple. The accumulation gates TG_T, TG_B as well as the coupling gate C are shown in red. **b)** Overview SEM picture of the qubit device showing the entire active area. The ohmic contact gates are colored olive green.

4.3 Transistor measurements

An initial test performed on every device is a measurement of its transistor characteristics. These measurements are repeated at room temperature, 4 K and 400 mK in order to check the functionality of the device at each temperature stage of the ^{3}He cryostat. They are performed on Hall bar devices as well as quantum dot devices.
For a first test, the source drain bias V_D is swept in the range of -10 mV to 10 mV with all gates at 0V and the source drain current I_D is measured. This measurement tests for direct leakage between source and drain or to ground. Example curves for a Hall bar device are shown in Fig. 4.3 a). No leakage current is visible in the measurements. Similar results are obtained for the quantum dot devices.
The same measurement is repeated for a fixed voltage applied to the gates that allows current to flow through the device. The resulting I_D-V_D curves are shown in 4.3 b). A voltage of 3 V was applied to the gate of the Hall bar. The current depends linearly on the source drain voltage with a small current offset that is an artifact from the IV-converter. The linear behavior indicates that the formation of ohmic contacts in the fabrication was successful. In the case of a failed contact formation a Schottky barrier can form at the metal semiconductor junction. A Schottky barrier can prohibit operation at low temperatures and for low bias voltages. From these measurements the sample resistance is determined to be 23 kΩ at room temperature and 9.2 kΩ at cryogenic temperatures. Similar behavior is also observed for quantum dot devices.
Next, the gate voltage is swept with a fixed source drain bias of 10 mV. The I_D-V_G curve has three different regimes. For negative gate voltages up to low positive gate voltages the conduction is suppressed. At a certain threshold voltage the conduction turns on exponentially, then becomes linear and eventually saturates. The turn on curves for a Hall bar are shown in Fig. 4.3 c) and for a quantum dot device in Fig. 4.3 d). For the Hall bar, the threshold voltage at room temperature is around 0.7 V, while it is around 1 V at 4 K and 400 mK. Despite the higher threshold voltage, the curve rises steeper and reaches a even higher level of current for the same maximum gate voltage at lower temperatures. From a fit of the first points at the onset of conduction the inverse subthreshold slope called subthreshold swing S is extracted. The fits are depicted in black in Fig. 4.3 c) and a subthreshold swing of 125 mV/dec is extracted at room temperature, 91 mV/dec at 4 K and 92 mV/dec at 400 mK. The subthreshold swing can be compared to its theoretical minimum from Eq. 4.1.

$$S = \ln(10)\frac{k_b T}{e}\left(1 + \frac{C_{2DEG}}{C_{ox}}\right) \tag{4.1}$$

k_b is Boltzmann's constant, T the temperature and e the electron charge, C_{2DEG} the capacitance of the 2DEG and C_{ox} the gate oxide capacitance. The minimum subthreshold swing at room temperature is 60 mV/dec and about 1 mV/dec and 0.1 mV/dec at 4 K and 400 mK respectively. The measured subthreshold swing shows a similar trend with temperature, but at higher values overall. It indicates that the ratio of C_{2DEG} and C_{ox} is not ideal for a transistor, however the focus for this device is the use as a Hall bar. For the temperature dependence of both the threshold voltage and the subthreshold swing, the values stagnate a temperatures below 4 K which is attributed to the freeze out of phonons.

For the quantum dot devices the turn on happens also for higher voltages at lower temperatures. However, the rise at the threshold is not steeper and a plateau in conductance is reached at low currents. In addition, the turn on curve at 400 mK shows Coulomb peaks, indicating the formation of a quantum dot which limits the transistor performance.

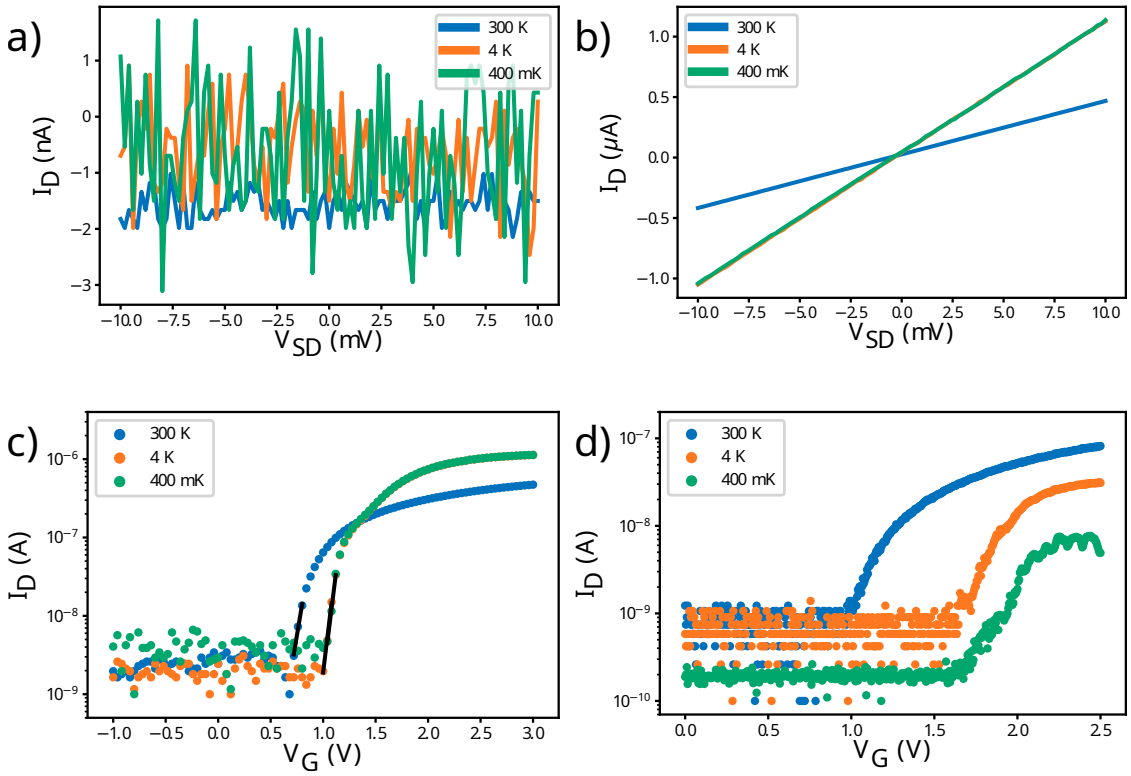

Figure 4.3: Transistor characteristics a) Leakage tests for a Hall bar with the gate voltage fixed at 0 V. No leakage is visible. **b)** I_D-V_D curve for a Hall bar with the gate voltage fixed at 3 V. All curves are linear which is an indication of the successful formation of ohmic contacts. **c)** I_D-V_G characteristics for a Hall bar with the source drain bias fixed at 10 mV. The current is plotted in a logarithmic scale and the data is shifted sightly to compensate for the negative offset originating from the IV-converter. After a region of no current the conduction turns on steeply at the threshold voltage before saturating for even larger gate voltages. The turn on happens at higher voltage for lower temperatures, but the rise is steeper. The black lines mark the fits of the subthreshold slope. **d)** I_D-V_G characteristics for a quantum dot device with the source drain bias fixed at 10 mV and the depletion gates are fixed at 2 V. The current is plotted in a logarithmic scale and the data is shifted sightly to compensate for the negative offset originating from the IV-converter. The turn on behavior deviates from the expected transistor characteristics and first Coulomb peaks become visible at low temperatures. All measurements were repeated at room temperature (blue), 4 K (orange) and 400 mK (green).

4.4 Hall bar measurements

In this section, the gate stack and the substrate are characterized using a Hall bar. First, 2 and 4 terminal resistance measurements are performed. Then, the classical Hall effect and the quantum Hall effect with conductance plateaus and Shubnikov de Haas oscillations are investigated. Finally, the effects of weak localization and weak anti-localization are explored. For a detailed description of the classical and quantum Hall effect the reader is referred to the book of Gross and Marx [Gro18]. Here the Hall effect serves mainly as a tool to characterize material and device properties. The analysis of material properties that are extracted from the measurements follows in part Ref. [Sab19].
Measurements of the 4 terminal resistance and the Hall effect are performed using two synchronized SR830 lock-in amplifiers from Stanford research systems. The setup for Hall bar measurements is illustrated in Fig. 4.4.
The current is fixed to a constant value to obtain a voltage measurement that is directly proportional to the resistance of the 2DEG. In order to convert the given voltage source into a current source, a 1 MΩ resistor is placed in series with the sample. The resistor is chosen, because it dominates the resistance of the sample of typically tens of kΩ. Therefore, it fixes the current to about 5 nA for a bias voltage of 5 mV applied. Figure 4.5 a) shows the current flowing through the device and resistor in series as a function of accumulation gate voltage. For gate voltages from 0 V to 1.2 V the current is essentially 0 as there are no electrons accumulated in the 2DEG yet. Then, while increasing the accumulation gate voltage the current increases rapidly to 4 nA as metallic conduction becomes possible. The resistance of the sample becomes comparable with the 1 MΩ resistor. For even higher voltages, the current increases slowly and saturates at large gate voltages. At this point the 1 MΩ resistor dominates, fixing the current effectively to ≈ 4 nA.

4.4.1 2 and 4 terminal resistance measurements

The 2 and 4 terminal resistance can be obtained from basic measurements using a Hall bar. A 2 terminal measurement probes the total resistance of the device and setup, while a 4 terminal measurement allows for a separate measurement of the resistance of contacts and the 2DEG.
A two terminal measurement from one contact to another yields the resistance of the contacts and the 2DEG measured in series. The two terminal resistance is extracted from I_D-V_D curves such as the one presented in Sec. 4.3. In this example a 2 terminal resistance of 9.2 kΩ is obtained. However, it is impossible to separate the contact resistance from the resistance of the 2DEG with this technique.
When splitting the current and voltage measurement into separate measurements as depicted in Fig. 4.4, only the resistance of the 2DEG in between the inner contacts is probed. This technique is called a 4 terminal resistance measurement. The voltage drop between the inner contacts is called longitudinal voltage U_{xx} and the corresponding resistance is called longitudinal resistance R_{xx}. The longitudinal resistance is then converted into the sheet resistance R_S by multiplying with the aspect ratio $\frac{w}{l} = 1.7$. $l = 3\,\mu$m is the length between the inner contacts and $w = 5\,\mu$m is the width of the Hall bar. It is shown as a function of gate voltage in figure 4.5 b). The voltage drop is 0 for gate voltages below ≈ 2.1 V. At about 2.1 V U_{xx} increases rapidly. At this point the lock-in amplifier starts working

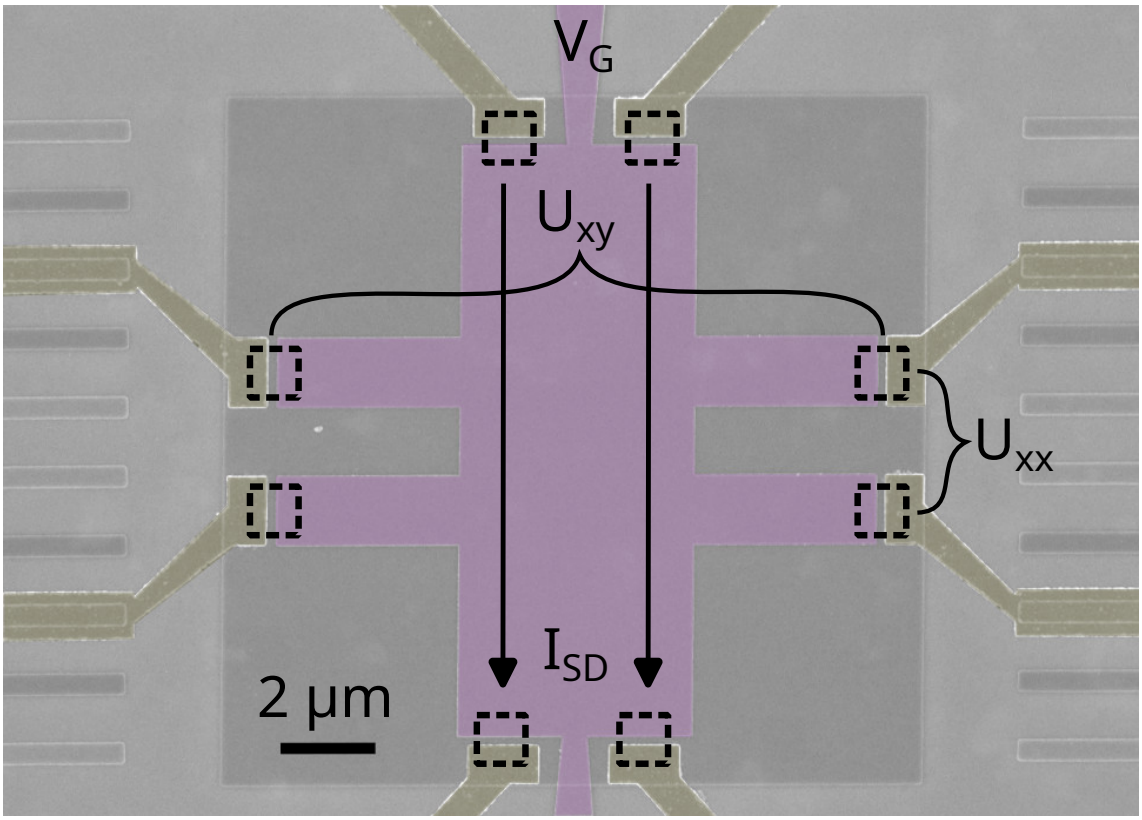

Figure 4.4: Setup Hall bar A constant current I_{SD} of 4 nA flows through the Hall bar from the top contacts (source) to the bottom contacts (drain) for a sufficiently large voltage V_G applied to the accumulation gate (purple). The longitudinal voltage U_{xx} is measured between two contacts on the same side, while the transversal voltage U_{xy} is measured between two contacts facing each other.

as intended. Subsequently, U_{xx} and therefore R_S reduces, as more and more conduction channels become available. A minimum sheet resistance of 530 $\frac{\Omega}{\text{sq}}$ is reached at ≈ 3.5 V of gate voltage. For higher gate voltages the resistance of the 2DEG increases again. The electron wave functions are squeezed against the top interface and become more sensitive to the surface roughness which acts as scattering centers.
Comparing the 2 terminal resistance and the 4 terminal resistance, reveals that the total device resistance is dominated by the contact resistance. Therefore, the contact resistance is estimated to be 4.3 kΩ per contact. Most likely the limiting factor is the resistance of the ohmic contacts that are only 0.4 µm by 1 µm in size. Larger implanted areas that are tailored for a Hall bar with large contacts for source and drain would help to improve the contact resistance of Hall bars. The design and fabrication process for the industrial devices is different, leading to significantly smaller contact resistances in range of 100 Ω. Generally, larger implanted areas with more distance to each other would be desirable to improve the ohmic contacts for all devices.

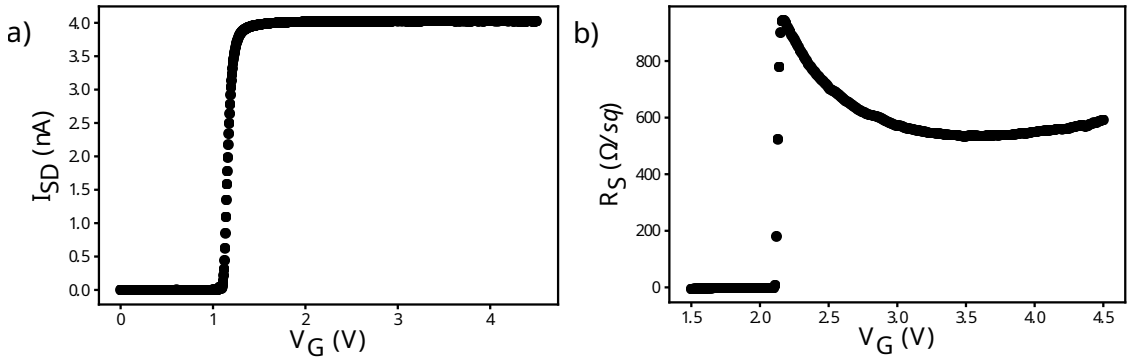

Figure 4.5: 4 terminal resistance a) Current flowing through the device and a 1 MΩ resistor as a function of gate voltage V_G. At about 1.2 V the device becomes conductive and the current rises rapidly to 4 nA, limited by the 1 MΩ resistor. **b)** Sheet resistance R_S as a function of gate voltage. Once the lock-in measurement works as intended at 2.1 V the sheet resistance deceases to a minimum, as more and more conduction channels become available. The following increase is explained by the electron wave function being squeezed against the top interface.

4.4.2 Hall effect

In order to measure the Hall effect, the longitudinal voltage U_{xx} and the transverse voltage or Hall voltage U_{xy} are extracted. The Hall bar is measured in an out-of-plane magnetic field. U_{xx} is measured on one side of the Hall bar in between the two inner contacts. U_{xy} is measured across the Hall bar with one contact on each side. An image of a Hall bar with the voltage measurements marked is depicted in Fig. 4.4.
The classical Hall effect describes the production of a transverse voltage that depends linearly on the magnetic field. The quantum Hall effect manifests in the form of conductance plateaus in the transverse voltage, as well as Shubnikov de Haas (SdH) oscillations in the longitudinal voltage. Both Hall effects give access to the electron density and mobility, two important material properties of the 2DEG. With the quantum Hall effect the Landau levels can be mapped and the spin and valley degeneracy can be probed.

Classical Hall effect

The Lorentz force acts on charge carriers flowing through a conductor in a magnetic field perpendicular to the current. As a result the charge carriers are deflected to one side of the conductor resulting in a measurable transversal voltage. This phenomenon is called the classical Hall effect which can be measured in any conductor or semiconductor. The transversal voltage U_{xy} and therefore the transversal resistance R_{xy} depends linearly on the magnetic field, where the slope allows to determine the charge carrier density n_s. Eq. 4.2 describes the magnetic field dependence of the transversal resistance for electrons as charge carriers in a 2D conductor, with I being the current and e the electron charge.

$$R_{xy} = \frac{1}{n_s e} B \tag{4.2}$$

The red curve in Fig. 4.6 shows the transversal resistance plotted against the magnetic field. For magnetic fields below ± 3 T the dependence is linear resulting in a electron density of $(3.66 \pm 0.05) \times 10^{12}\,\mathrm{cm}^{-2}$ at a gate voltage of 2.3 V.
The longitudinal voltage measures the 4 terminal resistance as described in Sec. 4.4.1 which is independent of the magnetic field in the classical model. The blue curve in Fig. 4.6 shows the longitudinal voltage converted into the sheet resistance. For magnetic fields around 0 T a peak in sheet resistance is visible. It is followed by a range of almost constant resistance up to ± 3 T, where irregular dips and peaks, but no clear oscillations are visible. The decrease in resistance can be explained by localization effects and is studied in further detail in Sec. 4.4.3. For the mobility calculation using Eq. 4.3 the sheet resistance at zero magnetic field is taken into account.

$$\mu = \frac{1}{R_S(B=0)en_s} \tag{4.3}$$

The electron mobility for the measurement in Fig. 4.6 is $(2210 \pm 20)\,\mathrm{cm}^2/\mathrm{Vs}$, using the electron density calculated earlier. From the mobility and the density the mean free path l can be calculated following Eq. 4.5.

$$l = \mu\frac{\hbar}{e}\sqrt{2\pi n_s} = 70\,\mathrm{nm} \tag{4.4}$$

It describes the average length an electron can travel without scattering. A second length scale that can be extracted is the Fermi wavelength λ_F.

$$\lambda_F = \sqrt{\frac{2\pi}{n_s}} = 13\,\mathrm{nm} \tag{4.5}$$

It gives an estimate for the necessary confinement to observe quantization in a quantum dot.

Quantum Hall effect

The quantum Hall effect manifests in the form of conductance plateaus and SdH oscillations. It can only be observed at low temperatures, large magnetic fields and in 2D systems. The origin of the quantum Hall effect is the filling and spacing between Landau levels that depends on the applied magnetic field and the Fermi energy.

Conductance plateaus

For magnetic fields above/below ± 3 T the transversal resistance in Fig. 4.6 shows conductance plateaus. From the value of the transversal resistance on the plateau, the number of completely filled Landau levels can be calculated following Eq. 4.6. h is Plank's constant, e the electron charge and i the number of completely filled Landau levels. $R_K = \frac{h}{e^2}$ is the von Klitzing constant, which corresponds to the resistance of the last conductance plateau.

$$R_{xy} = \frac{h}{ie^2} = \frac{R_K}{i} \tag{4.6}$$

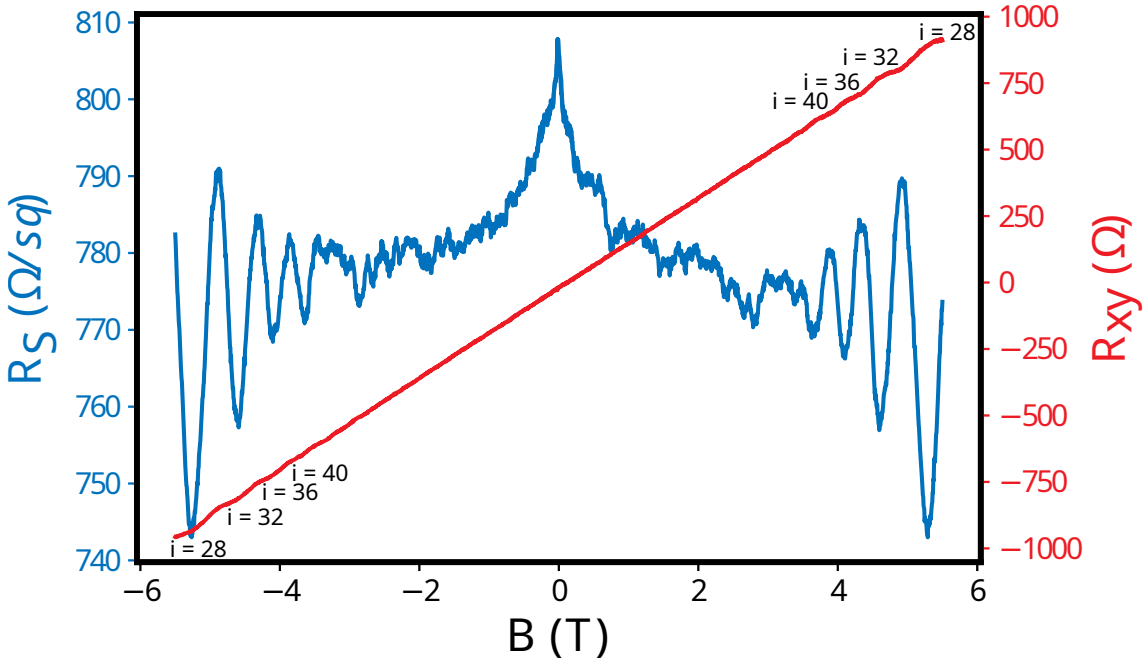

Figure 4.6: SdH oscillations and conductance plateaus In blue: Measurement of the longitudinal voltage U_{xx} converted into the sheet resistance R_S. An increase in sheet resistance is observed around B = 0 T due to weak localization. For intermediate magnetic field values up to 3 T the sheet resistance stays constant and for large magnetic field values SdH oscillations appear. In red: Measurement of the transversal voltage U_{xy} converted into the transversal resistance R_{xy}. For low magnetic fields the transversal resistance is linear and for large magnetic field values conductance plateaus are observed. The number of filled Landau levels i is indicated for each plateau. Both curves are composed of two separate measurements in order to cover the full range of magnetic field from -5.5 T to -5.5 T. For this measurement the gate is set to 2.3 V and the bias voltage to 5 mV.

The number of completely filled Landau levels is marked in Fig. 4.6. It changes by 4 for each plateau as the spin degeneracy is not lifted giving $g_s = 2$. The valley degeneracy is only partially lifted. At the Si/SiO_2 interface the 6 fold degeneracy of bulk Si is lifted into two z valleys and the four x and y valleys. The two z valleys v_+ and v_- are lower in energy, while the four in-plane valleys are well separated at higher energies. Therefore, $g_v = 2$ for the following measurements. In total the Landau levels are $g_s g_v = 4$ fold degenerate, hence the change by 4 in filling factor. Filling factors that can be resolved with the available magnetic field are in range from i = 28 to i = 40. The rather high filling factors indicate a large Fermi energy.
Each plateau corresponds to a minimum and each step to a maximum of the SdH oscillations. As the SdH oscillations are much better visible compared to the conductances plateaus, they are used for the calculation of electron density and mobility of the devices in the next section.

Shubnikov de Haas oscillations

In the measurement shown in Fig. 4.6, the sheet resistance starts oscillating with an increasing amplitude for the dips in resistances at magnetic fields above/below ± 3 T. These oscillations are called the SdH oscillations.
The first quantity that can be extracted is the electron density n_s. Formula 4.7 relates the difference in inverse magnetic field $\Delta\frac{1}{B}$ between adjacent minima to the electron density n_s. e is the elementary charge, h is Planck's constant and $g_s = 2$, $g_v = 2$ are the degeneracy factors for spin and valleys respectively.

$$\Delta\frac{1}{B} = \frac{1}{B_{i+1}} - \frac{1}{B_i} = g_s g_v \frac{e}{h n_s} \tag{4.7}$$

The four clear minima at large positive and large negative magnetic fields in Fig. 4.6 are used to calculate the electron density. For each pair of minima an electron density is calculated, resulting in an average electron density of $(3.41 \pm 0.05)\times 10^{12}\,\mathrm{cm}^{-2}$.
Equation 4.3 allows to calculate the mobility μ from the electron density. Form the electron density and the sheet resistance at zero magnetic field, the mobility for this measurement calculated to be $(2260 \pm 20)\,\mathrm{cm}^2/\mathrm{Vs}$ and the resulting mean free path is $l = 69\,\mathrm{nm}$.
By fitting the envelope of the SdH oscillations, the quantum lifetime τ_q can be extracted following Ref. [Sab19] using Eq. 4.8.

$$R_S(B) = A + \sqrt{B}\frac{\chi}{\sinh(\chi)} \exp\left(-\frac{\pi}{\omega_c \tau_q}\right) \tag{4.8}$$

$\chi = \frac{2\pi^2 k_B T}{\hbar\omega_c}$ and $\omega_c = \frac{eB}{m^*}$ is the cyclotron frequency. A is a fitting parameter to compensate the offset in sheet resistance, k_b is the Boltzmann constant, $\hbar$ is the reduced Planck constant and e is the electron charge. With the temperature T fixed to the cryostat temperature of 400 mK and the transverse effective mass $m^* = 0.19 m_e$ of silicon, the fit yields a quantum lifetime of 0.15 ps. From the quantum lifetime the Landau level broadening $\Gamma = \frac{\hbar}{2\tau_q} = 2.1\,\mathrm{meV}$ is extracted. The large broadening explains why neither the spin nor the valley splitting can be resolved in this measurement.

Density and mobility

The prior discussion was focused on the details of the SdH oscillations and the conductance plateaus for a fixed gate voltage. Here, the gate voltage is varied in order to find the optimal mobility and the corresponding density.
As a first approach, the measurements of the SdH oscillations are repeated in Fig. 4.7. The overall sheet resistance decreases with increasing gate voltage, as the 2DEG becomes more and more conductive. This corresponds to the decrease of the 4 terminal resistance described in Sec. 4.4.1. For an increasing gate voltage the frequency of the SdH oscillations increases. It reflects that the splitting and filling of Landau levels increases with increasing electron density and therefore with increasing gate voltage. The electron density as well as the mobility are extracted from the minima of the SdH oscillations. The electron density is plotted against the gate voltage in Fig. 4.9 a) and the mobility is plotted against the electron density in Fig. 4.9 b) as the red points. 6 different gate voltages and therefore

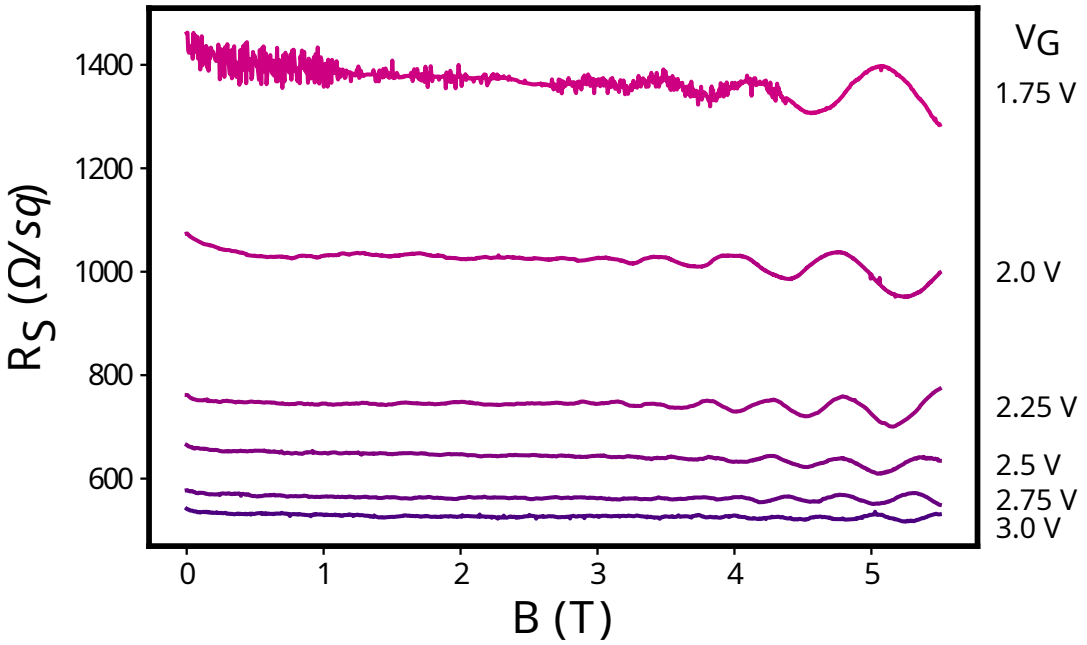

Figure 4.7: SdH oscillations for different gate voltages Measurement of the longitudinal voltage U_{xx} converted into the sheet resistance R_S against the applied magnetic field B. Each trace corresponds to a different gate voltage indicated on the right. The overall sheet resistance decreases with increasing gate voltage, as the 2DEG becomes more and more conductive.

electron densities are plotted. For each point the magnetic field is swept from 0 T to 5.5 T corresponding to a measurement time of multiple hours. This makes the method of using repeated measurements precise, but time consuming.
In an alternative approach, the gate voltage is swept and the magnetic field is changed in steps. In order for this approach to be viable, many steps in magnetic field need to be measured. Later, the SdH oscillations are reconstructed from the complete dataset. For the measurements in Fig. 4.8 560 steps in magnetic field were recorded. In addition, the device and the measurement setup need to react quickly to changes in gate voltage and the magnetic field needs to be stable over one sweep in gate voltage.
The measurements are shown in Fig. 4.8 for a gate voltage range from 1.5 V to 4 V and magnetic fields from -0.1 T to 5.5 T. In Fig. 4.8 a) the sheet resistance is measured, but the SdH oscillations are barely visible. Fig. 4.8 c) shows the derivative of the measurement in a) with respect to the gate voltage highlighting the SdH oscillations. For low accumulation gate voltages up to 2 V the electrons just start to accumulate in the 2DEG and therefore the sheet resistance still changes globally with the gate voltage. For higher gate voltages, the sheet resistance stays constant for low magnetic fields and begins to oscillate for magnetic fields above 3 T. In order to obtain the SdH oscillations, cuts along the magnetic field axis are taken. By identifying the minima of the SdH oscillations for a selection of gate voltages, lines can be fitted to the Landau levels. From these lines, the density and mobility for many gate voltages can be extracted. The resulting plot of electron density versus gate

voltage and mobility versus electron density is shown in Fig. 4.9 in blue.
In Fig. 4.8 b) the transversal resistance is plotted and the visibility of the conductance plateaus is even weaker than for the SdH oscillations. Fig. 4.8 d) shows the derivative of the measurement in b) with respect to the gate voltage highlighting the conductance plateaus. For low magnetic fields the transversal resistance increases linearly and for magnetic fields above 3 T the conductance plateaus become visible. The slope at low magnetic fields allows for extracting the electron density with the classical method. The electron density and mobility extracted from by this method is shown in Fig. 4.9 in green.
The pattern in Fig. 4.8, where the SdH oscillations and the conductance appear as rays in the 2D plot is called a Landau fan. It is a result of the simultaneous dependence of the splitting and filling of Landau levels with magnetic field and electron density. Also the filling of Landau levels can be extracted from the resistance value at conductance plateaus. The filling ranges from $i = 16$ to $i = 60$ with a jump of 4 between the visible peaks due to the spin and valley degeneracy. This confirms a rather high filling of Landau levels and that the first Landau levels are not in reach with the available magnetic field.
The electron density plotted against the gate voltage in Fig. 4.9 a) shows the same linear trend for all devices and methods. From the slope $\frac{dn_e}{dV_G}$ the gate capacitance per area $C = e\frac{dn_e}{dV_G} = 0.46\,\frac{\mu F}{cm^2}$ is extracted which matches well with the geometric capacitance $C_{geo} = 0.55\,\frac{\mu F}{cm^2}$ from Eq. 4.9

$$C_{geo} = \varepsilon_0 \left(\frac{d_{SiO_2}}{\varepsilon_{SiO_2}} + \frac{d_{Al_2O_3}}{\varepsilon_{Al_2O_3}} \right)^{-1} = 0.55\,\frac{\mu F}{cm^2} \tag{4.9}$$

ε_0 is the vacuum permittivity, $\varepsilon_{SiO_2}/\varepsilon_{Al_2O_3}$ are the relative permittivities of SiO_2/Al_2O_3 and $d_{SiO_2} = 5\,nm/d_{Al_2O_3} = 3\,nm$ are the thicknesses of the SiO_2/Al_2O_3 layer.
Next, mobility and density are plotted against each other in order to find the maximum mobility and the corresponding density. For low electron densities and therefore low gate voltages, the mobility increases rapidly. In this regime, electrons start accumulating in the 2DEG and the increasing number of electrons helps screen charged impurity and reduce Coulomb scattering. The minimum electron density for which metallic conduction is possible is called critical density or percolation density n_p. For a fit of the percolation density as in Ref. [Sab19], the data in 4.4.1 b) is insufficient at low gate voltages. Therefore, the percolation density is estimated from the first points of Fig. 4.9 b) to be in the order of $1 \times 10^{12}\,cm^{-2}$. For a density around $3.7 \times 10^{12}\,cm^{-2}$ the mobility reaches a maximum. For densities greater then $4 \times 10^{12}\,cm^{-2}$ the mobility is reduced despite the increase in electron density. For a large electron density, corresponding to a large top gate voltage, the wave function of the electrons is squeezed against the top interface. Therefore, the electrons start to feel the surface roughness, which effectively acts as scattering centers reducing the mobility. For the maximum mobility of $(2350 \pm 20)\,cm^2/Vs$ at a density of $(3.48 \pm 0.05) \times 10^{12}\,cm^{-2}$ a maximum mean free path of 72 nm is reached. The values obtained by the different methods are compared to the literature in the conclusion of this chapter.

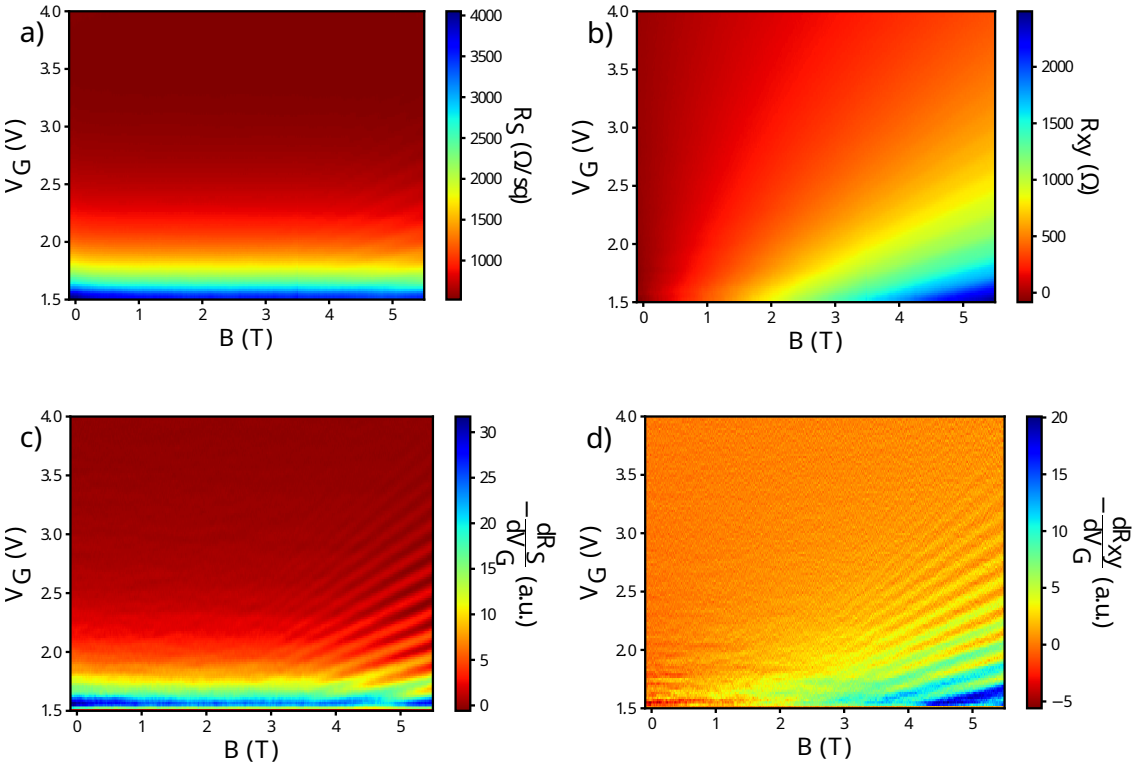

Figure 4.8: Sheet resistance and transversal resistance plotted against the magnetic field B and the gate voltage V_G a) Measurement of the longitudinal voltage U_{xx} converted into the sheet resistance R_S. **b)** Measurement of the transversal voltage U_{xy} converted into the transversal voltage R_{xy}. **c)** Derivative with respect to the gate voltage of the sheet resistance measured in a). The derivative highlights the SdH oscillations and reveals Landau levels with a filling factor from $i = 16$ (bottom) to $i = 60$ (top). **d)** Derivative with respect to the gate voltage of the transversal resistance measured in b). The derivative highlights the conductance plateaus and reveals Landau levels with a filling factor from $i = 16$ (bottom) to $i = 60$ (top).

4.4.3 Localization effects

When the electron wave function becomes localized, a positive correction to the resistivity is the result. Localization can occur due to disorder called strong localization. Alternatively, weak localization can occur when electrons self interfere during transport [Akk07]. The increased resistance around B = 0 T, visible in Fig. 4.6 indicates the presence of a magnetic field dependent localization.
Weak localization would be able to explain such a magnetic field dependent localization. The resistivity reflects the probability of an electron to propagate from A to B. Classically, this probability is the sum of the probabilities for each path. In quantum mechanics interference of the wave function has to be taken into account. Hence, closed loops in the electron trajectory that are shorter than the coherence length have to be taken into account. In the absence of spin-orbit coupling, the electrons always interfere constructively

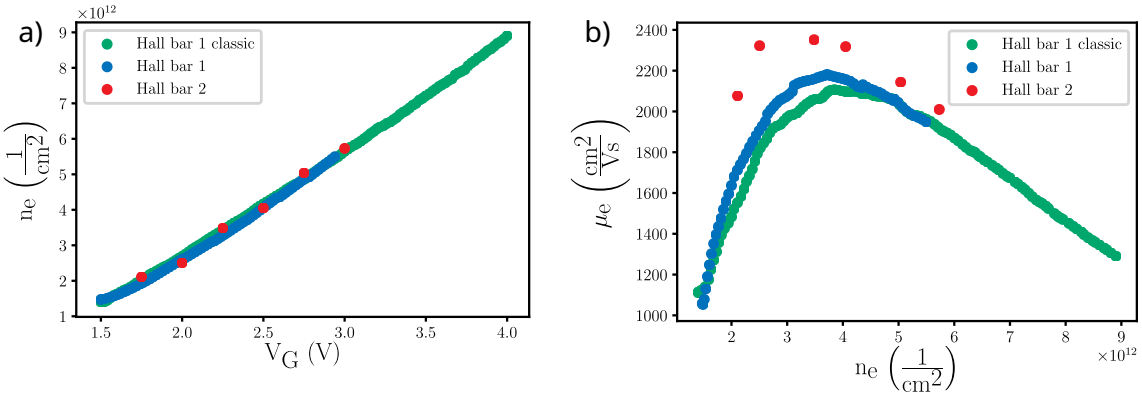

Figure 4.9: Gate voltage, electron density and electron mobility a) Electron density n_e plotted against the applied gate voltage V_G showing a linear trend. **b)** Electron mobility μ_e plotted against the electron density n_e. For the green points the electron density and mobility is extracted by the classical method from the measurements shown in 4.8 a) and c). For the blue points the electron density and mobility is extracted from the SdH oscillations from the measurements shown in 4.8 a). The red points correspond to a second Hall bar, where the electron density and mobility is extracted from the 6 measurements shown in Fig. 4.7 using the SdH oscillations.

leading to an increase of resistance. In the presence of a magnetic field, the time reversal symmetry between interfering paths is broken and the localization is suppressed.
In Fig. 4.10 the normalized sheet resistance for low magnetic fields between -0.2 T and 0.2 T for different gate voltages is depicted. These measurements are a closer investigation of the peak around B = 0 T, already visible in Fig. 4.6. The normalized sheet resistance shows a peak slightly before 0 T for all gate voltages. The peak can probably be attributed to weak localization. However, the asymmetry and the additional bumps indicate that other localization effects might be present, as well. The shift of the peak towards slightly negative magnetic fields can be attributed to hysteresis of the superconducting coil.
With increasing gate voltage the prominence of the peak decreases and therefore the signal-to-noise ratio decreases. This reduction of the signal-to noise-ratio is caused by the gate voltage squeezing the wave function of the electrons against the top interface of the 2DEG. Thereby, the influence of impurities in the oxide becomes stronger leading to a shorter coherence length. The shorter coherence length in turn reduces the number of loops contributing to the weak localization and therefore diminishes the peak in resistance.

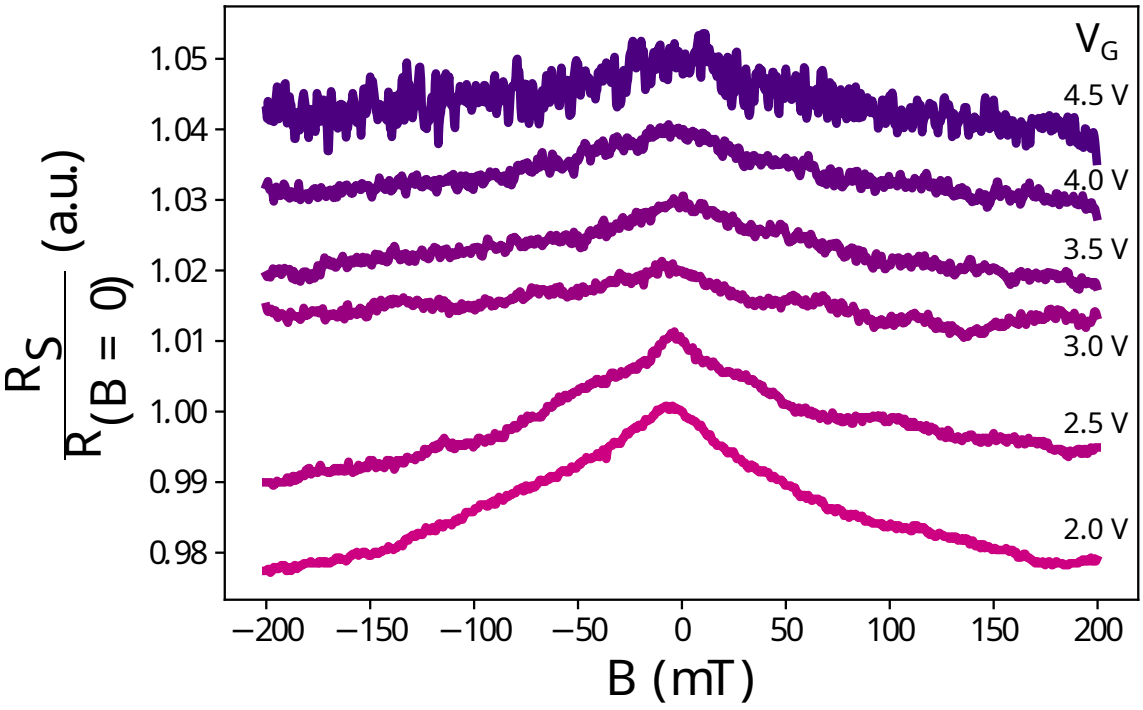

Figure 4.10: Localization effects Normalized sheet resistance $\frac{R_S}{R_{B=0}}$ at low magnetic fields B. The different Hall gate voltages are indicated on the right. The effect of localization manifests as a peak in resistance. Each curve is offset by 0.01 on the y-axis to better distinguish the measurements.

4.5 Quantum dot measurements

Hall bars probe the material properties of a large area and for many electrons accumulated in the 2DEG. Therefore, screening effects become relevant and the extracted quantities always represent an average. Quantum dots make it possible to capture single electrons in a tightly confined space. They can be therefore used to study the local properties of the substrate and the gate stack. Here, quantum dots are studied to qualitatively evaluate the use of the substrate and the fabrication process for qubit operation. The fabrication of the devices is discussed in Sec. 3.2 and the design is discussed in Sec. 4.2. The concept of a stability diagram and Coulomb diamonds is introduced in Ch. 2.

The device characterized in Fig. 4.11 a) has been fabricated on the same chip as the Hall bars presented previously in Sec. 4.4. The measurement is performed at 400 mK in the same ^{3}He cryostat used for Hall bar characterization. A stability diagram is shown where the voltage applied to the depletion gates BL and BR is varied. The accumulation gate is set to a fixed value of 2.2 V. Transitions angled approximately 45 ° are visible throughout the stability diagram. This could be an indication of a quantum dot formed in between the depletion gates with equal influence of both gates on the quantum dot potential. However, their width and spacing is much larger than expected and the transitions are bend irregularity. A zoom into one of the transitions is shown in Fig. 4.11 b). It reveals

that the transitions are composed of lines following two different slopes. This substructure indicates that three quantum dots in series are formed instead of one quantum dot. Only when the potential of all three quantum dots is aligned and inside the bias window current can flow which explains the pattern. In addition, fluctuations present in the measurement imply the presence of two level systems in the vicinity of the quantum dot. The effect of charged traps that are filled or emptied at a certain gate voltage causes the entire stability diagram to shift multiple times. Comparable results are obtained for devices fabricated on a different chip, but the same wafer. Therefore, this wafer is not suitable for the reliable formation of quantum dots.

Devices from a new wafer originating from a different batch are studied next. A batch typically consists of 25 wafers that are processed together with only small process variations between wafers. In between batches larger changes to the process are made. Hence, significant improvements are expected from a wafer from a new batch.

The characterization is performed in the immersion refrigerator at 4 K. The stability diagram shows that vertical and horizontal lines are visible indicating the formation of two independent quantum dots. The lines are tightly spaced, faint and broad which is in part due to the higher temperature, but mainly due to insufficient confinement. There are no angled lines that would indicate that the intended quantum dot formed in between the depletion gates. The device quality has improved, as no fluctuations or switches are visible. Coulomb diamonds shown in Fig. 4.11 d) are recored for one of the quantum dots. They show the expected diamond pattern, however it is overlayed with peaks originating from exited states and impurities. From the Coulomb diamonds a gate lever arm around 0.1 eV/V is extracted. Even though the formation of quantum dots is possible and the stability is greatly improved compared to the previous wafer the result is insufficient do be used for a qubit.

Further confining the electrons could improve the functionality of the devices. A design inspired by Ref. [Vel14] with an additional confinement layer has been fabricated and tested. However, the first tests failed and further development was stopped by the COVID-19 pandemic.

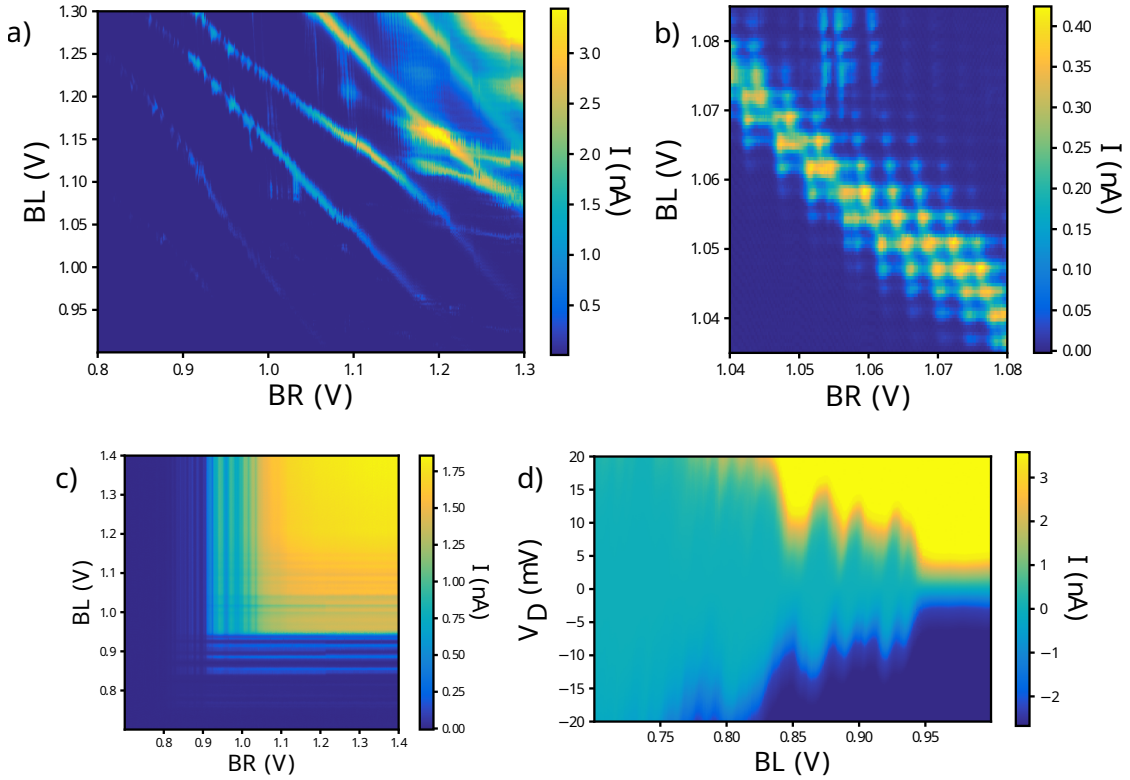

Figure 4.11: Charge stability a) Stability diagram of a quantum dot device from the same chip the Hall bar measurements were performed on. The voltage applied to the depletion gates BL and BR is varied and the accumulation gate is set to a fixed value of 2.2 V. **b)** Zoom into the stability diagram from a). **c)** Stability diagram of a quantum dot device from a new batch. **d)** Coulomb diamonds of a quantum dot device from a new batch.

4.6 Conclusion

In this chapter test structures for transistor measurements, Hall bar measurements and quantum dot formation have been successfully implemented. Devices made by academic fabrication based on a preprocessed wafer from the industrial fabrication are studied. This combination enables the characterization of devices that are not available on the regular mask set used for the industrial process.

First transistor measurements are preformed that give insights into leakage, the device resistance and the turn on behavior at different temperatures. A device resistance of 23 kΩ at room temperature and 9.2 kΩ at cryogenic temperatures is extracted from the $I_D - V_D$ curve. Threshold voltage and subthreshold swing are extracted from the $I_D - V_G$ curve. The threshold voltage at room temperature is around 0.7 V, while it is around 1 V at 4 K and 400 mK. A subthreshold swing of 125 mV/dec is extracted at room temperature, 91 mV/dec at 4 K and 92 mV/dec at 400 mK. The threshold voltage increases for lower temperatures and the subthreshold swing decreases. The subthreshold swing is well above the theoretical minimum of 60 mV/dec at room temperature and also larger than the values for a typical transistor of 70 mV/dec. The turn on behavior of the quantum dot

deviates also qualitatively from the expected transistor characteristics and first Coulomb peaks become visible at low temperatures. Nevertheless, the devices were not build with the intention to make good transistors, but good Hall bars or quantum dots. Going one step further, the electron mobility could be extracted from transistor measurements using the split C-V method [Cas06; Oha07; Rom04], but a separate measurement of the gate capacitance with respect to the gate voltage was not available for this thesis. As the split C-V technique overestimates the density and underestimates mobility [Neg11], the Hall effect can serve as reference for the mobility on these devices.
A more precise measurement of the mobility and additional insights into the properties of the 2DEG can be gained from Hall bar measurements. First the 4 terminal resistance is measured and a minimum sheet resistance of 530 $\frac{\Omega}{\text{sq}}$ is extracted. In combination with the 2 terminal resistance determined previously, the resistance per ohmic contact is estimated to be 4.3 kΩ. An improvement in sheet resistance and contact resistance would be desirable in particular for transport measurements. However, advanced experiments on qubit devices are mostly performed using charge sensing techniques. By measuring the classical and the quantum Hall effect, the electron mobility and the corresponding density is extracted. From the data at low electron densities the percolation density is estimated to be around $1\times10^{12}\,\text{cm}^{-2}$. A peak mobility of $(2350 \pm 20)\,\text{cm}^2/\text{Vs}$ is reached at a density of $(3.48 \pm 0.05)\times10^{12}\,\text{cm}^{-2}$ resulting in a maximum mean free path of 72 nm. The Fermi wavelength at the percolation density is about 25 nm and 13 nm at the electron density of maximum mobility. For larger densities the mobility is reduced despite the increase in electron density. The electrons start to feel the surface roughness, which effectively acts as scattering centers reducing the mobility. In addition, the relation between the electron density and the gate voltage gives access to the gate capacitance of $0.46\,\mu\text{F}/\text{cm}^2$ close to the geometric capacitance.
The conductance plateaus of the quantum Hall effect determine the number of filled Landau levels in the range between 28 and 40. A quantum lifetime 0.15 ps corresponding to a Landau level broadening of 2.1 meV is extracted from a fit to the envelop of the SdH oscillations. The large broadening explains why neither the spin nor the valley splitting is resolved. For higher magnetic fields and improved mobilities the quantum Hall effect allows to determine the spin and valley splitting in contrast to the classical Hall effect.
In order to put these results in perspective, they are compared to Ref. [Sab19] in table 4.1. In the work of Sabbagh et al. the percolation density is an order of magnitude lower than in

Table 4.1: Comparison to the Literature

Ref.	T (K)	t_{SiO_2} (nm)	$t_{Al_2O_3}$ (nm)	n_p ($1/\text{cm}^2$)	μ_{max} (cm^2/Vs)	n_{max} ($1/\text{cm}^2$)	l (nm)	Γ (μeV)
This work	0.4	5	3	1×10^{12}	2350	3.48×10^{12}	72	2100
[Sab19]	1.7	10	17	1.75×10^{11}	9800	1.13×10^{12}	120	480

this work, while the maximum mobility is about 4 times larger than in this work. Also the mean free path and the Landau level broadening is smaller despite the temperature being

lower in this work. There are two major reasons for the differences. First, the mobility typically improves with thicker oxides. The equivalent oxide thickness is 6.3 nm in this work, while it is 17 nm in Ref. [Sab19]. In Ref. [Pud02] a record mobility of 34000 cm^2/Vs for a Si/SiO_2 substrate is reported for a SiO_2 thickness of 190 nm. The thicker oxide mitigates the effect of the granularity of the gates and the strain caused by the gates. The trade-off here is that a thicker oxide also reduces the gate lever arm. Second, there is the material and process quality which affects the mobility as any impurity in the oxide or at the interface acts as a scattering center.
For the future an improvement in percolation density as well as mobility would be desirable. From the improved charge stability of quantum dots measured on a new wafer and on complete industrial devices, improvements regarding Hall bar measurements can be expected. In addition, Hall bars made by the industrial process would give more insights for the final devices.
Quantum dots fabricated on the same chip as the Hall bars reveal defects relevant at very low electron densities and close to the quantum dot. They become visible in the form of two level fluctuations and switches in the stability diagram. In addition, quantum dots are formed under each gate and not only at the intended position. On a different wafer from a new batch the charge stability is greatly improved, but the quantum dots are again not formed at the intended position. Coulomb diamonds reveal a variety of excited states and impurities. This shows that despite improvements on the new wafer, the fabrication process is critical. Further confinement of the electrons could lead to better quantum dot formation. The Fermi wavelengths extracted previously from the Hall bar measurements are rather small and it is challenging to shrink the device dimensions further. Therefore, the material quality in particular the percolation density and maximum mobility need to be improved further for reliable quantum dot operation.
However, this thesis continues in the next chapter with industrially fabricated devices using a micro-magnet added in post-CMOS processing. They are based on the same type of FD-SOI wafer as the substrate and demonstrate that the industrial fabrication process at CEA-Leti results indeed in better charge stability. With the help of the added micro-magnet qubit operation will be demonstrated in the following chapter.

CHAPTER 5

Electron spin qubit

5.1 Introduction

Semiconductor spin qubits are among the leading platforms for building an universal quantum computer. Many building blocks have been successfully implemented in academic devices. They show long coherence times [Muh14] and allow for fast manipulation [Yon18] which results in high single and two qubit fidelities [Mad22; Noi22; Xue22].
In order to leverage these successes for building larger and larger demonstrators of a quantum computer, the technologies used need to be adapted to be more reliable and scalable. For semiconductor spin qubits, CMOS technology is the ideal candidate for this purpose. The same way billions of transistors are integrated in a classical processor, a large number of quantum dots could be integrated leading to a quantum computer that has a sufficient number of qubits to solve useful problems [Van13]. However, making the direct leap from academic fabrication to qubits fabricated fully by industrial CMOS standards is too large to be done without intermediate solutions.
An important step is to process all the parts of the qubit that are compatible with CMOS technology on an industrial level and only add the components that are incompatible with CMOS technology by post-processing in an academic clean room. Previously, the design and fabrication of hybrid academic/industrial silicon spin qubit devices was shown. The main addition to the industrial device in post-processing is a FeCo micro-magnet that enables efficient driving of the electron spin via EDSR. Thereby, the performance of the industrial device can be investigated beyond the existing work on charge control and spin readout [Ans20; Cha20; Cir21; Gil20; Nie22; Spe22; Urd19]. Alternative approaches to drive the spin are the use of a stripline for ESR, as well as the manipulation of the spin via the intrinsic spin-orbit coupling. A stripline can be integrated in the industrial process, however manipulation speeds are limited [Zha18]. Manipulation via the intrinsic spin-orbit coupling is a viable option for hole spin qubits [Mau16; Pio22], however for electron spin qubits in silicon the small intrinsic spin-orbit coupling is does not allow for efficient spin driving [Cor18].
Academic devices for electron spin qubit devices featuring a micro-magnet have demonstrated high qubit fidelities due to the ability to engineer the extrinsic spin orbit coupling and therefore optimize the qubit drive as well as the decoherence originating from charge noise [Mil22; Noi22; Xue22; Yon18].
On purely industrial devices, based on CMOS technology qubit control has been demonstrated using a stripline and the ESR technique [Zwe22]. In this thesis, the advantages of a micro-magnet fabricated in an academic clean room are combined with an industrially

fabricated device with great prospect in scalability. The resulting devices serve as a testbed to demonstrate spin manipulation via EDSR. In addition, this method can provide valuable feedback to the fabrication on aspects that are not accessible within a reasonable time frame otherwise. The device under test for this chapter corresponds to the device depicted in Fig. 5.1. The nomenclature for the different parts of the device is adopted from the same figure. All measurements are carried out at the dilution cryostat base temperature of 120 mK.
In the following chapter, the characteristics of one of the afore mentioned devices is studied in detail. First, the design is introduced in Sec. 5.2. Quantum dot measurements are presented in section 5.3, followed by spin measurements in section 5.4 and spin manipulation via EDSR is demonstrated in section 5.5.

5.2 Device design

In this section the design of the hybrid industrial/academic qubit device is explained, while the fabrication has been detailed in section 3.2. First, an industrial device is chosen as a basis and its functionality is explained. Then, the design constrains on the gates contacting the device are discussed. Finally, the design and the magnetic properties of the micro-magnet are presented.
The basis of the hybrid industrial/academic qubit is an industrially fabricated quantum dot device. The channel is formed by an 80 nm wide silicon nanowire using CEA-Leti based FD-SOI technology. A device with a single pair of split gates, having a gate length L_G, as well as a gate separation S_V of 50 nm is chosen, because it is the simplest device where capacitive charge sensing via a SET and energy selective spin readout has been demonstrated before.
A large quantum dot used as a SET is formed under gate T_1. A small quantum dot, which serves as the qubit is formed under gate B_1. The situation is illustrated in Fig. 5.1. There is no gate directly controlling the coupling between the quantum dots nor their coupling to the reservoirs. Therefore, alternative methods need to be used, to bring the two quantum dots in the desired coupling regime. For the SET, the coupling to the reservoirs needs to been strong enough to allow for a detectable current flow through the device. Between the two quantum dots only capacitive coupling for charge detection is desired. The qubit dot needs to have a small tunnel coupling to the reservoirs with a tunnel rate faster than the spin relaxation rate. On the other hand the acquisition time sets a limit how for the maximum tunnel rate that can be resolved.
In a first step, the channel width, as well as the gate length and separation need to be chosen so that the couplings are roughly in the right regime by design. The coupling of the SET to the reservoirs and the qubit dot can be tuned by changing the charge occupancy in the SET. Thereby, the size of the corresponding quantum dot changes and with it the overlap of wave functions. Hence, the coupling increases for more electrons in the sensor. Finally, the coupling can be controlled by the micro-magnet which acts as a top gate, as well as the back gate. However, the coupling between the quantum dots and their coupling to the reservoirs are changed simultaneously. These three methods combined allow for capacitive charge sensing, as well as energy selective spin readout in this device and it has been demonstrated previously on two devices with similar dimensions [Spe22].

Devices with wrap-around gates would need to me measured either in a transport measurement [Cor18] or by RF reflectometry [Urd19]. In transport measurements the last electron is difficult to reach and spin fidelities are typically low. Therefore, relying on transport measurements is not suitable for coherent spin manipulations. Using source or gate refelectometry is a potential route to improve the speed and fidelity of spin readout in the future. However, it comes with additional requirements for the experimental setup. For this work, the focus is on a first demonstration of coherent electron spin manipulation and post-processing on a FD-SOI device.
The devices are contacted with Ti/Al gates. Their layer stack is mostly motivated by the fabrication. The material should not be superconducting or at least the superconductivity needs to beak down during the measurement. The measurements are performed typically at an external magnetic field of 0.5 T, which is much larger than the critical magnetic field of aluminum. Hence, aluminum can be used as gate metal. If the gates would remain superconducting, the Meissner effect would lead to an expulsion of the magnetic field weakening and distorting the field created by the micro-magnet.
The design of the gates leading to the bond pads is shown in 5.1 c). The gates increase in size the further they are away from the devices until they are connected to bond pads. The gate B_1 is connected to a triangular aluminum gate. The tapered gate is designed to avoid abrupt changes in the gate size and therefore its impedance. The final part of the triangular gate that is intended as a bond pad is twice as large as a regular bond pad to accommodate two bond wires. In addition, two ground planes are added next to the triangular gate forming a coplanar wave guide. These choices were made for optimal transmission of the RF signal.
The last layer added in post-processing is a FeCo micro-magnet. Its purpose is to provide a magnetic field gradient for efficient spin driving via EDSR. The magnet is composed of three rectangles of size 4.5 µm by 1.5 µm connected to a gate that leads to a bondpad. Besides providing a magnetic field gradient, the micro-magnet is used as a top gate. By applying a voltage on the micro-magnet, the coupling between the quantum dots and to the reservoirs can be tuned slightly. The potential below the gates however is mostly unaffected as the metallic gates screen the influence of a top gate.
The coordinate system is defined as in Fig. 5.1 a) with the external magnetic field oriented along the z-axis, the easy axis of the micro-magnet. The y-axis is pointing down, out of plane and the x-axis is oriented along the nanowire. Each rectangle can be seen as a separate magnet. The shape of each magnet is chosen to be long along the direction of the external magnetic field so that magnetic domains will orient along this axis [Neu15].
The gap between the two magnets is 450 nm and the quantum dot is displaced from the center of the gap by about 23 nm in x and -15 nm in z. These values vary slightly from the intended values and are therefore extracted from the SEM image. The thickness of the FeCo magnet is 300 nm. Taking into account the gate stack, the SiO_2 layer gates, isolation and the adhesion layer the micro-magnet is estimated to be 212.5 nm away from the 2DEG. In the framework of the master thesis of Victor El Homsy these parameters were used to simulate the magnetic field of the micro-magnet. The contribution of each magnet is calculated analytically and added up to obtain the stray field of the micro-magnet (Eqn. 5.1). The gradient matrix (Eqn. 5.3) is calculated numerically by differentiating the stray

field. The stray field in the z-direction is adjusted to the value of 167 mT that is found by analyzing the magnetic field dependence of the Larmor frequency in section 5.5.1. The other values of the stray field and the gradient matrix are scaled accordingly to obtain the correct absolute values for a partially magnetized magnet. The micro-magnet adds a small contribution to the magnetic field in x and y of $B_x = 0.14\,\mathrm{mT}$ and $B_y = -11\,\mathrm{mT}$. Compared to the magnetic field along the z-direction, consisting of the micro-magnet contribution $B_z = 161\,\mathrm{mT}$ and the external magnetic field $B_{ext} \approx 0.5\,\mathrm{mT}$, the in-plane contributions only slightly tilt the quantization axis.

$$B = \begin{pmatrix} B_x \\ B_y \\ B_z \end{pmatrix} = \begin{pmatrix} 0.15 \\ -11 \\ 167 \end{pmatrix} \mathrm{mT} \tag{5.1}$$

The gradient matrix G contains the local variation of the magnetic field in the directions B_x, B_y, B_z for displacements of the electron in the x, y, z direction. The intended displacement is in the z-direction. However, due to the formation of the quantum dot in the corner of the nanowire, a small displacement in the y-direction is expected, as well [Voi14]. The displacement in the x-direction is negligible. Biel Martinez Diaz and Yann-Michel Niquet from CEA IRIG have simulated the response of an electron to an AC voltage V_{AC} applied to the gate in a similar device [Mar22]. This polarizability $\overrightarrow{r'}$ is estimated to be 0.1 nm/mV for the z-direction resulting in a Rabi frequency $f_R = 1.14\,\mathrm{MHz}$ using formula 5.2 and V_{AC} = 1 mV. The g-factor is assumed to be 2, $\overrightarrow{b}$ is the unit vector pointing along in the same direction as the magnetic field, μ_B is the Bohr magneton and h Planck's constant.

$$f_R = \frac{V_{AC}\mu_B g}{2h} |\overrightarrow{b} \times G\overrightarrow{r'}| = \frac{V_{AC}\mu_B g}{2h} |\frac{dB_y}{dz} z'| \tag{5.2}$$

The resulting gradients for the field oriented along the, x-axis as well as for displacements along the x-axis, the effect of the micro-magnet is negligible. The gradient of the magnetic field in the y-direction for a movement of the electron in the z-direction is $\frac{dB_y}{dz} = 0.81\,\mathrm{mT/nm}$. It is responsible together with the much smaller $\frac{dB_x}{dz} = 0.011\,\mathrm{mT/nm}$ gradient for driving the spin around the Bloch sphere. These gradients are commonly referred to as the transverse gradient. The gradients for the magnetic field oriented in the z-direction, cause the electron spin to pick up a phase. They are commonly referred to as the longitudinal gradient. The $\frac{dB_z}{dx}$ component is small and the displacement is negligible. By design, the $\frac{dB_z}{dy}$ = -0.89 mT/nm component is similar in strength compared transverse gradient. However, for devices typically found in the literature [Yon18] the displacement along the y-direction is negligible. In the present device, the a significant displacement in the y-direction is expected and therefore an additional dephasing is expected as well. The $\frac{dB_z}{dz}$ = -0.055 mT/nm component is designed to be small compared to the transverse gradient, as it causes a dephasing proportional to the driving.

$$G = \begin{pmatrix} \frac{dB_x}{dx} & \frac{dB_x}{dy} & \frac{dB_x}{dz} \\ \frac{dB_y}{dx} & \frac{dB_y}{dy} & \frac{dB_y}{dz} \\ \frac{dB_z}{dx} & \frac{dB_z}{dy} & \frac{dB_z}{dz} \end{pmatrix} = \begin{pmatrix} -2.18 \times 10^{-3} & -0.14 \times 10^{-3} & 0.011 \\ -0.13 \times 10^{-3} & 0.063 & -0.81 \\ 0.011 & -0.89 & -0.055 \end{pmatrix} \text{mT/nm} \quad (5.3)$$

The third magnet above connects the two other magnets to keep their electric potential identical. However, it also generates a difference in magnetic field ΔB_z between neighboring quantum dots along the nanowire. This allows addressing two or more qubits independently in a future device.

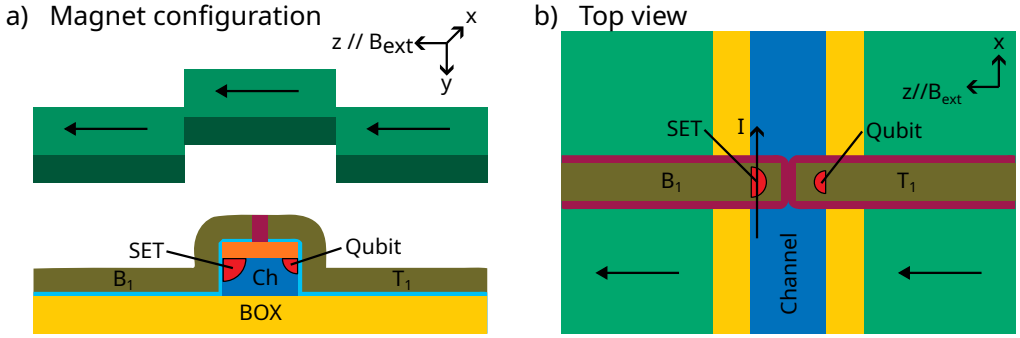

Figure 5.1: Device design a) Magnet configuration relative to the device. The device (bottom) is cut through the gates in the y,z-plane. The gates (olive green) are split and wrapped around the nanowire that forms the channel Ch (blue). In the left corner a large quantum dot which serves as a SET for charge sensing is formed. A small quantum dot in the right corner serves as the qubit. 212.5 nm above the device the micro-magnet (green) is placed with its easy-axis oriented along the z-axis, parallel to the external magnetic field. **b)** Top view of the device. A small current for charge sensing flows through the SET quantum dot. The qubit quantum dot is capacitively coupled to the SET and tunnel coupled to the reservoirs formed in the channel.

5.3 Quantum dot measurements

The first step to characterize a semiconductor electron spin qubit is to form quantum dots and monitor their charge occupancy down to the last electron. This task is well described in the literature [Wie02; Zwa13] and is now routinely achieved in industrial devices fabricated by CEA-Leti [Cha20; Nie22; Spe23; Spe22; Urd19].
A bias voltage of 0.6 mV is applied between the source contact and the drain contact. Voltages are set on the gates T_1 and B_1 in order to enable conduction through the channel. The resulting current is measured using the setup described in Ch. 3. In the stability diagrams the X(Y)-axis represent the voltages applied to the gates T_1(B_1) and the color scale shows the current flowing through the device. The concept behind a stability diagram is introduced in Ch. 2.

5.3.1 Charge stability

In order to get an overview, a stability diagram covering the different regimes of conductance is recorded. It ranges from no conductance at all over Coulomb blockaded conduction to transistor like behavior. The resulting global stability diagram is shown in Fig. 5.2 a). In the bottom left corner no conduction is possible as the voltage applied to both gates is pinching off the current through the channel entirely. On the top left (bottom right) lines of conduction almost orthogonal to the B_1-axis (T_1-axis) are visible indicating Coulomb blockaded current flow through the quantum dot formed below the gate B_1 (T_1). In the top right corner current can flow through both sides of the channel resulting into more transistor like behavior with incomplete Coulomb blockade. Towards the center of the stability diagram a broad transition angled 45 ° with respect to the B_1-axis and T_1-axis is visible. This indicates an equal coupling to both gates. The transition is attributed to a dopant that entered the channel either during implantation or due to diffusion during one of the annealing steps.
When zooming into the middle right part of the global stability diagram, the transitions of the quantum dot below T_1 are clearly visible, as shown in Fig. 5.2 b). As the quantum dot below T_1 can serve as a charge sensor for the quantum dot on the other side, it is from now on referred to as the sensor dot. The sensor dot is operated in the many electron regime to ensure a detectable current flow. In the order of 100 electrons are loaded into the sensor dot. However, the exact occupation can not be determined as the dopant transition is crossing and shifting the sensor transitions at lower occupation multiple times. The voltage difference between neighboring sensor dot transitions is extracted in an undisturbed area. The occupation is estimated by extrapolating to the sensor voltage used for the measurements. The sensor transitions undergo a shift towards more positive voltages on T_1, when an electron enters the quantum dot below the gate B_1. The quantum dot below B_1 is from now on referred to as the qubit dot, as it will be used to form a qubit in this chapter. Due to the capacitive effect of the charge in the qubit dot a more positive voltage is necessary to align the chemical potential of the sensor dot with the bias window. Therefore, the current flowing through the sensor dot can be used to detect the charge occupation of the qubit dot. With this technique the charge occupation of the qubit dot can be monitored down to the last electron. In Fig. 5.2 b) the white dashed lines highlight the first two transitions of the qubit dot and the electron number is indicated. No further transition occurs below the one at $B_1 = 0.58\,\mathrm{V}$.
Fig. 5.2 c) shows the stability diagram, when zooming in again on the first transition of the qubit dot and focusing on the strongest sensor transition. The two branches of the sensor transition are clearly separated due to the capacitive shift induced by an electron entering or leaving the qubit dot. Stochastic tunneling events become visible when crossing the qubit dot transition, indicating that the tunnel rate is in the same range as the acquisition time.

5.3.2 Gate lever arm and electron temperature

In Fig. 5.2 d) so called Coulomb diamonds are shown. On the x-axis the voltage applied to gate T_1 is varied as in Fig. 5.2 b). The position in the stability diagram where the Coulomb diamonds are measured is indicated by the horizontal red dashed line. On the y-axis, the

bias voltage is swept from -8 mV to 8 mV. By identifying the corners of a diamond the gate lever arm can be extracted. The clearest diamond, highlighted by orange lines, is used to determine the gate lever arm of 0.28 eV/V. However, the value depends highly on the limits of the color scale making the diamond taller or shorter. For the extraction, the limits were chosen to be significantly larger than the noise floor, but also smaller then the height of a Coulomb peak in the low bias regime as shown in Fig. 5.2 c). Furthermore, the lever arm is expected to increase for lower electron occupations. Therefore, the extracted gate lever arm can only be an estimation of the actual lever arm relevant for the qubit dot and for the extraction of the electron temperature in the next step.
Fig. 5.2 e) shows a cut orthogonal to the qubit dot transition. The measurement is taken with an acquisition time per point much longer then the tunneling rate. Therefore, no stochasticity is present in this measurement. As the tunneling rates of the qubit dot towards the reservoirs, as well as to the sensor dot are small compared to the acquisition rate, the remaining effect to broaden the transition is the temperature. A Fermi–Dirac distribution as described in Eqn. 5.4 is fitted to the data.

$$I = I_0 \frac{I_1}{1 + e^{\frac{\alpha_G (s - s_0)}{k_B T}}} \tag{5.4}$$

Assuming the gate lever arm obtained from Fig. 5.2 d) the electron temperature is estimated to be 400 mK. This value is significantly larger than the base temperature of the cryostat of 120 mK. One reason for that can be the uncertainty on the gate lever arm discussed previously. Another possible explanation for the discrepancy could be that the thermometer to measure the base temperature is mounted on the mixing chamber of the cryostat and not on the cold finger where the device is mounted. In addition, insufficient thermalization and filtering as discussed in 3.4 might increase the electron temperature. However, the temperature is sufficiently low in order to readout and manipulate the spin, described in the next sections.

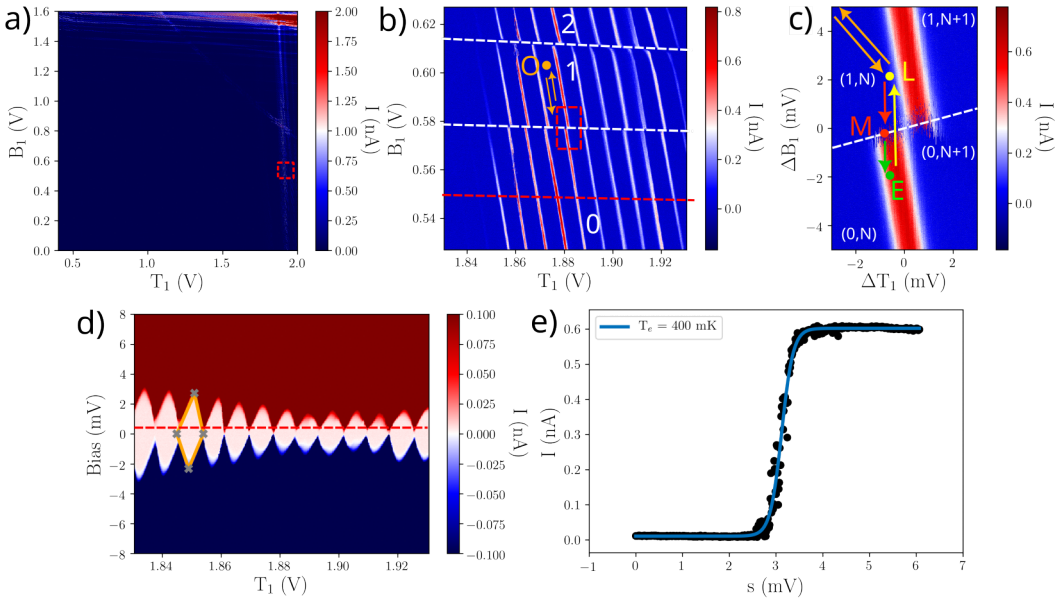

Figure 5.2: Charge characterization a) Global stability diagram. The X(Y)-axis represent the voltages applied to the gates T_1(B_1) and the color scale shows the current flowing through the device. The red square highlights the region shown in b). **b)** Zoom into the region relevant for spin measurement and manipulation. The quantum dot formed under gate B_1 is in the few electron regime. The electron occupancy is indicated and the white dashed lines emphasize a charge transition in this quantum dot. The quantum dot formed under the gate T_1 is in the many electron regime and is used as a charge sensor. The orange circle indicates the operating point O for spin manipulation. The red rectangle highlights the region shown in c). **c)** Zoom on the transition used for spin measurement. The empty position E (green), load position L (yellow) and measurement position M (red) are indicated by circles in the respective color. **d)** Coulomb diamonds measured along the red dashed line visible at the bottom of b). The diamond highlighted by the orange lines is used to determine the gate lever arm α_G = 0.28 eV/V. **e)** Current measurement across the transition depicted in c) with s defined as $s = \sqrt{T_1^2 + B_1^2}$. A Fermi–Dirac distribution assuming α_G extracted from d) is fitted to the data resulting in an electron temperature of 400 mK. All measurements were performed at the cryostat base temperature of ≈ 120 mK.

5.4 Spin measurements

With the charge under control, the next step is to readout the spin configuration. On this device energy selective spin readout [Elz04] was chosen among the different techniques to readout the spin state of quantum dots descried in 2.6. Energy selective spin readout is a well established tool that does not necessarily give the highest possible readout fidelities, but is relatively easy to implement. The first requirement is a charge sensor. Second, tunnel coupling of the qubit dot to one reservoir or the sensor dot with a tunnel rate much faster than the spin relaxation rate, but slower than the acquisition time is needed. Finally, the temperature needs to be in the same range or lower than the Zeeman energy [Ama08]. As these conditions are fulfilled and the focus for this thesis is on spin manipulation, energy selective spin readout is the best choice for spin readout. In addition, this readout

technique has been established on two previous devices [Spe23]. Therefore, the optimal device dimensions are known plus the hardware and software necessary is established.
In this section, the measurement procedure is described first and then the spin relaxation is discussed. In the latter part, the spin relaxation time T_1 is studied for different magnetic fields and the role of spin-orbit coupling as well as spin-valley coupling is studied.

5.4.1 Measurement procedure

The theory behind energy selective spin readout has been laid out in section 2.6. Here, the practical realization is discussed. The positions in the stability diagram corresponding to the different steps in the protocol are depicted in Fig. 5.2 c). The first step is to move to the region where no electrons are in the qubit dot in order to empty it (position E). After a waiting time longer the than the tunnel rate, the electron is moved quickly along the yellow arrow to the loading position L. The loading position is located far enough from the transition so that both the energy level of the spin down, as well as spin up are well below the Fermi energy. An electron with random spin orientation is loaded during the loading time t_{load}. Subsequently, the electron is moved along the red arrow to the measurement position M. At the measurement position the energy level of a spin up electron is located above the Fermi energy, while the energy level of a spin down electron is below. Once the measurement position is reached, the data acquisition is started. A click in the sensor current is recorded when a spin up electron tunnels out of the qubit dot until a spin down electron from the reservoir tunnels back into the qubit dot. Hence a spin to charge conversion is achieved and the result can be detected in the current flowing through sensor dot. Example time traces are shown in Fig. 5.3 a). The blue line shows the detection of a spin up electron and the red line the detection of a spin down electron. In the case of a spin down electron initially loaded into the qubit dot, its energy is below the Fermi energy of the reservoirs. Therefore, it is blocked from tunneling out of the quantum dot and no change in the sensor current appears. After the measurement, the qubit dot is emptied again by moving the electron along the green arrow back to the empty position E.
In a first step the procedure described above is repeated for different measurement positions starting from the quantum dot being empty to one electron being loaded into the quantum dot. In between these two cases, the chemical potential of the spin up electron lies above the Fermi energy and the chemical potential of the spin down electron below. In this region spin readout is possible and it is defined as the measurement window. If a spin up electron is measured, the quantum dot is emptied first and reloaded once leading to a single click. In the light blue area labeled meas visible in Fig. 5.4 a) either a single click or no click is recorded. It is therefore possible to distinguish between a spin up and a spin down electron in the measurement window.
By extracting the size of the measurement window for different magnetic fields, the gate lever arm α_G can be extracted. A line, as defined in Eqn. 5.5 is fitted to the last four points at high magnetic field.

$$V_{MW} = \frac{2\mu_B}{\alpha_G} B + b \tag{5.5}$$

V_{MW} is the size of the measurement window in volts, μ_B is Bohrs magneton, B is the magnetic field and b is an offset. A gate lever arm of 0.62 eV/V is extracted from the slope.

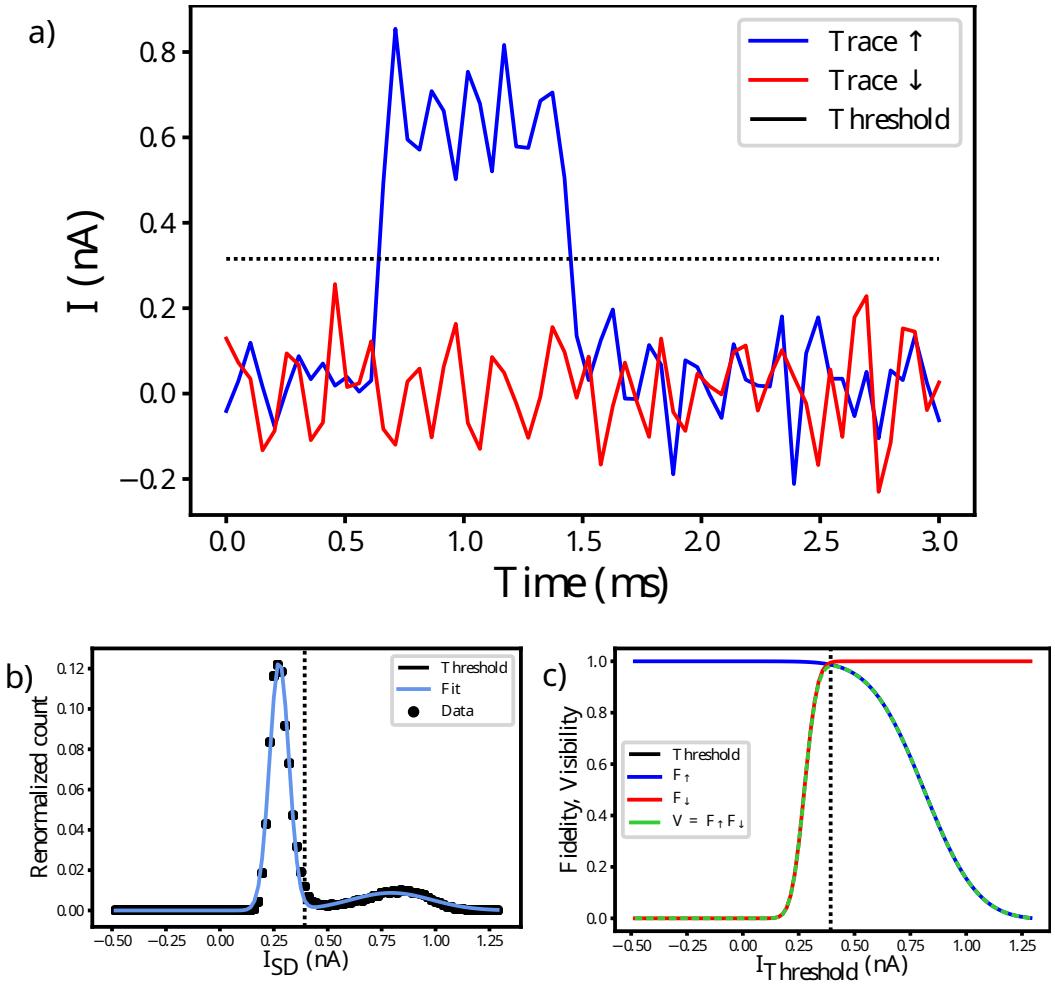

Figure 5.3: Fidelity analysis a) Single shot traces for a spin up electron (blue) and a spin down electron (red). The threshold is optimized to discriminate between spin up and spin down is depicted by the dashed line. **b)** Histogram of the maximal values from all traces of the experiment in d). A double Gaussian with a decay is fitted to the data. **c)** Based on the fit in b) the fidelity of the spin up and down measurement, as well as the visibility is calculated. The threshold is set to the point of maximum visibility.

The reason why the first points are not taken into account is that size of the measurement window becomes so small that it is difficult determine the exact borders and it becomes sensitive to charge fluctuations of the transition. For larger magnetic fields the relative error from this effect becomes small and the values can be used to determine the measurement window.

Following the calculation from Sec. 5.3.2 a gate lever arm of 0.62 eV/V suggests that the electron temperature is 886 mK instead of 400 mK. However, such elevated electron temperatures are inconsistent with the fact that energy selective spin readout is possible at magnetic fields as low as 0.44 T. The Zeeman energy ($E_Z = 51\,\mu$eV) would be significantly

smaller than the thermal energy ($E_T = 76\,\mu eV$) in this case.
This method represents a different way to measure the gate lever arm with the advantage that it probes the qubit dot directly in the single electron regime. In contrast, for the gate lever arm extracted from Coulomb diamonds (see Sec. 5.3.2) the sensor dot is probed in the many electron regime.
An additional method to extract the gate lever arm consists of calibrating the electron temperature with different bath temperatures. However, changing the temperature using a heater in the fridge is very limited, as the heater is far from the device. Changing and measuring the temperature at the PCB, close to the sample, is not possible with the setup. Even though the method presented here seems more suitable to determine the gate lever arm, the resulting electron temperature stands contrast to the spin measurements at low magnetic fields. Therefore, no final conclusion can be made on the gate lever arm.

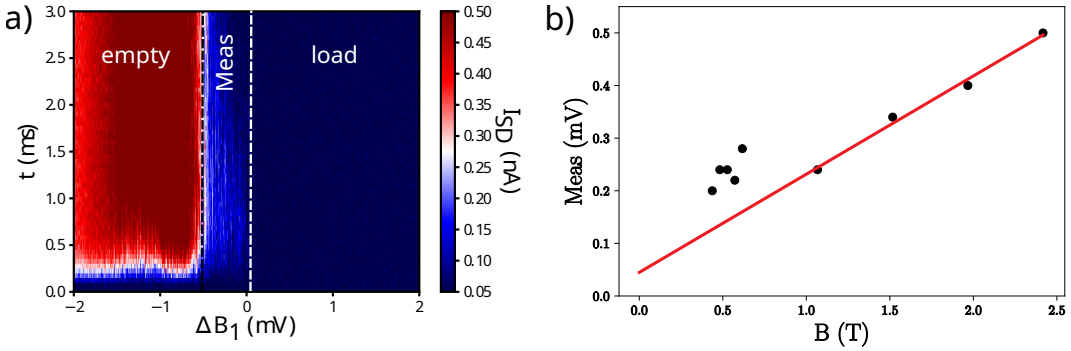

Figure 5.4: Measurement window a) Single shot time traces are plotted for different measurement positions at a magnetic field of 2.46 T. On the y-axis the measurement time t is plotted and the x-axis the voltage ΔB_1 is varied. The sensor current I_{SD} is plotted in color code. The measurement position is changed over the transition from an empty quantum dot to one electron loaded into the quantum dot. In between the quantum dot is emptied and reloaded once, defining the measurement window (Meas). **b)** The size of the measurement window (Meas) is plotted for different magnetic fields B. A line is fitted to the last four points suggesting a gate lever arm of 0.62 eV/V.

The single shot time traces are recorded with an integration time of 50 µs per point and a typical trace is 3 ms long. By recording many repetitions of the single shot traces an optimal threshold for discriminating between a click and no click can be found. For each trace the maximum current is plotted in a histogram. In Fig. 5.3 b) two peaks become visible one centered around 0.25 nA representing the case when the current remains at the base level. A second smaller peak at 0.8 nA represents the case when a click is recorded. The histogram is fitted with two Gaussians and a decay term taking into account the spin relaxation during the measurement. From the fit, the fidelity as well as the visibility of the measurement depending on the threshold current can be derived. The optimal threshold is found at the maximum visibility as shown in 5.3 c). In this example a click is detected with a fidelity of $F_c = 0.987$ and no click is detected with a fidelity of $F_{nc} = 0.995$. A visibility of $V = F_c F_{nc} = 0.982$ is achieved.
A complete fidelity analysis involving a numerical simulation of the experiment as in Ref.

[Kei19; Mor10] is omitted. The reason is that for low magnetic fields, where most of the following measurement are performed, the measurement window is so far degraded that correct modeling of the data becomes difficult. In that case, only an estimation for the threshold is extracted from the fit for single shot analysis.
In the ideal case, the current remaining at the base level corresponds to the detection of a spin down electron and a click to the detection of a spin up electron. However, state preparation and measurement (SPAM) errors such as thermal excitations, spin relaxation and loading/initialization errors lower the actual fidelity of the spin readout. These values therefore represent only the fidelity to correctly detect a click or not. The spin fidelity is characterized in the next subsection with the help of spin relaxation.

5.4.2 Spin relaxation

Using the threshold found previously, the population can be calculated. It corresponds to the fraction of click events from repeated time traces. In the first experiment the loading time is varied. Once a spin up electron is loaded, the spin orientation remains up on average for the spin relaxation time T_1. The data points for waiting times up to 30 ms at a magnetic field of 2.46 T are shown in Fig. 5.5 d). It is fitted to an exponential decay resulting in a spin relaxation time $T_1 = 5.2\,\mathrm{ms}$ in this example.
In the ideal case a population of 50 % is expected for very short loading times, as initially a random spin orientation should be loaded. However, the initial population in Fig. 5.5 d) is $P_I = 36\,\%$. This discrepancy gives an initialization error of 14 %. A possible explanation are discontinuities in the density of states of the reservoir prohibiting spin up electrons from being loaded [Pla13].
For long loading times the spin is expected to relax to the spin down state leading to a population of 0 %. In the experiment however, the final population P_F converges to a value of 9 %. Some electrons return to the spin up state even though the spin has relaxed. From the initial and the final the visibility of the spin measurement can be extracted using Eqn. 5.6. It gives a limited spin visibility of 78 %.

$$V = 1 - \frac{P_I + P_F}{2} \tag{5.6}$$

The thermal population of the spin up state can be estimated using formula 5.7 for the thermal occupation of a two level system following Fermi–Dirac statistics normalized by the initial population found earlier. For a magnetic field of 2.46 T corresponding to a Zeeman splitting of E_Z of 285 µeV and an electron temperature of 400 mK, Eqn. 5.7 gives a thermal population P_T of 0.03 %, which is in negligible compared to the 9 % in the measurement.

$$P_T = 2P_I \frac{1}{1 + e^{\left(\frac{E_Z}{k_B T}\right)}} \tag{5.7}$$

Hence for large magnetic fields thermal excitations or thermal broadening of the reservoir alone can not explain the discrepancy. The error might be related again to discontinuities in the density of states or falsely detected spin up events.
For smaller magnetic fields however thermal population of the spin can become as large

as 18 % for B = 0.44 T. While the fidelity to detect a click or not remains unaffected by the magnetic field, the spin fidelity is reduced for smaller magnetic fields. As the Zeeman energy is proportional to the magnetic field and the thermal broadening remains constant the window in which the measurement position can be chosen shrinks for smaller magnetic fields. The closer the measurement position is to the transition the more thermally activated errors will occur and the spin up electrons also get more prone to discontinuities in the density of states increasing the initialization error. Therefore, the spin fidelity will be degraded for smaller magnetic fields until no spin readout is possible anymore.
This requirement is the most critical one for energy selective spin readout to work with spin manipulation. If the spin readout can only be achieved at high magnetic fields the frequency to drive the qubit exceeds the capabilities of the RF setup. In previous devices, the lowest magnetic field that allowed energy selective spin readout was 1.5 T [Spe23]. This translates to a driving frequency of about 40 GHz for the qubit. Pioneering publications on Si/SiO_2 based spin qubits have worked with such high frequencies [Vel14], however these frequencies remain challenging to work with. In the present device, spin readout is possible down to a magnetic field of 0.44 T corresponding to a qubit frequency of only 12 GHz or $E_Z = 51\,\mu eV$. In comparison the electron temperature of 400 mK corresponds to a thermal energy of 34 µeV. Therefore, energy selective spin readout is compatible with spin manipulation in this device.

Magnetic field dependence of the spin relaxation rate

Next, the spin relaxation time is measured for different magnetic fields from 0.44 T to 2.46 T. In Fig. 5.5 e) on the y-axis the spin relaxation rate $1/T_1$ is plotted on a logarithmic scale and the magnetic field is plotted on the x-axis. A characteristic peak at 0.52 T is visible showing a drastically increased spin relaxation rate up to a relaxation rate of $T_1 = 320$ Hz. This peak can be attributed to the stronger spin valley coupling at the anti-crossing of the $|v_-, \uparrow\rangle$ state and the $|v_+, \downarrow\rangle$ state opening a channel for fast relaxation. It is called the spin-valley hotspot. At lower magnetic fields below the hotspot no spin readout is possible. Past the hotspot the relaxation rate passes a minimum of $T_1 = 2.4$ Hz at 0.62 T and increases afterwards for higher magnetic fields up to 190 Hz at 2.46 T.
In order to interpret this data, it is fitted using the model detailed in [Hua14; Spe22]. The fit model and its interpretation has been provided by Biel Martinez Diaz and Yann-Michel Niquet from CEA IRIG. The model consists of the contributions from spin-orbit coupling and spin-valley coupling taking Johnson–Nyquist noise, as well as phonon noise into account by adding up the rates of each contribution in Eqn. 5.8.

$$\frac{1}{T_1} = \Gamma_{SV,JN} + \Gamma_{SV,Ph} + \Gamma_{SO,JN} + \Gamma_{SO,Ph} \tag{5.8}$$

The spin-valley coupling is described by Eqns. 5.9 and 5.10 and corresponds to the orange curve. With $C_{i,j}$ (i ∈ {SV,SO}, j ∈ {JN,Ph}) being the respective coupling strength, E_Z the Zeeman energy, E_0 an arbitrary energy reference, k_b the Boltzmann constant and T

the temperature.

$$\Gamma_{SV,JN} = C^2_{SV,JN} \left(\frac{E_Z}{E_0}\right) \frac{\exp(\frac{E_Z}{k_b T}) + 1}{\exp(\frac{E_Z}{k_b T}) - 1} F\left(E_{VS}, \Delta_{SV}\right) \tag{5.9}$$

$$\Gamma_{SV,Ph} = C^2_{SV,Ph} \left(\frac{E_Z}{E_0}\right)^5 \frac{\exp(\frac{E_Z}{k_b T}) + 1}{\exp(\frac{E_Z}{k_b T}) - 1} F\left(E_{VS}, \Delta_{SV}\right) \tag{5.10}$$

F is a function of the valley splitting E_{VS} and the spin-valley gap Δ_{SV}. It is responsible for modeling the spin-valley hotspot and defined in Eqns. 5.11, 5.12, 5.13 and 5.14. E_{VS} gives the position of the hotspot on the x-axis and Δ_{SV} is responsible for the width of the peak. The spin-valley gap corresponds to the gap of the anti crossing of the $|v_-, \uparrow\rangle$ state and the $|v_+, \downarrow\rangle$ state.

$$F\left(E_{VS}, \Delta_{SV}\right) = \frac{2\Delta^2_{SV}(E_2 - E_1)}{(E_1^1 + \Delta^2_{SV})(E_1^2 + \Delta^2_{SV})} \qquad \text{if } E_{VS} \geq E_Z \tag{5.11}$$

$$F\left(E_{VS}, \Delta_{SV}\right) = \frac{2(E_1 E_2 + \Delta^2_{SV})^2}{(E_1^1 + \Delta^2_{SV})(E_1^2 + \Delta^2_{SV})} \qquad \text{if } E_{VS} < E_Z \tag{5.12}$$

$$E_1 = E_{VS} - E_Z + \sqrt{(E_{VS} - E_Z)^2 + \Delta^2_{SV}} \tag{5.13}$$

$$E_2 = E_{VS} + E_Z + \sqrt{(E_{VS} + E_Z)^2 + \Delta^2_{SV}} \tag{5.14}$$

As E_Z is proportional to the magnetic field, the global dependence of each rate is given by the exponent of $\left(\frac{E_Z}{E_0}\right)$. The Johnson–Nyquist noise contribution is linear while the phonon noise contribution scales with the power of five with B. However, outside of the hotspot the contribution of spin-valley coupling is negligible.
The spin-orbit coupling is described by Eqns. 5.15 and 5.16 and corresponds to the purple curve. It does not capture the hotspot, however the global dependence outside the hotspot fits very well. The Johnson–Nyquist noise contribution scales with the power of three while the phonon noise contribution scales with the power of seven.

$$\Gamma_{SO,JN} = C^2_{SO,JN} \left(\frac{E_Z}{E_0}\right)^3 \frac{\exp(\frac{E_Z}{k_b T}) + 1}{\exp(\frac{E_Z}{k_b T}) - 1} \tag{5.15}$$

$$\Gamma_{SO,Ph} = C^2_{SO,Ph} \left(\frac{E_Z}{E_0}\right)^7 \frac{\exp(\frac{E_Z}{k_b T}) + 1}{\exp(\frac{E_Z}{k_b T}) - 1} \tag{5.16}$$

The combination of both contributions (green) describes the data very well. An additional fit taking into account solely the phonon noise contribution (red), shows that it only becomes relevant for high magnetic fields, higher than the fields accessible in this experiment. Therefore, it can be concluded that the relaxation times are limited by Johnson–Nyquist noise. A previous device was phonon noise limited, however spin readout was only possible starting from 1.5 T and the hotspot occurred at 2.6 T [Spe22]. As the B^5/B^7 dependence

makes the phonon noise dominate at high magnetic fields, these findings are consistent with each other. In Ref. [Spe22] three devices, including this one, are compared. While the valley splitting differs, the overall magnetic field dependence of the relaxation rate is consistent for all three devices. This indicates that the global structure of the quantum dots is similar in both cases.
From the fit, a valley splitting of $E_{VS} = 60\,\mu\text{eV}$ or $0.52\,\text{T}$ is extracted. In order to put this number into context, it can be compared to the two other devices in [Spe22]. For them the valley splitting is significantly larger. A valley splitting of $300\,\mu\text{eV}$ ($191\,\mu\text{eV}$) is reported for device 1 (device 2). On similar devices using the same industrial fabrication technology even higher valley splittings of $681\,\mu\text{eV}$ and $571\,\mu\text{eV}$ are reported [Cir21]. Even though all these devices share the same technological basis for the qubit device, the device discussed here is unique due to the post-processing that was performed on it. Possible reasons for the degradation of the valley splitting due to post-processing are the additional exposure with ebeam lithography and the post-fabrication annealing that is different to the industrial process. However, wafer to wafer variations or local variations of the valley splitting are as well candidates to explain the different values of the valley splitting. Local variations are a known issue for the variability, as the valley splitting is sensitive to variation at the atomic scale [Paq22]. A systematic study of the valley splitting will be necessary to achieve the desired variability for scaling up to multi qubit systems and for mass production.
The spin-valley mixing strength $\Delta = 0.04\,\mu\text{eV}$ is smaller compared to the other two devices in Ref. [Spe22] of $4\,\mu\text{eV}$ for device 1 and $0.2\,\mu\text{eV}$ for device 2. This can be likely explained by destructive interference between the spin-valley coupling and the artificial spin-orbit coupling created by the micro-magnet.
Nevertheless, the region in magnetic field just past the spin-valley hotspot is interesting for qubit operation, as a minimum also called a cold spot can be exploited for long relaxation times [Hos21].

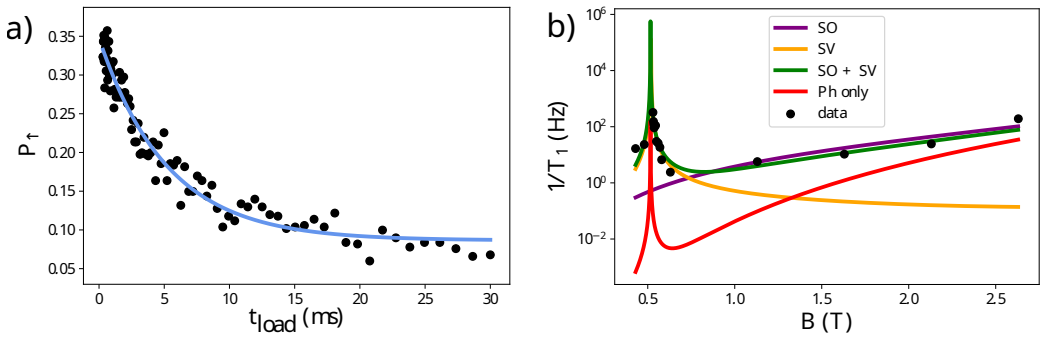

Figure 5.5: Spin relaxation a) Measurement of the spin relaxation time T_1 for an external magnetic field of 2.46 T. Using the threshold determined previously, the spin up population $P\uparrow$ is determined and plotted on the y-axis. On the x-axis the loading time t_{load} is varied to extract the spin relaxation rate. An exponential decay is fitted to the data yielding a spin relaxation time of $T_1 = 5.2\,\text{ms}$. **b)** Spin relaxation rate $\frac{1}{T_1}$ plotted for different magnetic fields B. At 0.52 T the spin relaxation hotspot is visible. The data is fitted to determine the contribution of spin-orbit coupling (purple) spin-valley coupling (orange). Both phonon noise, as well as Johnson–Nyquist noise are taken into account. The combination of spin-orbit and spin-valley coupling (green) fits the data best. A fit using only the phonon noise contribution is shown in red.

5.5 Spin manipulation

The spin measurement procedure can be modified to include spin manipulations. Starting from the empty position E in Fig. 5.2 c), the electron is moved to the measurement position. As the energy level of a spin down electron is below the Fermi energy, while the energy of a spin up electron is above the Fermi energy, a spin down electron is loaded into the quantum dot. Using this technique, the spin is initialized into the ground state for later manipulations. The possibility to initialize the spin to the ground state quickly, without relying on long spin relaxation times of up to 500 ms, is another advantage of using energy selective spin readout. The spin down electron is then moved to the loading position and subsequently moved to the operating position O in Fig. 5.2 b). At the operating position, the electron is in the middle between the $0 \rightarrow 1$ transition and the $1 \rightarrow 2$ transition of the qubit dot. Here, the spin manipulation can take place without the risk to cross a charge transition and therefore losing the intended charge and spin configuration. After the spin manipulation, the electron is returned to the loading position and the spin is measured as described previously in Sec. 5.4.

In order to drive the spin at the operating position, a microwave pulse is send to the gate B_1 using the microwave setup described in Ch. 3.4. At the microwave source the RF frequency and the input power of the carrier signal can be controlled. With pulses from the AWG the I and Q quadrature of the carrier frequency can be modulated using a mixer.

5.5.1 Larmor precession

In a first experiment involving spin manipulation the Larmor frequency is determined. In Fig. 5.6 a) the population is plotted against the excitation frequency f. Eqn. 1.10 from Ch. 1 for the spin up probability $P_\uparrow(f,t_p)$ depending on the excitation frequency f and the

pulse duration t_p can be rewritten in the form of Eqn. 5.17. With A being the visibility, f_L the Larmor frequency, f_R the Rabi frequency at resonance and B an offset accounting for thermal excitations.

$$P_{\uparrow}(f,t_p) = \frac{A}{\left(\frac{f-f_L}{f_R}\right)^2 + 1} \sin^2\left(\pi f_R t_p \sqrt{\left(\frac{f-f_L}{f_R}\right)^2 + 1}\right) + B \tag{5.17}$$

A central peak occurs where the resonance condition $f = f_L$ is fulfilled. Side peaks are visible, if the condition in Eqn. 5.18 is fulfilled with n being a positive integer. However, the first order side peaks are hidden in the central peak explaining the unusual shape compared to the literature [Pio22; Vel14]. The shape is a symptom of the low Rabi frequency and short coherence times measured in this device (see Sec. 5.5.2). The second order side peaks seem visible and fitted, but might as well originate from smoothing the data. Due to the degraded spin readout at low magnetic fields the spin-up population is smoothed with a moving average of 3 points to improve the convergence of the fits.

$$f = f_L \pm f_R \sqrt{\left(\frac{n-0.5}{f_R t_p}\right)^2 - 1} \tag{5.18}$$

On longer timescales the Larmor frequency is prone to fluctuations in the nuclear spin bath, drifts in the external magnetic field, as well as to charge noise via the micro-magnet. To account for these slow changes in the Larmor frequency, a feedback loop is implemented. The Larmor frequency is measured each minute and the newly determined Larmor frequency is used for the following main experiment. The feedback experiment takes about 20 s while the main experiment typically takes 40 s. The exact duration varies depending on the readout fidelity and the constrains of the main experiment. This procedure is repeated in order to obtain sufficient averages and all experiments are merged into a big experiment. A faster feedback or more advanced techniques to predict the correct Larmor frequency [Nak20] were not possible because of the low readout fidelity, as well as the long communication time between FPGA and computer. All of the following, more complex experiments are performed using a feedback loop.

Characterization of the micro-magnet stray field

In Fig. 5.6 b) the Larmor frequency is determined for different magnetic fields ramped up and down. A minor hysteresis loop becomes apparent indicated by the different slopes. The arrows indicate the direction in which the field is changed. To each dataset a line is fitted using Eqn. 5.19. The Larmor frequency f_L is composed of a contribution from the external magnetic field $B_{ext} = aB_{set}$ and the stray field of the micro-magnet B_μ. A correction factor a is introduced to compensate for the difference between the expected magnetic field and the set value of the magnetic field supply. μ_B is the Bohr magneton, h is Planck's constant and g is the electron g-factor. The g-factor is assumed to be 2 as only small deviations from the theoretical value are reported in the literature for electrons in

silicon [Feh59].

$$f_L = g\frac{\mu_B}{h}\left(aB_{set} + B_\mu\right) \tag{5.19}$$

The resulting correction factors are between 1.03 for the decreasing external magnetic field (blue points) and 0.92 or 0.90 for the increasing magnetic field (green or red points). When converting the data to the micro-magnet magnetization for a given correction factor, a minor hysteresis loop of the micro-magnet can be visualized. In order to obtain physical hysteresis, the smallest correction factor has to be taken into account. For an increasing external magnetic field the magnetization needs to remain constant or has to increase. Therefore, $a = 0.90$ is an upper bound for the correction factor. The discrepancy between the set value and the external magnetic field felt by the device can be probably explained by the home made cold finger of the cryostat not being aligned perfectly with the coils that produce the in-plane magnetic field.
For the magnetization of the micro-magnet $B_\mu = 167\,\mathrm{mT}$ is therefore a lower bound and $B_\mu = 247\,\mathrm{mT}$ is an upper bound obtained from micro-magnetic simulations for a fully polarized micro-magnet. As a hard magnet behavior is expected for FeCo at cryogenic temperatures, the choice of a constant magnetization and a large minor hysteresis loop is justified.

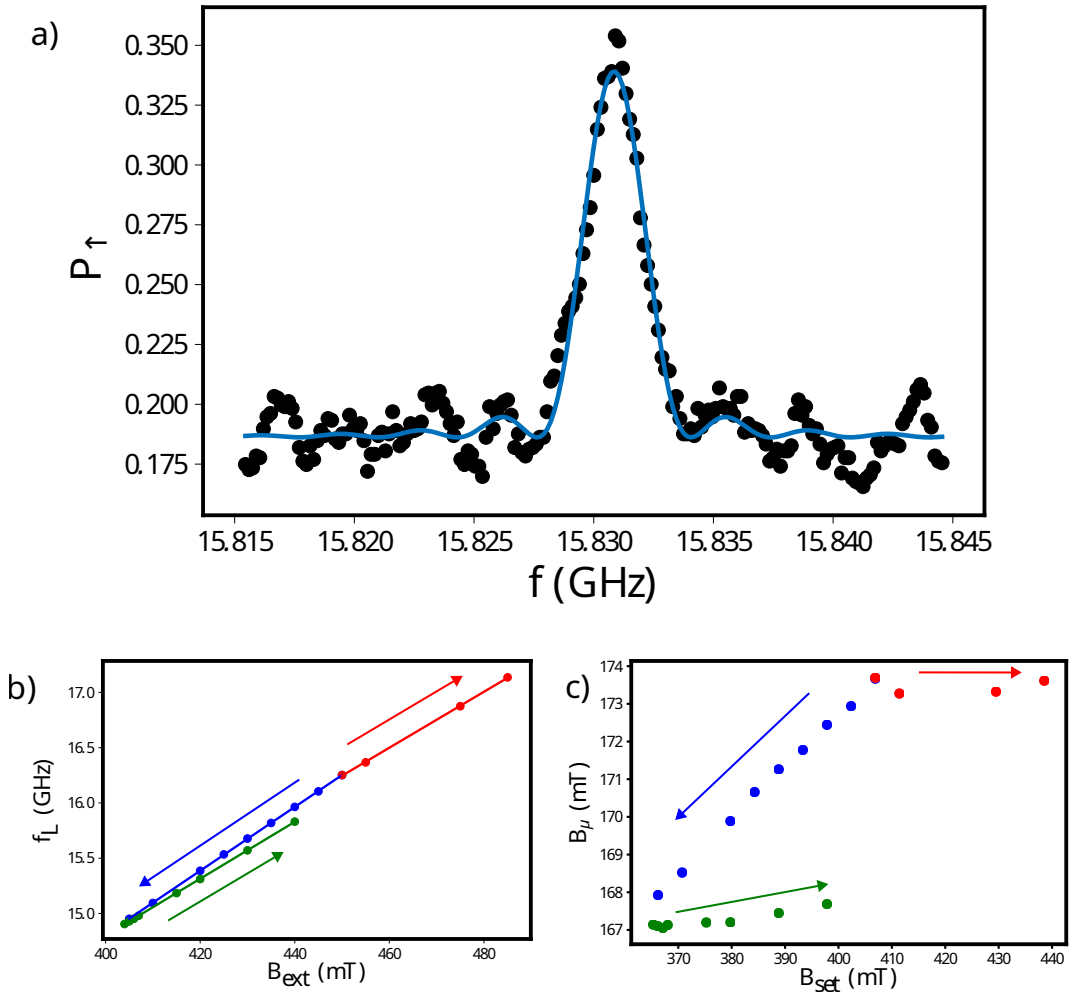

Figure 5.6: Larmor precession and micro-magnet hysteresis a) Determination of the Larmor frequency for a pulse duration of 400 ns. The spin up population $P_\uparrow$ is plotted against the excitation frequency f. The fit corresponds to formula 5.17. The central peak is used to determine the Larmor frequency f_L. **b)** Larmor frequencies f_L measured for different external magnetic fields B_{ext}. For the blue points the field was lowered monotonously, while it was increased monotonously for the green and red points as indicated by the arrows. The lines are linear fits to extract the correction factor and the micro-magnet stray field. **c)** Micro-magnet magnetization B_μ depending on the set magnetic field B_{set} for the same measurement sequences as in b).

5.5.2 Rabi oscillations

Rabi oscillations can be derived from formula 5.17 by imposing the resonance condition $f = f_L$. The expression then collapses into a simple cosine with the Rabi frequency f_R. Using the Bloch equations, a longitudinal spin relaxation time T_1 and a transversal decoherence time T_2 can be included in the model. As a result, the amplitude of the oscillations is suppressed exponentially with the characteristic times T_1 and T_2 [Blo46]. As $T_1 \approx 100\,\text{ms}$ is much longer than T_2, only the dominant T_2 decay is taken into account in

Eqn. 5.20. A is the initial amplitude, B a constant, T_2^{Rabi} the decoherence time and t_p the pulse duration.

$$P_{\uparrow,Bloch}(t_p) = A \exp\left(-\frac{t_p}{T_2^{Rabi}}\right)(1 - \cos(2\pi f_R t_p)) + B \tag{5.20}$$

However, when the dynamics of a decoherence mechanism is slow compared to the dynamics of the quantum system, the Bloch equations do not hold anymore. Ref. [Kop07] describes an approach to model Rabi oscillations in a GaAs double quantum dot that is coupled to a nuclear spin bath. The nuclear spin bath is varying slowly compared to the Rabi oscillations and the coherence time T_2^*. The nuclear spin field is considered static during each realization of the experiment. When averaging over many realizations, the nuclear spin field changes and therefore the shape of the averaged curve changes to a power law decay and a universal phase shift of $\frac{\pi}{4}$ arises. In the limit of only one spin being in resonance, Eqn. 7 from Ref. [Kop07] can be adapted to a single spin qubit in natural silicon as in Eqn. 5.21.

$$P_{\uparrow,Koppens}(t_p) = \frac{A}{\sqrt{t_p}} \cos\left(2\pi f_R t_p + \frac{\pi}{4}\right) + B \tag{5.21}$$

A and B can be derived from the driving field, the external magnetic field and the mean value and variance of the nuclear spin field. As these quantities are inaccessible in the experiment, A and B are treated as fitting parameters.
For the experimental realization, a RF pulse with frequency f_L and variable length is send to the device. Fig. 5.7 a) shows Rabi oscillations recorded using the feedback method described previously. Initially, a spin down electron is loaded. Therefore, a minimal spin up population is observed. In an ideal experiment the initial population would be 0. However, thermal excitations initialize some spins in the spin up orientation. A pulse now rotates the spin up around the Bloch sphere. For a π pulse the spin is rotated up. In the ideal case a spin up population of 1 is expected. However only a level of 45 % is reached. First, the initial population of 20 % needs to be subtracted. However, the remaining discrepancy needs to be explained. Fluctuations in the Larmor frequency faster than the timescale of the feedback loop are a probable reason. For each experiment where the excitation frequency is not in resonance with the spin it will not be driven and therefore reduce the spin up population on average. For longer pulse durations the spin is rotated further around the Bloch sphere reaching again a minimum for a 2π pulse, but not at the same level of population as measured initially. The oscillation is repeated for longer pulse durations with decreasing amplitude until no more oscillations are visible for pulses longer then 20 µs. From a fit with Eqn. 5.21 $A = 0.07$, the Rabi frequency $f_R = 0.63$ MHz, as well as the offset $B = 0.34$ are extracted. The power j = 0.48 is close to the expected value of 0.5, as well as the phase $\Phi = 0.19\pi$ close to the expected value of 0.25π. A fit to an exponential decay does not fit the data. Therefore, a source of slow noise must be present in the device. Most likely the remaining nuclear spins in the natural silicon are the source.
In 5.7 b) measurements of the Larmor frequency and of Rabi oscillations are combined into a 2D color plot. On the y-axis the excitation frequency is varied as in Fig. 5.6 a) and on the x-axis the pulse duration is changed as in Fig. 5.7 a). The spin-up population

is plotted in color code. The vertical dashed line corresponds to the position where a typical measurement of the Larmor frequency would be taken and the horizontal dashed line corresponds to a measurement of the Rabi oscillations. The pattern is described by Eqn. 5.17. However, the characteristic chevron pattern observed in the literature is not visible due to the slow Rabi frequency and the fast dephasing. As discussed in Sec. 5.5.1 the first order side peaks are hidden in the central peak and higher order side peaks are not resolved, leading to the unusual pattern observed here.

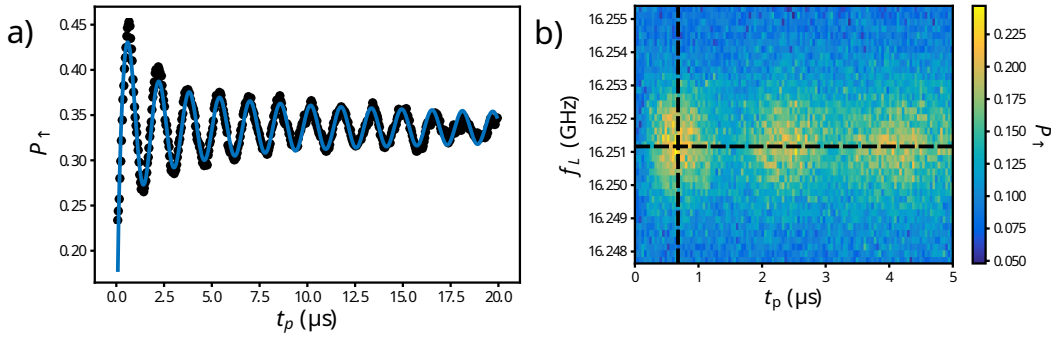

Figure 5.7: Rabi oscillations. a) Rabi oscillations measured over a pulse duration t_p of up to 20 µs. Characteristic oscillations in the spin up probability $P_\uparrow$ are observed by changing the duration of the RF burst send to the sample. The data is fitted with a cosine and a power law decay as described in Eqn. 5.21. **b)** Spin up population $P_\uparrow$ for pulse durations t_p up to 5 µs and excitation frequencies f_L around the Larmor frequency. On the y-axis the excitation frequency is varied and on the x-axis the pulse duration is changed. The spin up population is plotted in color code. The vertical dashed line corresponds to the position where a typical measurement of the Larmor frequency would be taken and the horizontal dashed line corresponds to a measurement of the Rabi oscillations. The characteristic chevron pattern observed in literature is not visible due to the slow Rabi frequency and the fast dephasing.

5.5.3 Power dependence of Rabi oscillations

Following from Eqn. 5.2 the Rabi frequency is proportional to the amplitude of the AC voltage that the electron feels. Hence, the Rabi frequency is proportional to the square root of the power [Pla12]. In Fig. 5.8 a) Rabi oscillations for different input powers are shown in a 2D color plot. A cut along the x-axis corresponds to a Rabi experiment like in Fig. 5.7 a). On the y-axis the input power at room temperature P_{in} is plotted and the population is encoded in the color scale. A cross like imperfection is visible in the plot, as the data has been merged from 4 different experiments in order to maintain a reasonable file size.

The input power at room temperature is plotted instead of the power that the electron feels, as it can only be estimated. On the one hand, the power can be estimated from the attenuation originating from the setup as described in Sec. 3.4.1. As a result a power of -30 dBm equivalent to 20 mV peak to peak arrives typically at the PCB. However, a significant additional attenuation is expected from the PCB, the bond wires and the device itself which can not be measured easily. On the other hand, Eqn. 5.2 together with the polarizability extracted from simulations described in Sec. 5.2 allows to estimate the driving strength to about 1 mV from the measured Rabi frequencies.

The Rabi frequency increases for larger powers while the coherence visibly reduces. In order to quantitatively verify the power dependence, the Rabi frequencies are extracted for each power are plotted against the square root of the input power in Fig. 5.8 b). For large input powers above 4 dBm the data follows a linear trend. However, the line fitted to the data does not go to the origin as expected. This is attributed to the transfer function of the active IQ mixer. Low input powers below 4 dBm are outside the specified power range of the mixer. Hence the signal is attenuated additionally, explaining the deviation from the linear trend.

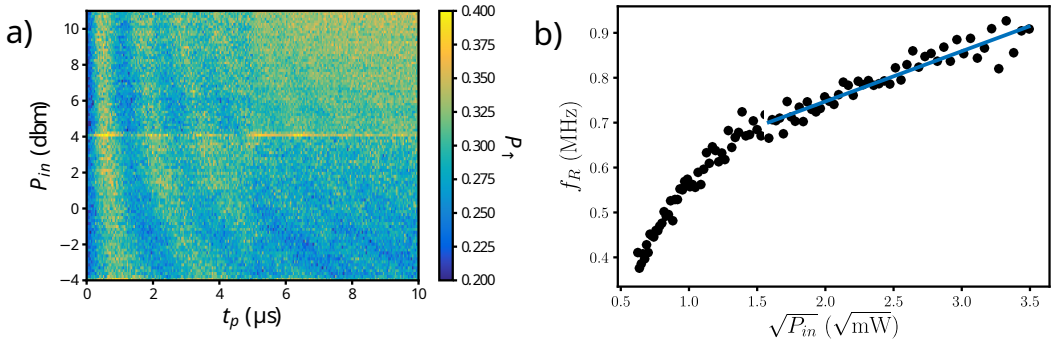

Figure 5.8: Rabi oscillations for different input powers. **a)** Rabi oscillations for different input RF powers P_{in}. The experiment in Fig. 5.7 is repeated for different RF input powers and stacked to a 2D plot with the spin up probability $P_\uparrow$ in color scale. A cross like imperfection is visible in the plot, as the data has been merged from 4 different experiments in order to maintain a reasonable file size. **b)** The Rabi frequency f_R goes linear with the square root of the input power $\sqrt{P_{in}}$ for large input powers. A deviation from the linear trend is observed at lower input powers, as they are outside of the specified power range of the mixer.

5.5.4 Valley enhanced EDSR

As the natural spin-orbit coupling (SOC) is weak in silicon, alternative methods to drive the electron spin are of great interest. In this thesis a micro-magnet is used to provide an artificial SOC to drive the spin efficiently. However, driving speeds are limited due to the poor polarizability of the corner dot forming in the nanowire. Corna et al. [Cor18] have shown that spin-orbit mediated EDSR can occur in a similar nanowire device at the spin-valley degeneracy. However, spin-orbit mediated EDSR alone was not strong enough to drive the spin coherently. With the device presented here, both mechanisms are present and can be studied simultaneously. To investigate the interplay between spin-valley mixing and spin-orbit coupling EDSR is performed as a function of the magnetic field [Cor18; Hao14; Hua17].

Fig. 5.9 b) presents example Rabi oscillations performed at different external magnetic fields. Only the external magnetic field including the correction found in Sec. 5.5.1 is plotted here, while in Sec. 5.4.2 the contribution of the micro-magnet was included, as well. It shows an increase of the Rabi frequency as the field gets closer to the valley hotspot (355 mT). This is supported by Fig. 5.9 a) which plots the Rabi frequency as a function of the magnetic field. The black line corresponds to a fit modeling the valley enhanced EDSR taking the strong hybridization of the spin and valley states at the spin-valley hotspot into

account. The underlying model is detailed in the next section.
A clear peak in Rabi frequency at 365 mT is followed by a slower decrease of Rabi frequency for larger magnetic fields. Between 370 mT and 380 mT Rabi oscillations that are strongly affected by heating and the points are therefore omitted. Rabi oscillations at the hotspot on the other hand are not affected by heating. The last two points were recorded with a micro-magnet voltage of -2.5 V instead of -3 V, as the device experienced a switch and had to be retuned. As a consequence Rabi frequencies increased making a correction of -0.62 MHz necessary. A measurement at 396 mT is repeated to obtain the frequency difference before and after retuning the device. It is worth noting that measurement further on the hotspot is prevented by the degraded spin readout fidelity due to fast spin relaxation and because of the Zeeman energy approaching the thermal energy.
This increase in Rabi frequency at the hotspot is related to the presence of a second drive mechanism which involves the presence of spin-valley mixing in the silicon quantum dot combined with synthetic spin-orbit coupling as described theoretically in Ref. [Hua21]. More precisely, the microwave electric field allows a transition from two different valleys but same spin ($|v_-, \downarrow\rangle$ and $|v_+, \downarrow\rangle$) and the synthetic SOC couples the two opposite spins in different valleys ($|v_-, \uparrow\rangle$ and $|v_+, \downarrow\rangle$) which eventually leads to an opposite spins and same valley transition ($|v_-, \uparrow\rangle$ to $|v_-, \downarrow\rangle$). The theory behind valley enhanced EDSR is explained in the next section and described in the literature in Ref. [Bou18; Cor18]. The Rabi frequency monotonously increases with the valley mixing which indicates that the two mechanisms are adding up resulting in a larger transverse field in the rotating frame. A more quantitative estimation of the amplitude and phase of the two components of the driving fields in the rotating frame is impractical here. It would require to change both the direction of the synthetic SOC field and the external magnetic field to map and disentangle the evolution of the two mechanisms in space.
While the presence of valleys offers an enhancement of EDSR driving speed it also increases the susceptibility of the qubit to charge noise. A similar trend between the Rabi frequency and the decoherence rate of Rabi oscillations is observed in Fig. 5.9 c). As the fit model in 5.21 does not include a decoherence rate, $T_{2,rabi}$ denotes in this case the time after which the envelop of the Rabi oscillation has decayed to 1/e. Ref. [Hua21] proposes a sweetspot for qubit operation this case. Close to the hotspot but not exactly at the hotspot, a maximum in quality factor is predicted. The simulated qubit driving strength and the simulated spin dephasing rate reach their maximum value at slightly different magnetic field in Ref. [Hua21] resulting in a sweetspot. However, no clear sweetspot is observed in this experiment. More precise measurements covering the entire spin-valley hotspot would be necessary to confirm or exclude the existence of a sweetspot.

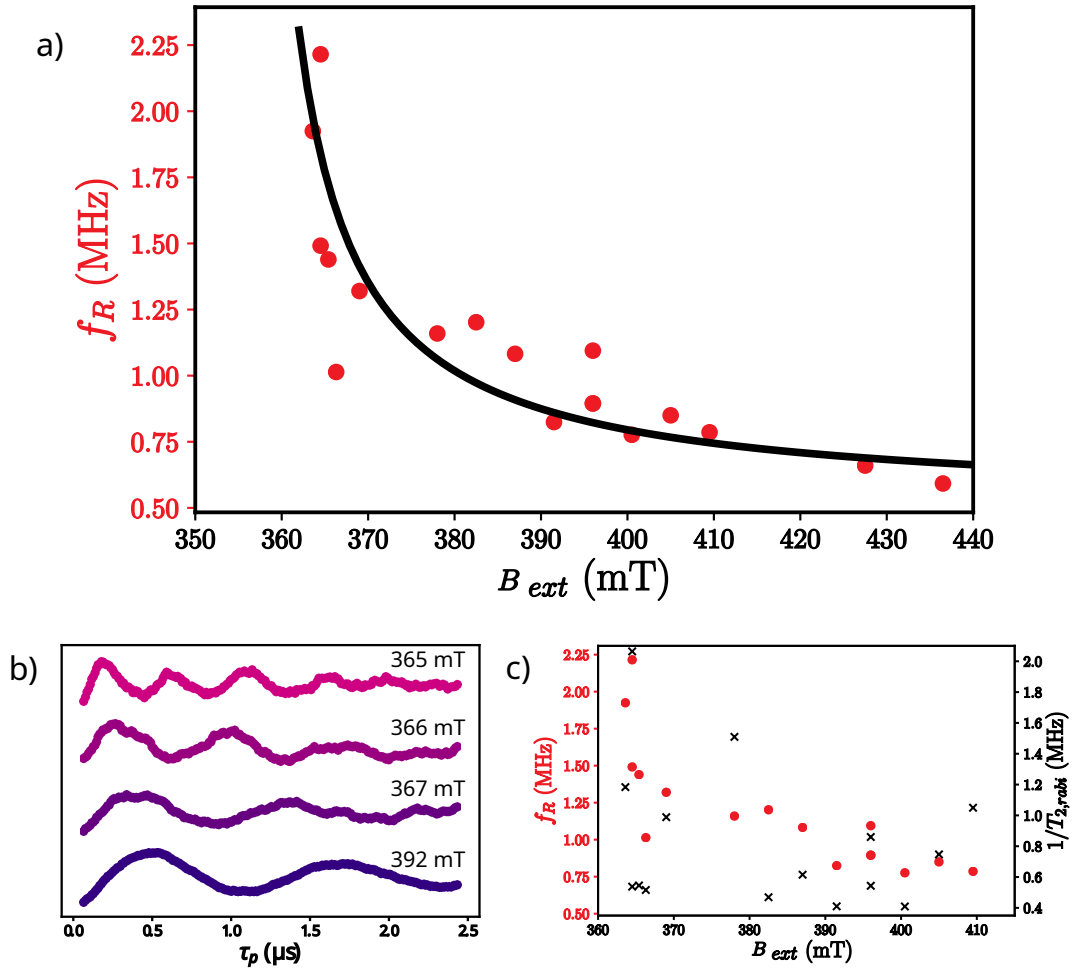

Figure 5.9: Valley enhanced EDSR a) Rabi frequency f_R as a function of the external applied magnetic field B. A clear peak in Rabi frequency at 365 mT is followed by a slower decrease of Rabi frequency for larger magnetic fields. Between 370 mT and 380 mT Rabi oscillations that are strongly affected by heating (cf. Fig. 5.8) and the points are therefore omitted. Rabi oscillations at the hotspot on the other hand are not affected by heating. The last two points were recorded with a micro-magnet voltage of -2.5 V instead of -3 V, as the device experienced a switch and had to be retuned. As a consequence Rabi frequencies increased making a correction of -0.62 MHz necessary. The black line corresponds to the model in Eqn. 5.38 with an additional offset of 0.5 MHz to account for the regular EDSR driving. $C_{v_1v_2} = 0.02\,\mu$eV corresponding to the spin-valley gap extracted before. **b)** Rabi oscillations at different magnetic fields noted on the right for a constant drive amplitude ($V_{AC} = 1$ mV) and pulse durations τ_p up to 2.5 µs. **c)** Rabi frequency f_R and characteristic decay rate for the Rabi oscillations $1/T_{2,Rabi}$ for different external magnetic fields B_{ext}. The decay rate follows roughly the trend of the Rabi frequency. No clear sweetspot in quality factor is observed in this experiment.

Theory

Due to the strong confinement of the quantum dot in the z-direction the six fold valley degeneracy in bulk silicon is lifted. The four in-plane $\pm\vec{k}_x$ and $\pm\vec{k}_y$ valleys are high in energy and inaccessible for the measurement. Only the lowest lying $\pm\vec{k}_z$ valleys are are accessible. The $-\vec{k}_z$ and $+\vec{k}_z$ state are also split in energy E_1 and E_2 by the valley splitting $E_2 - E_1 = E_{VS}$ due to the sharp potential at the Si/SiO_2 interface. The $-\vec{k}_z(+\vec{k}_z)$ valley state is denoted as $|v_1,\sigma\rangle(|v_2,\sigma\rangle)$ with $\sigma =\uparrow,\downarrow$ the spin index. The different valleys states are pretested in Fig. 5.10 a).
The spin degeneracy is lifted by the magnetic field via the Zeeman energy $E_Z = g\mu_B B$. The energies of the relevant subspace for qubit operation is shown in Fig. 5.10 b). When $E_Z = E_{VS}$ the $|v_1,\uparrow\rangle$ and $|v_2,\downarrow\rangle$ states anti-cross leading to a coupling of different valleys and different spins. This leads to an increased spin relaxation rate as shown in Sec. 5.4.2, but it can also be exploited to for valley enhanced EDSR.
The following discussion on the theory behind valley enhanced EDSR follows closely the supplementary note 2 of Ref. [Cor18]. The starting point for the non-perturbative model is the full Hamiltonian (Eqn. 5.22) in the $\{|v_1,\downarrow\rangle, |v_1,\uparrow\rangle, |v_2,\downarrow\rangle, |v_2,\uparrow\rangle\}$ subspace. The advantage is that this model is also valid at the anti-crossing.

$$H = \begin{pmatrix} E_1 - \frac{1}{2}g\mu_B B & 0 & -iR_{v_1v_2} & C^*_{v_1v_2} \\ 0 & E_1 + \frac{1}{2}g\mu_B B & -C_{v_1v_2} & iR_{v_1v_2} \\ iR_{v_1v_2} & -C^*_{v_1v_2} & E_2 - \frac{1}{2}g\mu_B B & 0 \\ C_{v_1v_2} & -iR_{v_1v_2} & 0 & E_2 + \frac{1}{2}g\mu_B B \end{pmatrix} \tag{5.22}$$

with g the Landé factor, μ_B the Bohr magneton and

$$C_{v_1v_2} = \langle v_2,\uparrow| H_{SOC} |v_1,\downarrow\rangle = -\langle v_1,\uparrow| H_{SOC} |v_2,\downarrow\rangle \tag{5.23}$$
$$R_{v_1v_2} = -i\langle v_2,\downarrow| H_{SOC} |v_1,\downarrow\rangle = -i\langle v_1,\uparrow| H_{SOC} |v_2,\uparrow\rangle \tag{5.24}$$

$C_{v_1v_2}$ couples different valleys and different spins via spin-orbit coupling. It corresponds to the spin-valley gap $\Delta_{SV} = 2|C_{v_1v_2}|$ defined in Sec. 5.4.2. $R_{v_1v_2}$ couples different valleys and same spins via spin-orbit coupling. As it couples same spins, the contribution of $R_{v_1v_2}$ can be neglected. As a consequence the Hamiltonian can be solved in two separate subspaces $\{|v_1,\downarrow\rangle, |v_2,\uparrow\rangle\}$ and $\{|v_1,\uparrow\rangle, |v_2,\downarrow\rangle\}$. The energy eigenvalues for the $\{|v_1,\downarrow\rangle, |v_2,\uparrow\rangle\}$ subspace are:

$$E_\pm = \frac{1}{2}(E_1 + E_2) \pm \frac{1}{2}\sqrt{(E_{VS} + g\mu_B B)^2 + 4|C_{v_1v_2}|^2} \tag{5.25}$$

and the eigenstates are:

$$|\Psi_+\rangle = \alpha|v_1,\downarrow\rangle + \beta|v_2,\uparrow\rangle \tag{5.26}$$
$$|\Psi_-\rangle = \beta|v_1,\downarrow\rangle - \alpha^*|v_2,\uparrow\rangle \tag{5.27}$$

with

$$\alpha = \frac{-2C_{v_1v_2}}{\sqrt{4|C_{v_1v_2}|^2 + W^2}} \tag{5.28}$$

$$\beta = \frac{W}{\sqrt{4|C_{v_1v_2}|^2 + W^2}} \tag{5.29}$$

and

$$W = E_{VS} + g\mu_B B + \sqrt{(E_{VS} + g\mu_B B)^2 + 4|C_{v_1v_2}|^2} \tag{5.30}$$

The energy eigenvalues for the $\{|v_1, \uparrow\rangle, |v_2, \downarrow\rangle\}$ subspace are:

$$E'_{\pm} = \frac{1}{2}(E_1 + E_2) \pm \frac{1}{2}\sqrt{(E_{VS} - g\mu_B B)^2 + 4|C_{v_1v_2}|^2} \tag{5.31}$$

and the eigenstates:

$$|\Psi'_+\rangle = \alpha' |v_1, \uparrow\rangle + \beta' |v_2, \downarrow\rangle \tag{5.32}$$

$$|\Psi'_-\rangle = \beta' |v_1, \uparrow\rangle - \alpha'^* |v_2, \downarrow\rangle \tag{5.33}$$

with

$$\alpha' = \frac{-2C_{v_1v_2}}{\sqrt{4|C_{v_1v_2}|^2 + W'^2}} \tag{5.34}$$

$$\beta' = \frac{W'}{\sqrt{4|C_{v_1v_2}|^2 + W'^2}} \tag{5.35}$$

and

$$W' = E_{VS} - g\mu_B B + \sqrt{(E_{VS} - g\mu_B B)^2 + 4|C_{v_1v_2}|^2} \tag{5.36}$$

With the eigenstates, the Rabi frequencies $f_{\pm}$ between the spin ground state $|\Psi_-\rangle$ and the mixed spin and valley states $|\Psi'_{\pm}\rangle$ can be calculated. f_- describes the Rabi frequencies for magnetic fields below the anti-crossing ($B < B_{VS}$) and f_+ describes the Rabi frequencies for magnetic fields above the anti-crossing ($B > B_{VS}$).

$$hf_- = e\delta V_g |\langle \Psi'_- | D | \Psi_- \rangle| = e\delta V_g |\alpha'\beta + \alpha^*\beta'||D_{v_1v_2}| \tag{5.37}$$

$$hf_+ = e\delta V_g |\langle \Psi'_+ | D | \Psi_- \rangle| = e\delta V_g |\alpha\alpha' + \beta\beta'||D_{v_1v_2}| \tag{5.38}$$

with the electric dipole matrix element between valleys v_1 and v_2

$$D_{v_1v_2} = \langle v_1,\sigma | D | v_2,\sigma \rangle = \langle v_2,\sigma | D | v_1,\sigma \rangle \tag{5.39}$$

Due to the $E_{VS} - g\mu_B B$ term in the mixed spin and valley states, the Rabi frequency reaches a maximum at B_{VS}. $C_{v_1v_2}$ determines the width of the peak and $D_{v_1v_2}$ determines the height of the peak.
The Rabi frequency data is obtained at magnetic fields above the hotspot. Therefore, f_+ is of interest to compare the data with the model. The model for f_+ can be expanded as

in Eqn. 5.40. Using the definition of W and W', f_+ becomes a function of the magnetic field with parameters E_{VS}, $|C_{v_1v_2}|$, δV_g and $|D_{v_1v_2}|$. E_{VS} and $|C_{v_1v_2}| = \frac{\Delta_{SV}}{2} = 0.02\,\mu\text{eV}$ are know. For δV_g exists an estimation of 1 mV and $|D_{v_1v_2}|$ can be obtained from the fit. The fit in Fig. 5.9 a) corresponds to the model in Eqn. 5.40 with an additional offset of 0.5 MHz to account for the regular EDSR driving. Finally, the electric dipole matrix element between valleys v_1 and v_2 $|D_{v_1v_2}|$ can be estimated to 3×10^{-10}.

$$f_+ = \frac{e\delta V_g}{h} \frac{4C^2 + WW'}{\sqrt{4C^2 + W^2}\sqrt{4C^2 + W'^2}} |D_{v_1v_2}| \tag{5.40}$$

The fit shows that the model for valley enhanced EDSR describes the data well. This suggests that indeed valley enhanced EDSR is observed.

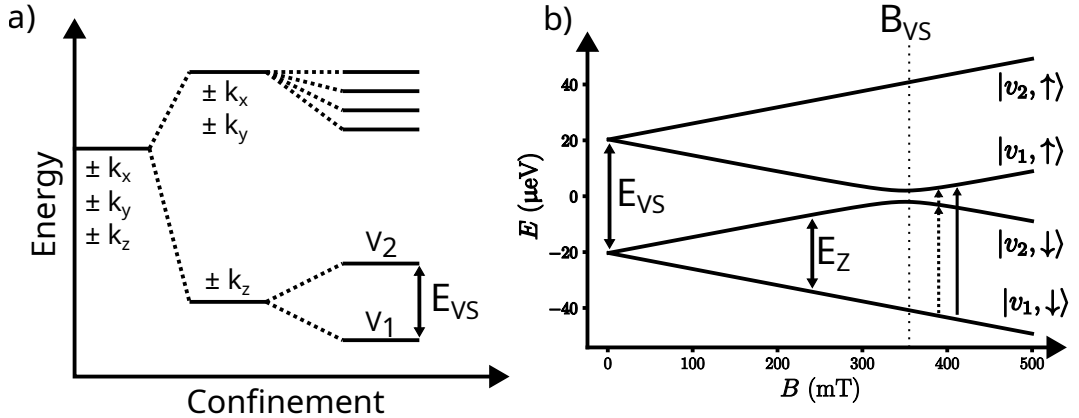

Figure 5.10: Theory valleys a) Valleys in silicon. Due to the strong confinement of the quantum dot in the z-direction the six fold valley degeneracy in bulk silicon is lifted. The four in-plane $\pm\vec{k}_x$ and $\pm\vec{k}_y$ valleys are high in energy and inaccessible for the measurement. Only the lowest $\pm\vec{k}_z$ lying valleys are are accessible. **b)** Energy E of the states $|v_1, \downarrow\rangle, |v_2, \uparrow\rangle, |v_1, \uparrow\rangle, |v_2, \downarrow\rangle$. The v_1 and the v_2 valley are split by the valley splitting E_{VS}. The spin degeneracy is lifted by the magnetic field via the Zeeman energy $E_Z = g\mu_B B$. The arrows illustrate valley enhanced EDSR. The solid arrow shows the regular EDSR drive coupling same valleys, but different spin directly. In the case of valley enhanced EDSR, the microwave electric field allows a transition from two different valleys but same spin ($|v_-, \downarrow\rangle$ and $|v_+, \downarrow\rangle$) and the synthetic SOC couples the two opposite spins in different valleys ($|v_-, \uparrow\rangle$ and $|v_+, \downarrow\rangle$), which eventually leads to an opposite spins and same valley transition ($|v_-, \uparrow\rangle$ to $|v_-, \downarrow\rangle$).

Alternative mechanisms

Next, alternative mechanisms to explain the increase in Rabi frequency are discussed. First, an additional observation is presented that needs explanation. Fig. 5.11 a) shows a calibration measurement that consists basically of a Larmor frequency measurement as in Fig. 5.6 a), but with the excitation frequency covering the entire bandwidth of the mixer. The magnetic field is set to an effective value of 542 mT that corresponds to a Larmor frequency of 15.184 GHz, which is indicated by the dashed line. The narrow peak expected at the Larmor frequency is not resolved and outside of this frequency no driving of the spin is expected as the qubit is out of resonance. However, the measurement reveals that

the population changes significantly with the excitation frequency over the entire range. A number of peaks in population become visible with a overall increase in population towards smaller excitation frequencies. This increase happens at the same frequencies or magnetic fields as the increase in Rabi frequency around the spin-valley hotspot discussed in the previous section.
As a result the population seems correlated to the increase in Rabi frequency. In order to visualize the correlation, the population is extracted for each point where the excitation frequency is equal to the Larmor frequency of a Rabi experiment in Fig. 5.9 a) and it is plotted against the Rabi frequency. The result is shown in 5.11 b). For small Rabi frequencies the population and Rabi frequency do not seem correlated, however for larger Rabi frequencies a correlation becomes apparent.
First, it is important to note that a correlation does not automatically implies a causal relation. Nevertheless an investigation is needed, if a plausible alternative to valley enhanced EDSR as the explanation of the increase in Rabi frequency exists. Such a mechanism has to increase the driving strength of the regular Rabi drive or it needs to introduce a second drive mechanism that acts on the same state.

Power A first option are fluctuations in the transmitted power. As discussed in Sec. 5.5.3 the Rabi frequency is proportional to the power arriving at the qubit. Therefore, a fluctuation in power could lead to an increase in Rabi frequency. Considering the ratio of the smallest Rabi frequency (0.59 MHz) and the largest Rabi frequency (2.23 MHz) measured, a difference in power of 11.6 dB would be necessary to explain the increase. The calibration measurement in Fig. 5.11 a) is repeated at three different input powers 0 dBm, 5 dBm, 11 dBm. The change in input power is comparable to the power difference needed to explain the increase in Rabi frequency, but still the impact on the calibration measurement is marginal. Hence, fluctuations in power do not explain the calibration experiment.
On the other hand power transmission of the RF lines changes depending on the excitation frequency due to imperfect impedance matching of the different components of the RF setup. VNA measurements of the setup as detailed in Sec. 3.4 show that the power transmission indeed changes with excitation frequency, but only at a rate of about 1 dB/GHz with fluctuations at most a few dB strong. Even though the VNA measurements do not take the effect of the PCB and the bond wires into account, fluctuations in the transmitted power seem too weak to explain the increase in Rabi frequency.

Heating The next explication that is considered is heating. Sending RF signals as well as baseband pulses to the qubit leads to local heating of the device. Heating effects have been reported to increase the thermal population and alter the shape of Rabi oscillations [Kaw14; Kaw16; Pla12]. Furthermore, shifts in the Larmor frequency due to heating from non-resonant driving have been reported [Fre17; Hen20a; Phi22; Sav23; Tak18; Wat18; Zwe22]. Recently, deeper investigations on the topic of heating have been conducted [Tak18; Und23a; Und23b]. The heating effect occurs within 100 ns, while cooling takes milliseconds according to Ref. [Und23b]. The limiting factor for cooling the device is found to be phononic thermal transport through the device to the metal ground plane of the PCB.

Heating can lead to thermal excitations inside the quantum dot, but affects the reservoirs as well. In combination with a irregular density of states in the reservoirs, an increase in population including the observed peaks could be explained by heating. However, there is no reason why this effect would increase strongly at the spin-valley hotspot in particular and why it would be correlated to the Rabi frequency.
Also the increase in Rabi frequency needs to be explained. A shift in Larmor frequency of up to 1 MHz is reported [Und23b]. A shift in Larmor frequency can in turn lead to off-resonant driving with an increased Rabi frequency as modeled in Eqn. 5.17. For the device measured in this thesis the width of the Larmor peak (5 MHz) is significantly larger than the reported shift. Therefore, the driving is mostly on-resonant with little effect on the Rabi frequency. Also the measured Chevron pattern for this device in Fig. 5.7 b) shows no increase in Rabi frequency for off-resonant driving due to the particular shape explained in Sec. 5.5.2. Heating effects can explain an increase in population in the calibration experiment, but there is no reason for a correlation. In addition, it is unlikely that heating explains the increase in Rabi frequency in this case.

Polarizability Also a change in polarizability can influence the Rabi frequency. The polarizability is introduced in the beginning of this chapter in Sec. 5.2. It is the displacement of an electron in response to an AC voltage applied to the gate. The polarizability is estimated to be 0.1 nm/mV and Eqn. 5.2 shows that the Rabi frequency depends linearly on the polarizability. Therefore, an increased polarizability would lead to an increased Rabi frequency. A irregular density of states in the reservoir that is populated depending on the excitation frequency could capacitively affect the polarizability of an electron inside the quantum dot. However, this effect is expected to be small as it relies purely on the capacitive effect. Plus there is no reason why this effect would be increase strongly at the spin-valley hotspot in particular. Therefore the polarizability changes only little compared to the change observed in Fig. 5.9 a). Hence a change in polarizability is unlikely and it is not sufficient to explain the data.

Resonant electrical transition Finally, the increase in population can be explained by resonant driving of a transition from two different valleys, but same spin ($|v_-, \downarrow\rangle$ and $|v_+, \downarrow\rangle$). It is the same process that enables valley enhanced EDSR, however the conventional drive mechanism coupling same valleys but different spin ($|v_-, \downarrow\rangle$ and $|v_-, \uparrow\rangle$) is not present. With the excitation frequency close to the valley splitting it is possible to drive the two different valleys, but same spin transition. If the electron remains in the $|v_+, \downarrow\rangle$ state, the readout needs to be performed before the electron relaxes to the $|v_-, \downarrow\rangle$ state. As the valley transition is not protected from charge noise in the same way as a spin transition, the relaxation time is typically too short to be measured.
Alternatively, the electron in the $|v_+, \downarrow\rangle$ state could be transfered into the $|v_-, \uparrow\rangle$ state via the synthetic SOC and therefore completing the valley enhanced EDSR protocol. This additional step might be possible as the calibration measurement is performed at a magnetic field close to the spin-valley hotspot. More calibration measurements at larger magnetic fields or without magnetic field would be necessary to conclude on this question. The

advantage of this approach is that it explains the increase in population, as well as the increase in Rabi frequency and the correlation between the two.
In conclusion, no alternative effect that could increase the Rabi frequency significantly is found. Therefore, valley enhanced EDSR is the most likely explanation of the observed increase in population as well as the increase in Rabi frequency and the correlation between the two.

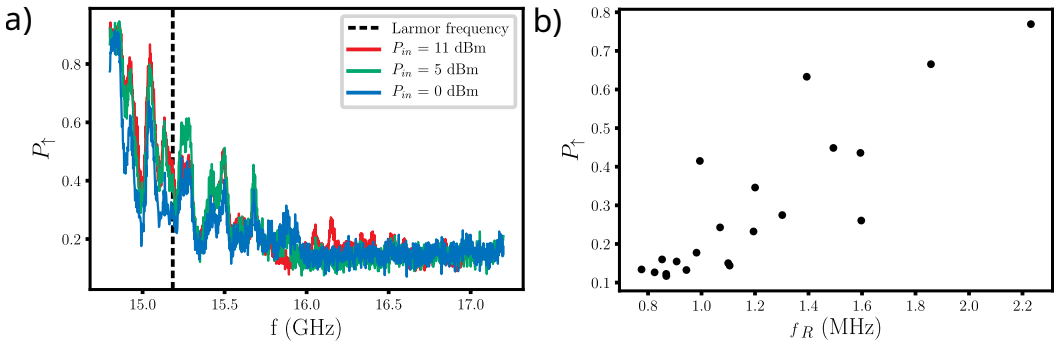

Figure 5.11: Population for non resonant driving and correlation to the Rabi frequency a) Population $P_\uparrow$ for non resonant driving with excitation frequency f for three different input powers P_{in}. A number of peaks in population become visible with an overall increase in population towards smaller excitation frequencies. **b)** Correlation between the population $P_\uparrow$ in a) and the Rabi frequency f_R measured in Fig. 5.9 a). For small Rabi frequencies the population and Rabi frequency do not seem correlated, however for larger Rabi frequencies a correlation becomes apparent.

5.6 Coherence

Quantum coherence describes the ability of a quantum system to maintain a definite phase relation between quantum states. If the qubit is completely isolated from its environment, there is no loss of coherence. However, a physical qubit is never perfectly isolated from the environment plus manipulation and measurement require coupling to the environment at certain times. As a result the phase relation is lost over time which is called decoherence. The decoherence is quantified by the coherence time T_2^*.
For a single spin qubit the situation can be illustrated in the Bloch sphere. The $|\uparrow\rangle$ and $|\downarrow\rangle$ states are at the poles of the Bloch sphere and the azimuthal angle Φ describes the phase between the two states. The electron spin only couples directly to magnetic noise such as the Overhauser field of the nuclear spin bath or fluctuations in the external magnetic field. Indirectly the electron spin can couple to charge noise via SOC. In silicon the SOC is low, but the micro-magnet introduces synthetic SOC. As a result the phase relationship is lost over time when the electron spin is not in one of the eigenstates. In this section the coherence of the qubit is studied first and ways to extend the coherence using dynamical decoupling is are presented.
The coherence time can be extracted from the measurement of the Larmor frequency and from Hahn echo experiments. A first estimate for the coherence time can be obtained from the measurements of the Larmor precession. The Larmor frequency can slightly vary due

to a change in resonance condition caused by noise and therefore the peak around the Larmor frequency broadens when measured repeatedly. Fitted with a Lorentzian, T_2^* is inversely proportional to the full width half maximum Δf_{FWHM} of the peak as in Eqn. 5.41 [Sli90].

$$T_2^* = \frac{1}{\pi \Delta f_{FWHM}} \tag{5.41}$$

For the measurement in Fig. 5.12 a) a coherence time of about 130 ns is extracted for a experiment duration of 1 h. For longer experiment durations the Larmor frequency explores a wider spectrum of frequencies resulting in a broader peak.
In order to understand the broadening, Larmor spectroscopy is used to track the evolution of the qubit energy over time. For this purpose the Larmor frequency is measured over three days. Using Fourier transform the noise power spectral density (PSD) curve is constructed in Fig. 5.12 b). It shows fluctuations as strong as 10 MHz at low frequency, which is in good agreement with hyperfine interaction in natural silicon devices [Pla12]. To fit the experimental data, a hyperfine model of nuclear spins with only three clusters in the frequency window is used. Saturation of the PSD at very low frequency is obtained as expected for a finite number of fluctuators, but the expected $1/f^2$ regime at higher frequencies is not reached due the small measurement bandwidth in this case. In the following, the Larmor frequency is recalibrated every minute to minimize the influence of this quasi-static noise.

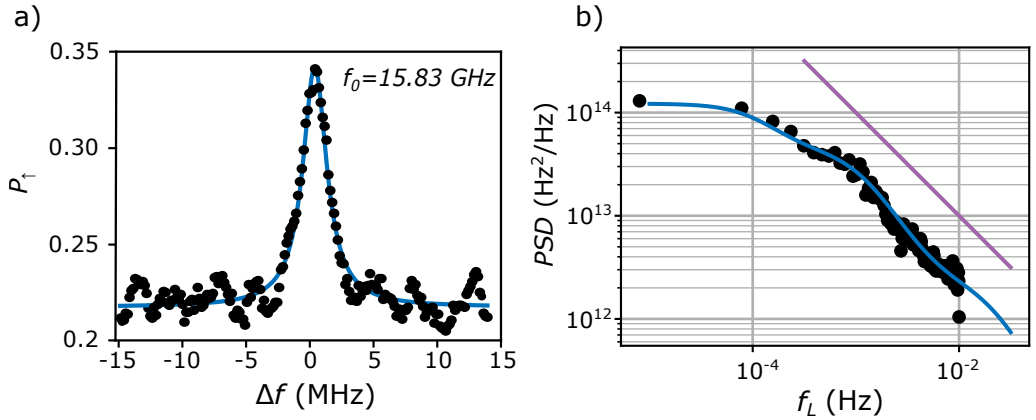

Figure 5.12: Larmor spectroscopy a) EDSR spectrum of the single electron spin. The spin up state probability $P_\uparrow$ is measured as a function of the excitation frequency Δf. The peak is centered around the Larmor frequency f_L. **b)** Power spectral density of the qubit frequency. The Larmor frequency f_L is measured over three days followed by a Fourier transform (black dots). The fit (blue) corresponds to a model including three nuclear spins at different fluctuating frequencies. The $1/f$ trend is depicted with the purple line.

The next method to obtain the coherence time discussed here is via the Hahn Echo. For this experiment the spin is initialized in the $|\downarrow\rangle$ state and a $\pi_x/2$ rotation around the x-axis in the Bloch sphere is performed. A $\pi_x/2$ rotation corresponds to a RF pulse of duration $\frac{1}{4f_R}$ that rotates the spin in the equatorial plane. Hence a superposition between

the $|\uparrow\rangle$ and $|\downarrow\rangle$ state is prepared. During a first delay τ_1 the spin dephases. With the following π_y pulse around the y-axis the spin is rotated to the other side of the equatorial plane. Quasi-static noise then acts inversely on the spin, resulting in a refocusing of the spin. If the second delay τ_2 has the same duration as the first one, most of the phase is recovered after a final $\pi_x/2$ rotation. The echo is shown in Fig. 5.13 a). The duration of the second delay is varied and the measured population is plotted against the difference between τ_1 and τ_2 called $\Delta\tau_w$. As a result the entire echo becomes visible. The broadening represents the effect of the quasi-static noise acting on the spin during dephasing and therefore provides an estimate for the coherence time. When fitted to a Gaussian as in Eqn. 5.42, the coherence time is given by the full width half maximum of the echo. The variance C of the echo is then related to the coherence time $T_2^* = 2\sqrt{2\ln(2)}C$ [Pla12].

$$P_\uparrow = B\exp\left[-\frac{1}{2}\left(\frac{\Delta\tau_w}{C}\right)^2\right] + D \tag{5.42}$$

As a result, a T_2^* of about 500 ns is extracted. The effective experiment duration is about 1 min, as the feedback loop corrects for changes in the Larmor frequency at this rate. Therefore, the longer coherence time compared to the Larmor linewidth is expected.
The Hahn echo experiment can also be used to extend the coherence time. Thanks to the refocusing, phase information that seemed lost can be recovered and the effect of quasi-static noise is canceled out. An echo can be observed after much longer evolution times $\tau = \tau_1 + \tau_2$ than the coherence time T_2^*. The reduced amplitude of the echo represents the effect of high frequency noise that can not be refocused. As a result, the echo becomes smaller and broader. When measured for different evolution times the normalized amplitude of the echo A can be fitted using Eqn. 5.43 [Kaw16] with the noise color α.

$$A(\tau) = \exp\left[-(\frac{\tau}{T_2^{HE}})^{1+\alpha}\right] \tag{5.43}$$

The decay of the normalized echo amplitude is shown in Fig. 5.13 b). The Hahn echo coherence time is $T_2^{HE} = 36\,\mu s$.
In comparison, the two coherence times differ, but their difference can be explained by the effective experiment duration. As all advanced experiments are performed using a feedback loop, the coherence time of 500 ns extracted from the Hahn echo is the appropriate value to consider. The difference with reported values in natural silicon [Kaw14; Tak16] is explained by a smaller size of the quantum dot leading to a shorter hyperfine-induced dephasing. A calculation of the wavefunction size from the group of Yann-Michel Niquet from CEA IRIG showed that the quantum dot volume is approximately an ellipsoid of main axis (2 nm,6 nm, 9 nm) [Mar22]. This gives a volume around 400 nm^3, which is one order of magnitude smaller than standard SiGe quantum dots [Str20].

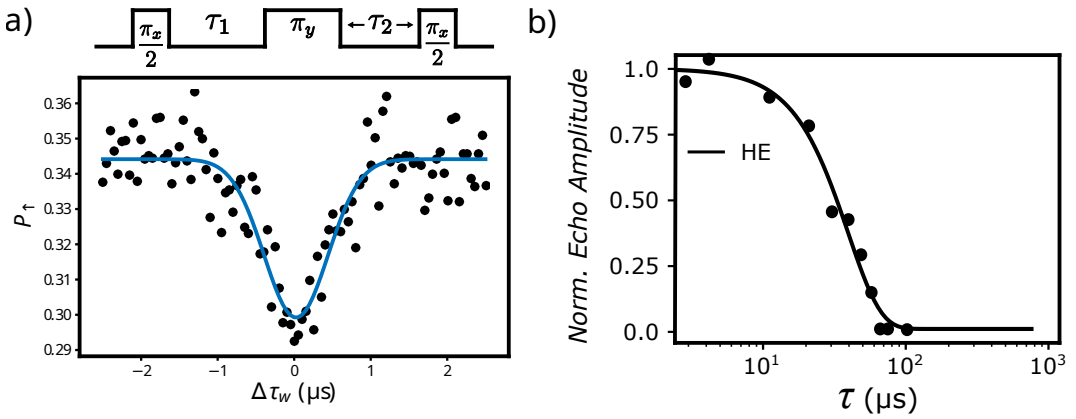

Figure 5.13: Coherence times a) Echo envelope measured using a Hahn echo sequence leading to a T_2^* of 500 ns. The spin-up population $P_\uparrow$ is plotted against the difference between the delays $\Delta\tau_w$ in the Hahn echo experiment. **b)** Normalized echo amplitude as a function of total free evolution time τ of the Hahn echo. For each Hahn echo experiment the echo is renormalized using the reference echo amplitude for τ= 1 µs.

5.7 Conclusion

In this chapter an electron spin qubit based on a CMOS process and post-processed with a micro-magnet is successfully characterized.

First, the design of the device and the micro-magnet is elucidated. The basis is an industrially fabricated quantum dot device those dimensions were chosen to optimize energy selective spin readout. In the academic fabrication, the device is contacted with Ti/Al gates. A FeCo micro-magnet is added to provide a magnetic field gradient for efficient spin driving via EDSR. Simulations of the micro-magnet give a transverse gradient of $\frac{dB_y}{dz}$ = 0.81 mT/nm and a longitudinal gradient of $\frac{dB_z}{dz}$ = -0.055 mT/nm. Together with simulations of the polarizability of 0.1 nm/mV a Rabi frequency of 1.14 MHz is estimated.

Next, a quantum dot below each gate is formed with one acting as a sensor and the other as a qubit. The qubit dot is tuned to the last electron and transitions suitable for spin readout are found. With the help of the gate lever arm (0.28 eV/V) extracted from Coulomb diamonds, the electron temperature is estimated to be 400 mK.

The spin is measured using energy selective spin readout with a charge fidelity of $F_c = 0.987$ and $F_{nc} = 0.995$ resulting in a visibility of $V = F_c F_{nc} = 0.982$. A limited spin visibility of 78 % is extracted from a measurement of the spin relaxation time. The spin relaxation rate is measured for different magnetic field showing an overall relaxation rate compatible with Johnson-Nyquist noise. The spin-valley hotspot is visible at 0.52 T which corresponds to a valley splitting of 60 µV and a spin-valley mixing strength of 0.04 µeV.

Spin manipulation is achieved via EDSR. In a first step, the external magnetic field is corrected and the stray field of the micro-magnet is estimated to be 167 mT using measurements of the Larmor frequency. Rabi oscillations are recorded next and fitted with a power law decay proposed in [Kop07]. A Rabi frequency of 0.63 MHz is extracted and the characteristic power law decay and the universal phase shift is observed. This indicates that a source of slow noise must be present in the device, most likely the remaining nuclear

spins in the natural silicon. An increase in Rabi frequency by more than a factor of 2 at the spin-valley hotspot is observed. The increase is explained by valley enhanced EDSR. Alternative mechanisms are considered, but none of them can fully explain the increase in Rabi frequency. Finally, the coherence time is determined via the Larmor linewidth and the spread of the Hahn echo. For an effective experiment duration of 1 min, a $T_2^* = 500\,\mathrm{ns}$ is extracted, which is limited by the hyperfine interaction of the remaining nuclear spins. Using a Hahn echo, the quasi-static noise limiting T_2^* can be refocused extending the coherence to $T_2^{HE} = 36\,\mu\mathrm{s}$.

The device presented here is a proof-of-principle demonstrating that an electron spin qubit based on industrial FD-SOI devices is possible. Towards the goal of building a quantum computer with these devices a number of improvements need to be made. First, the charge stability over longer periods of time needs to be improved. The device suffered from a constant drift of the stability diagram and occasional switches that limited the measurement time in a fixed configuration for comparable results. Currently spin readout is only possible at a very limited number of charge transitions. The spin measurements would potentially benefit from cleaner reservoirs that could be created for instance by gates instead of doping. For spin manipulation an improved polarizability would increase the Rabi drive significantly. The nuclear spin bath is currently the strongest source of decoherence at low frequencies. Hence, the coherence time as well as the Rabi decay are expected to greatly benefit from the introduction of isotopically purified ^{28}Si. Finally, valley enhanced EDSR may enable faster driving speeds for improved qubit quality in the future, however the existence of a sweetspot for qubit operation still needs to be proven.

In conclusion the qubit performance is comparable to pioneering spin qubit realizations on other material systems [Kaw14; Pla12]. The measurements presented in this chapter provide first experimental evidence for valley enhanced EDSR and demonstrate an electron spin qubit on a FD-SOI substrate for the first time.

CHAPTER 6

Conclusion and Outlook

6.1 Conclusion

At the heart of this thesis are intermediate solutions to bridge the gap between academic and industrial fabrication of spin qubits. While devices made fully by industrial CMOS standards make great progress, certain designs, processes and materials remain difficult to integrate. This thesis demonstrated that post-CMOS processing is a platform for proof-of-concepts and material characterization that can close this gap. Post-CMOS processing was performed at two different stages in this thesis. First, a preprocessed industrial FD-SOI wafer was used to implement test structures for transistor measurements, Hall bar measurements and quantum dot formation. Second, a single electron spin qubit in a CMOS device was studied with a micro-magnet integrated in a flexible BEOL.

6.1.1 Characterization

For material characterization a FD-SOI wafer was prepared at CEA-Leti with ohmic contacts and an active area. The minimal processing gave the academic fabrication a maximum freedom, while the substrate is shared with the industrial platform. This combination has enabled the characterization of Hall bars and quantum dot devices that are not available on the regular mask set used for the industrial process.
Transistor measurements performed on Hall bars gave insights into leakage, the device resistance and the turn on behavior at different temperatures. The threshold voltage at room temperature is around 0.7 V, while it is around 1 V at 4 K and 400 mK. A subthreshold swing of 125 mV/dec is extracted at room temperature, 91 mV/dec at 4 K and 92 mV/dec at 400 mK. The threshold voltage increases for lower temperatures and the subthreshold swing decreases as expected. The subthreshold swing is well above the theoretical minimum of 60 mV/dec at room temperature and also larger than the values for a typical transistor of 70 mV/dec.
The mobility and additional insights into the properties of the 2DEG can be gained from Hall bar measurements. By measuring the classical and the quantum Hall effect, the electron mobility and the corresponding density is extracted. The percolation density is estimated to be around $1\times10^{12}\,\mathrm{cm}^{-2}$. A peak mobility of $(2350 \pm 20)\,\mathrm{cm}^2/\mathrm{Vs}$ is reached at a density of $(3.48 \pm 0.05)\times10^{12}\,\mathrm{cm}^{-2}$ resulting in a maximum mean free path of 72 nm. The Fermi wavelength at the percolation density is about 25 nm and 13 nm at the electron density of maximum mobility. For larger densities the mobility is reduced despite the increase in electron density. Here the electrons start to feel the surface roughness, which effectively acts as scattering centers reducing the mobility. The conductance plateaus of the quantum Hall effect determine the number of filled Landau levels in the range between

28 and 40. A quantum lifetime of 0.15 ps corresponding to a Landau level broadening of 2.1 meV is extracted from a fit to the envelop of the SdH oscillations. The large broadening explains why neither the spin nor the valley splitting is resolved. In comparison to the literature [Sab19], the percolation density is an order of magnitude larger in this thesis, while the maximum mobility significantly smaller in this thesis. The main limiting factor is the small equivalent oxide thickness of 6.3 nm in this work, while the values in the literature range from 10 nm to 190 nm. The thicker oxide mitigates the effect of the granularity of the gates and the strain caused by the gates.
Quantum dot devices are very sensitive probes of their electrical environment. Fabricated on the same chip as the Hall bars they revealed defects relevant at very low electron densities and close to the quantum dot. On a different wafer from a new batch quantum dot measurements show that the charge stability is greatly improved, but the device quality was still insufficient for qubit operation.

6.1.2 Electron spin qubit

The second way post-CMOS processing is applied are complete industrial devices that are taken out of the fabrication before the BEOL. In the academic part of the fabrication, a micro-magnet is integrated in a flexible BEOL for efficient spin driving via EDSR. A device with a single pair of split gates was successfully contacted and the FeCo micro-magnet has been added.
In a first step, a quantum dot below each gate was formed with one acting as a sensor and the other as a qubit. The qubit dot was tuned to the last electron and transitions suitable for spin readout were found. With the help of the gate lever arm (0.28 eV/V) extracted from Coulomb diamonds, the electron temperature was estimated to 400 mK.
The electron spin was measured using energy selective spin readout with a charge fidelity of $F_c = 0.987$ and $F_{nc} = 0.995$ resulting in a visibility of $V = F_c F_{nc} = 0.982$. A limited spin visibility of 78 % was extracted from a measurement of the spin relaxation. The spin relaxation rate is measured for different magnetic fields showing an overall relaxation rate compatible with Johnson-Nyquist noise. The spin-valley hotspot is visible at 0.52 T which corresponds to a valley splitting of 60 µV and a spin-valley mixing strength of 0.04 µeV.
Spin manipulation is achieved via EDSR. First, the external magnetic field is corrected and the stray field of the micro-magnet is estimated to be 167 mT using measurements of the Larmor frequency. Rabi oscillations are recorded next and fitted with a power law decay proposed in [Kop07]. A Rabi frequency of 0.63 MHz is extracted and the characteristic power law decay and the universal phase shift is observed. This indicates that a source of slow noise must be present in the device, most likely the remaining nuclear spins in the natural silicon. When measured for different magnetic fields, an increase in Rabi frequency by more than a factor of 2 at the spin-valley hotspot is observed. The increase is explained by valley enhanced EDSR. Alternative mechanisms are considered, but none of them can fully explain the increase in Rabi frequency.
Finally, the coherence time is determined via the Larmor linewidth and the spread of the Hahn echo. For an effective experiment duration of 1 min, a $T_2^* = 500$ ns is extracted, which is limited by the hyperfine interaction of the remaining nuclear spins. Using a Hahn echo, the quasi-static noise limiting T_2^* can be refocused extending the coherence to $T_2^{HE} = 36$ µs.

In conclusion the qubit performance is comparable to pioneering spin qubit realizations on other material systems [Kaw14; Pla12]. The measurements provide first experimental evidence for valley enhanced EDSR and demonstrate an electron spin qubit using FD-SOI technology for the first time.

6.2 Outlook

The question is now, how electron spin qubits based on CMOS technology can evolve in order to achieve the next milestones that their academic counter parts have already reached. Ultimately the question is how they can benefit from the scalability that foundry based CMOS technology promises.
From the characterization measurements the large percolation density and the small mobility offers a route for improvement. These characteristics can be attributed mainly to the small gate oxide thickness of the devices. The thicker oxide mitigates the effect of the granularity of the gates and the strain caused by the gates. However, a thicker gate oxide also reduces the gate lever arm, as well as the control of the gate over the quantum dot. A compromise needs to be found for optimal quantum dot formation and gate control. Mobility measurements on devices that are made with the same industrial process as the qubit devices are necessary confirm the findings in this thesis and they offer an opportunity to monitor the process quality.
The proof-of-principle of an electron spin qubit has been successfully demonstrated in this thesis, but a number of potential improvements can be deducted from the measurements. Charge stability measurements show that quantum dots can be reliably formed, but the stability over time was limited by a constant drift and occasional switches. Here, the quality of the electronic environment needs to be improved, which may be connected to the low mobilities reported before. Also the impact of the reservoirs that are formed by doping in the close vicinity of the device needs to be investigated.
Spin readout is possible at low magnetic fields compatible spin manipulation. The limited fidelity needs to be improved and again the reliability needs to be addressed. Currently spin readout is only possible at a very limited number of charge transitions. First, an improvement in electron temperature would improve the spin readout and second spin measurements would potentially benefit from cleaner reservoirs that could be created for instance by gates instead of doping. This way the reservoirs can be purely defined by the gates field effect. Improved fidelities using energy selective spin readout have been reported on a similar device [Spe22]. Also, high fidelity singlet-triplet readout was demonstrated at elevated temperatures [Nie22] showing that high fidelity spin readout can be incorporated.
For spin manipulation an improved polarizability would increase the Rabi drive significantly. The nuclear spin bath is currently the strongest source of decoherence. Hence, the coherence time as well as the Rabi decay are expected to greatly benefit from the introduction of isotopically purified ^{28}Si. Finally, valley enhanced EDSR may enable faster driving speeds for improved qubit quality in the future, however the existence of a sweetspot for qubit operation still needs to be proven.
By realizing the improvements above, the next milestone should be in reach. Demonstrating high fidelity single qubit operation and performing randomized benchmarking is an important step to show the viability of electron spin qubits on a FD-SOI platform.

Post-CMOS-processing can be again of use to realize the proof-of-concept as academic implementations using a micro-magnet report the highest fidelities [Yon18]. In order to benefit from the fast qubit manipulation that EDSR via a micro-magnet offers, substantial progress needs to be made on the polarizability and the low driving speeds reported in this thesis. If this is not possible, spin manipulation using ESR via a stripline in combination with an isotopically purified channel can be a route to high single qubit fidelities. Devices fully processed by CMOS standards based on bulk technology have demonstrated qubit operation using this method [Zwe22] and a similar approach is in preparation for FD-SOI technology [Jac23]. Using ESR via a stripline for spin manipulation avoids the charge noise that can be coupled in by the micro-magnet. The drawback of this method is that driving speeds are typically well below 1 MHz. However, if the current driving speeds do not improve, ESR could enable high qubit fidelities thanks to optimized coherence times.
Next, two qubit and multi qubit operation should be addressed. Devices with multiple gates and additional exchange gates are under investigation [Paz22]. Multiple quantum dots are controlled by a first layer of gates and exchange gates for coupling neighboring quantum dots are placed in between the first layer of gates. This type of devices will enable two qubit gates and paves the road for a multi qubit array.
Finally, a unit cell and interconnections between the unit cells have to be defined that integrate into an architecture for a larger quantum computer [Van17]. Foundry based fabrication starts shining at this point, as it is expected to scale the unit cells rapidly.

Bibliography

[Aar08] Aaronson, S.: 'The limits of quantum'. *Scientific American* (2008), vol. 298(March): pp. 62–69 (cit. on p. 3).

[Ach23] Acharya, R. et al.: 'Suppressing quantum errors by scaling a surface code logical qubit'. *Nature* (Feb. 2023), vol. 614(7949): pp. 676–681 (cit. on p. 6).

[Akh23] Akhtar, M., F. Bonus, F. R. Lebrun-Gallagher, N. I. Johnson, M. Siegele-Brown, S. Hong, S. J. Hile, S. A. Kulmiya, S. Weidt, and W. K. Hensinger: 'A high-fidelity quantum matter-link between ion-trap microchip modules'. *Nature Communications* (Feb. 2023), vol. 14(1): p. 531 (cit. on p. 6).

[Akk07] Akkermans, E. and G. Montambaux: *Mesoscopic Physics of Electrons and Photons*. Cambridge University Press, May 2007 (cit. on p. 66).

[Ama08] Amasha, S., K. MacLean, I. P. Radu, D. M. Zumbühl, M. A. Kastner, M. P. Hanson, and A. C. Gossard: 'Electrical Control of Spin Relaxation in a Quantum Dot'. *Physical Review Letters* (Jan. 2008), vol. 100(4): p. 046803 (cit. on p. 80).

[Ans20] Ansaloni, F., A. Chatterjee, H. Bohuslavskyi, B. Bertrand, L. Hutin, M. Vinet, and F. Kuemmeth: 'Single-electron operations in a foundry-fabricated array of quantum dots'. *Nature Communications* (Dec. 2020), vol. 11(1): p. 6399 (cit. on pp. 9, 34, 73).

[Aru19] Arute, F. et al.: 'Quantum supremacy using a programmable superconducting processor'. *Nature* (2019), vol. 574(7779): pp. 505–510 (cit. on p. 6).

[Bal16] Ballance, C. J., T. P. Harty, N. M. Linke, M. A. Sepiol, and D. M. Lucas: 'High-Fidelity Quantum Logic Gates Using Trapped-Ion Hyperfine Qubits'. *Physical Review Letters* (2016), vol. 117(6): pp. 1–6 (cit. on p. 6).

[Bar14] Barends, R. et al.: 'Superconducting quantum circuits at the surface code threshold for fault tolerance'. *Nature* (2014), vol. 508(7497): pp. 500–503 (cit. on p. 6).

[Bar10] Barthel, C., M. Kjærgaard, J. Medford, M. Stopa, C. M. Marcus, M. P. Hanson, and A. C. Gossard: 'Fast sensing of double-dot charge arrangement and spin state with a radio-frequency sensor quantum dot'. *Physical Review B* (Apr. 2010), vol. 81(16): p. 161308 (cit. on p. 22).

[Bee91] Beenakker, C. W. J.: 'Theory of Coulomb-blockade oscillations in the conductance of a quantum dot'. *Physical Review B* (July 1991), vol. 44(4): pp. 1646–1656 (cit. on p. 13).

[Blo46] Bloch, F.: 'Nuclear Induction'. *Physical Review* (Oct. 1946), vol. 70(7-8): pp. 460–474 (cit. on p. 91).

[Blu10] Bluhm, H., S. Foletti, D. Mahalu, V. Umansky, and A. Yacoby: 'Enhancing the Coherence of a Spin Qubit by Operating it as a Feedback Loop That Controls its Nuclear Spin Bath'. *Physical Review Letters* (Nov. 2010), vol. 105(21): p. 216803 (cit. on p. 8).

[Blu11] Bluhm, H., S. Foletti, I. Neder, M. Rudner, D. Mahalu, V. Umansky, and A. Yacoby: 'Dephasing time of GaAs electron-spin qubits coupled to a nuclear bath exceeding 200 μs'. *Nature Physics* (Feb. 2011), vol. 7(2): pp. 109–113 (cit. on p. 8).

[Bor20] Borjans, F., X. G. Croot, X. Mi, M. J. Gullans, and J. R. Petta: 'Resonant microwave-mediated interactions between distant electron spins'. *Nature* (Jan. 2020), vol. 577(7789): pp. 195–198 (cit. on p. 9).

[Bou18] Bourdet, L. and Y.-M. Niquet: 'All-electrical manipulation of silicon spin qubits with tunable spin-valley mixing'. *Physical Review B* (Apr. 2018), vol. 97(15): p. 155433 (cit. on p. 95).

[Bra18] Brauns, M., S. V. Amitonov, P.-C. Spruijtenburg, and F. A. Zwanenburg: 'Palladium gates for reproducible quantum dots in silicon'. *Scientific Reports* (Dec. 2018), vol. 8(1): p. 5690 (cit. on p. 38).

[Bru19] Bruzewicz, C. D., J. Chiaverini, R. McConnell, and J. M. Sage: 'Trapped-ion quantum computing: Progress and challenges'. *Applied Physics Reviews* (June 2019), vol. 6(2): p. 021314 (cit. on p. 6).

[Cas06] Casse, M., L. Thevenod, B. Guillaumot, L. Tosti, F. Martin, J. Mitard, O. Weber, F. Andrieu, T. Ernst, G. Reimbold, T. Billon, M. Mouis, and F. Boulanger: 'Carrier transport in HfO_2 metal gate MOSFETs: physical insight into critical parameters'. *IEEE Transactions on Electron Devices* (Apr. 2006), vol. 53(4): pp. 759–768 (cit. on p. 71).

[Cha20] Chanrion, E. et al.: 'Charge detection in an array of CMOS quantum dots'. *Physical Review Applied* (2020), vol. 14(2): p. 1 (cit. on pp. 9, 34, 73, 77).

[Chi13] Childress, L. and R. Hanson: 'Diamond NV centers for quantum computing and quantum networks'. *MRS Bulletin* (Feb. 2013), vol. 38(2): pp. 134–138 (cit. on p. 8).

[Cir21] Ciriano-Tejel, V. N., M. A. Fogarty, S. Schaal, L. Hutin, B. Bertrand, L. Ibberson, M. F. Gonzalez-Zalba, J. Li, Y.-M. Niquet, M. Vinet, and J. J. Morton: 'Spin Readout of a CMOS Quantum Dot by Gate Reflectometry and Spin-Dependent Tunneling'. *PRX Quantum* (Mar. 2021), vol. 2(1): p. 010353 (cit. on pp. 9, 73, 87).

[Con22] Contamin, L., B. C. Paz, B. M. Diaz, B. Bertrand, H. Niebojewski, V. Labracherie, A. Sadik, E. Catapano, M. Casse, E. Nowak, Y.-M. Niquet, F. Gaillard, T. Meunier, P.-A. Mortemousque, and M. Vinet: 'Methodology for an efficient characterization flow of industrial grade Si-based qubit devices'. *2022 International Electron Devices Meeting (IEDM)*. IEEE, Dec. 2022: pp. 22.1.1–22.1.4 (cit. on p. 51).

[Cor18] Corna, A., L. Bourdet, R. Maurand, A. Crippa, D. Kotekar-Patil, H. Bohuslavskyi, R. Laviéville, L. Hutin, S. Barraud, X. Jehl, M. Vinet, S. De Franceschi, Y.-M. Niquet, and M. Sanquer: 'Electrically driven electron spin resonance mediated by spin–valley–orbit coupling in a silicon quantum dot'. *npj Quantum Information* (Dec. 2018), vol. 4(1): p. 6 (cit. on pp. 9, 38, 73, 75, 94, 95, 97).

[Deu92] Deutsch, D. and R. Jozsa: 'Rapid Solution of Problems by Quantum Computation'. *Proceedings of the Royal Society A: Mathematical, Physical and Engineering Sciences* (Dec. 1992), vol. 439(1907): pp. 553–558 (cit. on p. 1).

[Dow03] Dowling, J. P. and G. J. Milburn: 'Quantum technology: the second quantum revolution'. *Philosophical Transactions of the Royal Society of London. Series A: Mathematical, Physical and Engineering Sciences* (Aug. 2003), vol. 361(1809): pp. 1655–1674 (cit. on p. 1).

[Elh23] Elhomsy, V. et al.: 'Broadband parametric amplification for multiplexed SiMOS quantum dot signals'. *arXiv: 2307.14717* (July 2023), vol.: pp. 1–12 (cit. on pp. 11, 34).

[Elz04] Elzerman, J. M., R. Hanson, L. H. Willems van Beveren, B. Witkamp, L. M. K. Vandersypen, and L. P. Kouwenhoven: 'Single-shot read-out of an individual electron spin in a quantum dot'. *Nature* (July 2004), vol. 430(6998): pp. 431–435 (cit. on pp. 8, 80).

[Feh59] Feher, G.: 'Electron Spin Resonance Experiments on Donors in Silicon. I. Electronic Structure of Donors by the Electron Nuclear Double Resonance Technique'. *Physical Review* (June 1959), vol. 114(5): pp. 1219–1244 (cit. on p. 90).

[Fey82] Feynman, R. P.: 'Simulating physics with computers'. *International Journal of Theoretical Physics* (1982), vol. 21(6-7): pp. 467–488 (cit. on p. 1).

[Fow12] Fowler, A. G., M. Mariantoni, J. M. Martinis, and A. N. Cleland: 'Surface codes: Towards practical large-scale quantum computation'. *Physical Review A* (Sept. 2012), vol. 86(3): p. 032324 (cit. on p. 1).

[Fre17] Freer, S., Simmons, A. Laucht, J. T. Muhonen, J. P. Dehollain, R. Kalra, F. A. Mohiyaddin, F. E. Hudson, K. M. Itoh, J. C. McCallum, D. N. Jamieson, A. S. Dzurak, and A. Morello: 'A single-atom quantum memory in silicon'. *Quantum Science and Technology* (Mar. 2017), vol. 2(1): p. 015009 (cit. on p. 100).

[Fri18] Friis, N., O. Marty, C. Maier, C. Hempel, M. Holzäpfel, P. Jurcevic, M. B. Plenio, M. Huber, C. Roos, R. Blatt, and B. Lanyon: 'Observation of Entangled States of a Fully Controlled 20-Qubit System'. *Physical Review X* (Apr. 2018), vol. 8(2): p. 021012 (cit. on p. 6).

[Ful87] Fulton, T. A. and G. J. Dolan: 'Observation of single-electron charging effects in small tunnel junctions'. *Physical Review Letters* (July 1987), vol. 59(1): pp. 109–112 (cit. on p. 13).

[Gil20] Gilbert, W., A. Saraiva, W. H. Lim, C. H. Yang, A. Laucht, B. Bertrand, N. Rambal, L. Hutin, C. C. Escott, M. Vinet, and A. S. Dzurak: 'Single-Electron Operation of a Silicon-CMOS 2 × 2 Quantum Dot Array with Integrated Charge Sensing'. *Nano Letters* (Nov. 2020), vol. 20(11): pp. 7882–7888 (cit. on pp. 9, 34, 73).

[Gon21] Gonzalez-Zalba, M. F., S. de Franceschi, E. Charbon, T. Meunier, M. Vinet, and A. S. Dzurak: 'Scaling silicon-based quantum computing using CMOS technology'. *Nature Electronics* (Dec. 2021), vol. 4(12): pp. 872–884 (cit. on p. 12).

[Gor51] Gorter, C.: 'A possible explanation of the increase of the electrical resistance of thin metal films at low temperatures and small field strengths'. *Physica* (Aug. 1951), vol. 17(8): pp. 777–780 (cit. on p. 13).

[Gro18] Gross, R. and A. Marx: *Festkörperphysik*. De Gruyter, Jan. 2018 (cit. on p. 58).

[Gro96] Grover, L. K.: 'A fast quantum mechanical algorithm for database search'. *Proceedings of the twenty-eighth annual ACM symposium on Theory of computing - STOC '96*. New York, USA: ACM Press, 1996: pp. 212–219 (cit. on p. 1).

[Han07] Hanson, R., L. P. Kouwenhoven, J. R. Petta, S. Tarucha, and L. M. K. Vandersypen: 'Spins in few-electron quantum dots'. *Reviews of Modern Physics* (Oct. 2007), vol. 79(4): pp. 1217–1265 (cit. on p. 13).

[Hao14] Hao, X., R. Ruskov, M. Xiao, C. Tahan, and H. Jiang: 'Electron spin resonance and spin-valley physics in a silicon double quantum dot'. *Nature Communications* (2014), vol. 5(May): pp. 1–8 (cit. on p. 94).

[Hen20a] Hendrickx, N. W., D. P. Franke, A. Sammak, G. Scappucci, and M. Veldhorst: 'Fast two-qubit logic with holes in germanium'. *Nature* (Jan. 2020), vol. 577(7791): pp. 487–491 (cit. on p. 100).

[Hen20b] Hendrickx, N. W., W. I. Lawrie, L. Petit, A. Sammak, G. Scappucci, and M. Veldhorst: 'A single-hole spin qubit'. *Nature Communications* (2020), vol. 11(1) (cit. on p. 9).

[Hen21] Hendrickx, N. W., W. I. L. Lawrie, M. Russ, F. van Riggelen, S. L. de Snoo, R. N. Schouten, A. Sammak, G. Scappucci, and M. Veldhorst: 'A four-qubit germanium quantum processor'. *Nature* (Mar. 2021), vol. 591(7851): pp. 580–585 (cit. on p. 9).

[Hof06] Hofheinz, M., X. Jehl, M. Sanquer, G. Molas, M. Vinet, and S. Deleonibus: 'Simple and controlled single electron transistor based on doping modulation in silicon nanowires'. *Applied Physics Letters* (Oct. 2006), vol. 89(14): p. 143504 (cit. on p. 9).

[Hos21] Hosseinkhani, A. and G. Burkard: 'Relaxation of single-electron spin qubits in silicon in the presence of interface steps'. *Physical Review B* (2021), vol. 104(8) (cit. on pp. 8, 87).

[Hua21] Huang, P. and X. Hu: 'Fast spin-valley-based quantum gates in Si with micromagnets'. *npj Quantum Information* (Dec. 2021), vol. 7(1): p. 162 (cit. on p. 95).

[Hua14] Huang, P. and X. Hu: 'Spin relaxation in a Si quantum dot due to spin-valley mixing'. *Physical Review B* (Dec. 2014), vol. 90(23): p. 235315 (cit. on p. 85).

[Hua17] Huang, W., M. Veldhorst, N. M. Zimmerman, A. S. Dzurak, and D. Culcer: 'Electrically driven spin qubit based on valley mixing'. *Physical Review B* (Feb. 2017), vol. 95(7): p. 075403 (cit. on p. 94).

[Iba09] Ibach, H. and H. Lüth: *Solid-State Physics*. Berlin, Heidelberg: Springer Berlin Heidelberg, 2009 (cit. on p. 14).

[Ihn09] Ihn, T.: *Semiconductor Nanostructures*. Oxford University Press, Nov. 2009: pp. 1–10 (cit. on p. 2).

[Ito14] Itoh, K. M. and H. Watanabe: 'Isotope engineering of silicon and diamond for quantum computing and sensing applications'. *MRS Communications* (Dec. 2014), vol. 4(4): pp. 143–157 (cit. on p. 8).

[Jac23] Jacquinot, H., R. Maurand, G. T. Fernández-Bada, B. Bertrand, M. Cassé, Y. M. Niquet, S. de Franceschi, T. Meunier, and M. Vinet: 'RF simulation platform of qubit control using FDSOI technology for quantum computing'. *Solid-State Electronics* (2023), vol. 199: pp. 1–11 (cit. on p. 110).

[Jad21] Jadot, B., P.-A. Mortemousque, E. Chanrion, V. Thiney, A. Ludwig, A. D. Wieck, M. Urdampilleta, C. Bäuerle, and T. Meunier: 'Distant spin entanglement via fast and coherent electron shuttling'. *Nature Nanotechnology* (May 2021), vol. 16(5): pp. 570–575 (cit. on p. 8).

[Kan98] Kane, B. E.: 'A silicon-based nuclear spin quantum computer'. *Nature* (May 1998), vol. 393(6681): pp. 133–137 (cit. on p. 8).

[Kaw14] Kawakami, E., P. Scarlino, D. R. Ward, F. R. Braakman, D. E. Savage, M. G. Lagally, M. Friesen, S. N. Coppersmith, M. A. Eriksson, and L. M. K. Vandersypen: 'Electrical control of a long-lived spin qubit in a Si/SiGe quantum dot.' *Nat. Nano.* (2014), vol. 9(9): p. 666 (cit. on pp. 9, 100, 104, 106, 109).

[Kaw16] Kawakami, E., T. Jullien, P. Scarlino, D. R. Ward, D. E. Savage, M. G. Lagally, V. V. Dobrovitski, M. Friesen, S. N. Coppersmith, M. A. Eriksson, and L. M. K. Vandersypen: 'Gate fidelity and coherence of an electron spin in an Si/SiGe quantum dot with micromagnet'. *Proceedings of the National Academy of Sciences* (Oct. 2016), vol. 113(42): pp. 11738–11743 (cit. on pp. 100, 104).

[Kei19] Keith, D., S. K. Gorman, L. Kranz, Y. He, J. G. Keizer, M. A. Broome, and M. Y. Simmons: 'Benchmarking high fidelity single-shot readout of semiconductor qubits'. *New Journal of Physics* (June 2019), vol. 21(6): p. 063011 (cit. on p. 84).

[Kle23] Klemt, B. et al.: 'Electrical manipulation of a single electron spin in CMOS using a micromagnet and spin-valley coupling'. *npj Quantum Information* (Oct. 2023), vol. 9(1): p. 107 (cit. on p. 12).

[Kop06] Koppens, F. H. L., C. Buizert, K. J. Tielrooij, I. T. Vink, K. C. Nowack, T. Meunier, L. P. Kouwenhoven, and L. M. K. Vandersypen: 'Driven coherent oscillations of a single electron spin in a quantum dot'. *Nature* (Aug. 2006), vol. 442(7104): pp. 766–771 (cit. on p. 8).

[Kop07] Koppens, F. H. L., D. Klauser, W. A. Coish, K. C. Nowack, L. P. Kouwenhoven, D. Loss, and L. M. K. Vandersypen: 'Universal Phase Shift and Nonexponential Decay of Driven Single-Spin Oscillations'. *Physical Review Letters* (Sept. 2007), vol. 99(10): p. 106803 (cit. on pp. 92, 105, 108).

[Kou97] Kouwenhoven, L. P., T. H. Oosterkamp, M. W. S. Danoesastro, M. Eto, D. G. Austing, T. Honda, and S. Tarucha: 'Excitation Spectra of Circular, Few-Electron Quantum Dots'. *Science* (Dec. 1997), vol. 278(5344): pp. 1788–1792 (cit. on p. 8).

[Law20] Lawrie, W. I. L. et al.: 'Quantum dot arrays in silicon and germanium'. *Applied Physics Letters* (Feb. 2020), vol. 116(8): p. 080501 (cit. on p. 38).

[Lek17] Lekitsch, B., S. Weidt, A. G. Fowler, K. Mølmer, S. J. Devitt, C. Wunderlich, and W. K. Hensinger: 'Blueprint for a microwave trapped ion quantum computer'. *Science Advances* (2017), vol. 3(2): e1601540 (cit. on p. 6).

[Llo96] Lloyd, S.: 'Universal Quantum Simulators'. *Science* (Aug. 1996), vol. 273(5278): pp. 1073–1078 (cit. on p. 1).

[Los98] Loss, D. and D. P. DiVincenzo: 'Quantum Computation with Quantum Dots'. *Physical Review A* (1998), vol. 57(1): p. 12 (cit. on p. 7).

[Mad22] Madzik, M. T. et al.: 'Precision tomography of a three-qubit donor quantum processor in silicon'. *Nature* (Jan. 2022), vol. 601(7893): pp. 348–353 (cit. on pp. 8, 73).

[Mar22] Martinez, B. and Y.-M. Niquet: 'Variability of Electron and Hole Spin Qubits Due to Interface Roughness and Charge Traps'. *Physical Review Applied* (Feb. 2022), vol. 17(2): p. 024022 (cit. on pp. 76, 104).

[Mau16] Maurand, R., X. Jehl, D. Kotekar-Patil, A. Corna, H. Bohuslavskyi, R. Laviéville, L. Hutin, S. Barraud, M. Vinet, M. Sanquer, and S. De Franceschi: 'A CMOS silicon spin qubit'. *Nature Communications* (Nov. 2016), vol. 7: p. 13575 (cit. on pp. 9, 11, 34, 40, 73).

[Mi17] Mi, X., M. Benito, S. Putz, D. M. Zajac, J. M. Taylor, G. Burkard, and J. R. Petta: 'A Coherent Spin-Photon Interface in Silicon'. (Oct. 2017), vol.: pp. 1–19 (cit. on p. 9).

[Mil22] Mills, A. R., C. R. Guinn, M. J. Gullans, A. J. Sigillito, M. M. Feldman, E. Nielsen, and J. R. Petta: 'Two-qubit silicon quantum processor with operation fidelity exceeding 99%'. *Science Advances* (Apr. 2022), vol. 8(14): pp. 1–6 (cit. on pp. 9, 10, 73).

[Moo06] Moore, G. E.: 'Cramming more components onto integrated circuits, Reprinted from Electronics, volume 38, number 8, April 19, 1965, pp.114 ff.' *IEEE Solid-State Circuits Society Newsletter* (Sept. 2006), vol. 11(3): pp. 33–35 (cit. on p. 2).

[Mor10] Morello, A. et al.: 'Single-shot readout of an electron spin in silicon'. *Nature* (2010), vol. 467(7316): pp. 687–691 (cit. on pp. 8, 84).

[Mor21a] Mortemousque, P.-A., E. Chanrion, B. Jadot, H. Flentje, A. Ludwig, A. D. Wieck, M. Urdampilleta, C. Bäuerle, and T. Meunier: 'Coherent control of individual electron spins in a two-dimensional quantum dot array'. *Nature Nanotechnology* (Mar. 2021), vol. 16(3): pp. 296–301 (cit. on p. 8).

[Mor21b] Mortemousque, P.-A., B. Jadot, E. Chanrion, V. Thiney, C. Bäuerle, A. Ludwig, A. D. Wieck, M. Urdampilleta, and T. Meunier: 'Enhanced Spin Coherence while Displacing Electron in a Two-Dimensional Array of Quantum Dots'. *PRX Quantum* (Aug. 2021), vol. 2(3): p. 030331 (cit. on p. 8).

[Muh15] Muhonen, J. T., A. Laucht, S. Simmons, J. P. Dehollain, R. Kalra, F. E. Hudson, S. Freer, K. M. Itoh, D. N. Jamieson, J. C. McCallum, A. S. Dzurak, and A. Morello: 'Quantifying the quantum gate fidelity of single-atom spin qubits in silicon by randomized benchmarking'. *Journal of Physics: Condensed Matter* (Apr. 2015), vol. 27(15): p. 154205 (cit. on p. 8).

[Muh14] Muhonen, J. T., J. P. Dehollain, A. Laucht, F. E. Hudson, R. Kalra, T. Sekiguchi, K. M. Itoh, D. N. Jamieson, J. C. McCallum, A. S. Dzurak, and A. Morello: 'Storing quantum information for 30 seconds in a nanoelectronic device'. *Nature Nanotechnology* (Dec. 2014), vol. 9(12): pp. 986–991 (cit. on pp. 8, 73).

[Nak20] Nakajima, T., A. Noiri, K. Kawasaki, J. Yoneda, P. Stano, S. Amaha, T. Otsuka, K. Takeda, M. R. Delbecq, G. Allison, A. Ludwig, A. D. Wieck, D. Loss, and S. Tarucha: 'Coherence of a Driven Electron Spin Qubit Actively Decoupled from Quasistatic Noise'. *Physical Review X* (Mar. 2020), vol. 10(1): p. 011060 (cit. on p. 89).

[Neg11] Negara, M. A., D. Veksler, J. Huang, G. Ghibaudo, P. K. Hurley, G. Bersuker, N. Goel, and P. Kirsch: 'Analysis of effective mobility and hall effect mobility in high- k based In 0.75 Ga 0.25 As metal-oxide-semiconductor high-electron-mobility transistors'. *Applied Physics Letters* (Dec. 2011), vol. 99(23): p. 232101 (cit. on p. 71).

[Neu15] Neumann, R. and L. R. Schreiber: 'Simulation of micro-magnet stray-field dynamics for spin qubit manipulation'. *Journal of Applied Physics* (2015), vol. 117(19) (cit. on p. 75).

[Nie22] Niegemann, D. J. et al.: 'Parity and Singlet-Triplet High-Fidelity Readout in a Silicon Double Quantum Dot at 0.5 K'. *PRX Quantum* (Dec. 2022), vol. 3(4): p. 040335 (cit. on pp. 9, 34, 73, 77, 109).

[Nie12] Nielsen, M. A. and I. L. Chuang: *Quantum Computation and Quantum Information*. Cambridge University Press, June 2012 (cit. on p. 2).

[Noi22] Noiri, A., K. Takeda, T. Nakajima, T. Kobayashi, A. Sammak, G. Scappucci, and S. Tarucha: 'Fast universal quantum gate above the fault-tolerance threshold in silicon'. *Nature* (Jan. 2022), vol. 601(7893): pp. 338–342 (cit. on pp. 9, 73).

[Nur23] Nurizzo, M., B. Jadot, P.-A. Mortemousque, V. Thiney, E. Chanrion, D. Niegemann, M. Dartiailh, A. Ludwig, A. D. Wieck, C. Bäuerle, M. Urdampilleta, and T. Meunier: 'Complete Readout of Two-Electron Spin States in a Double Quantum Dot'. *PRX Quantum* (Mar. 2023), vol. 4(1): p. 010329 (cit. on p. 8).

[Oha07] Ohata, A., M. Cassé, and S. Cristoloveanu: 'Front- and back-channel mobility in ultrathin SOI-MOSFETs by front-gate split CV method'. *Solid-State Electronics* (Feb. 2007), vol. 51(2): pp. 245–251 (cit. on p. 71).

[Paq22] Paquelet Wuetz, B. et al.: 'Atomic fluctuations lifting the energy degeneracy in Si/SiGe quantum dots'. *Nature Communications* (2022), vol. 13(1): pp. 1–8 (cit. on p. 87).

[Paz22] Paz, B. C. et al.: 'Coupling control in the few-electron regime of quantum dot arrays using 2-metal gate levels in CMOS technology'. *ESSCIRC 2022- IEEE 48th European Solid State Circuits Conference (ESSCIRC)*. IEEE, Sept. 2022: pp. 45–48 (cit. on p. 110).

[Pet22] Petit, L., M. Russ, G. H. G. J. Eenink, W. I. L. Lawrie, J. S. Clarke, L. M. K. Vandersypen, and M. Veldhorst: 'Design and integration of single-qubit rotations and two-qubit gates in silicon above one Kelvin'. *Communications Materials* (Nov. 2022), vol. 3(1): p. 82 (cit. on p. 9).

[Pet05] Petta, J. R.: 'Coherent Manipulation of Coupled Electron Spins in Semiconductor Quantum Dots'. *Science* (Sept. 2005), vol. 309(5744): pp. 2180–2184 (cit. on p. 8).

[Phi22] Philips, S. G. J., M. T. Madzik, S. V. Amitonov, S. L. de Snoo, M. Russ, N. Kalhor, C. Volk, W. I. L. Lawrie, D. Brousse, L. Tryputen, B. P. Wuetz, A. Sammak, M. Veldhorst, G. Scappucci, and L. M. K. Vandersypen: 'Universal control of a six-qubit quantum processor in silicon'. *Nature* (Sept. 2022), vol. 609(7929): pp. 919–924 (cit. on pp. 9, 100).

[Pio08] Pioro-Ladrière, M., T. Obata, Y. Tokura, Y.-S. Shin, T. Kubo, K. Yoshida, T. Taniyama, and S. Tarucha: 'Electrically driven single-electron spin resonance in a slanting Zeeman field'. *Nature Physics* (Oct. 2008), vol. 4(10): pp. 776–779 (cit. on p. 8).

[Pio22] Piot, N. et al.: 'A single hole spin with enhanced coherence in natural silicon'. *Nature Nanotechnology* (Sept. 2022), vol. (cit. on pp. 9, 40, 73, 89).

[Pla12] Pla, J. J., K. Y. Tan, J. P. Dehollain, W. H. Lim, J. J. L. Morton, D. N. Jamieson, A. S. Dzurak, and A. Morello: 'A single-atom electron spin qubit in silicon'. *Nature* (Sept. 2012), vol. 489(7417): pp. 541–545 (cit. on pp. 8, 93, 100, 103, 104, 106, 109).

[Pla13] Pla, J. J.: 'Single atom spin qubits in silicon'. PhD thesis. UNSW, Sydney, Australia, 2013 (cit. on p. 84).

[Pow08] Powell, J. R.: 'The Quantum Limit to Moore's Law'. *Proceedings of the IEEE* (Aug. 2008), vol. 96(8): pp. 1247–1248 (cit. on p. 2).

[Pre18] Preskill, J.: 'Quantum Computing in the NISQ era and beyond'. *Quantum* (2018), vol. 2(July): p. 79 (cit. on p. 1).

[Pud02] Pudalov, V. M., M. E. Gershenson, H. Kojima, N. Butch, E. M. Dizhur, G. Brunthaler, A. Prinz, and G. Bauer: 'Low-Density Spin Susceptibility and Effective Mass of Mobile Electrons in Si Inversion Layers'. *Physical Review Letters* (Apr. 2002), vol. 88(19): p. 196404 (cit. on p. 72).

[Ran75] Randell, B.: *The Origins of Digital Computers*. Berlin, Heidelberg: Springer Berlin Heidelberg, 1975 (cit. on p. 2).

[Rom04] Romanjek, K., F. Andrieu, T. Ernst, and G. Ghibaudo: 'Improved Split C–V Method for Effective Mobility Extraction in sub-0.1-μ Si MOSFETs'. *IEEE Electron Device Letters* (Aug. 2004), vol. 25(8): pp. 583–585 (cit. on p. 71).

[Sab19] Sabbagh, D. et al.: 'Quantum Transport Properties of Industrial $^{28}Si/^{28}SiO_2$'. *Physical Review Applied* (July 2019), vol. 12(1): p. 014013 (cit. on pp. 58, 63, 65, 71, 72, 108).

[Sam18] Samkharadze, N., G. Zheng, N. Kalhor, D. Brousse, A. Sammak, U. C. Mendes, A. Blais, G. Scappucci, and L. M. K. Vandersypen: 'Strong spin-photon coupling in silicon.' *Science* (Mar. 2018), vol. 359(6380): pp. 1123–1127 (cit. on p. 9).

[Sav23] Savytskyy, R., T. Botzem, I. Fernandez de Fuentes, B. Joecker, J. J. Pla, F. E. Hudson, K. M. Itoh, A. M. Jakob, B. C. Johnson, D. N. Jamieson, A. S. Dzurak, and A. Morello: 'An electrically driven single-atom "flip-flop" qubit'. *Science advances* (2023), vol. 9(6): eadd9408 (cit. on p. 100).

[Sho97] Shor, P. W.: 'Polynomial-Time Algorithms for Prime Factorization and Discrete Logarithms on a Quantum Computer'. *SIAM Journal on Computing* (Oct. 1997), vol. 26(5): pp. 1484–1509 (cit. on p. 1).

[Sli90] Slichter, C. P.: *Principles of Magnetic Resonance*. Vol. 1. Springer Series in Solid-State Sciences. Berlin, Heidelberg: Springer Berlin Heidelberg, 1990 (cit. on p. 103).

[Spe23] Spence, C. et al.: 'Probing Low-Frequency Charge Noise in Few-Electron CMOS Quantum Dots'. *Physical Review Applied* (Apr. 2023), vol. 19(4): p. 044010 (cit. on pp. 77, 81, 85).

[Spe22] Spence, C. et al.: 'Spin-Valley Coupling Anisotropy and Noise in CMOS Quantum Dots'. *Physical Review Applied* (Mar. 2022), vol. 17(3): p. 034047 (cit. on pp. 9, 34, 73, 74, 77, 85–87, 109).

[Spr16] Spruijtenburg, P. C., S. V. Amitonov, F. Mueller, W. G. van der Wiel, and F. A. Zwanenburg: 'Passivation and characterization of charge defects in ambipolar silicon quantum dots'. *Scientific Reports* (Dec. 2016), vol. 6(1): p. 38127 (cit. on pp. 38, 41).

[Str20] Struck, T., A. Hollmann, F. Schauer, O. Fedorets, A. Schmidbauer, K. Sawano, H. Riemann, N. V. Abrosimov, L. Cywinski, D. Bougeard, and L. R. Schreiber: 'Low-frequency spin qubit energy splitting noise in highly purified 28Si/SiGe'. *npj Quantum Information* (May 2020), vol. 6(1): p. 40 (cit. on p. 104).

[Tak18] Takeda, K., J. Yoneda, T. Otsuka, T. Nakajima, M. R. Delbecq, G. Allison, Y. Hoshi, N. Usami, K. M. Itoh, S. Oda, T. Kodera, and S. Tarucha: 'Optimized electrical control of a Si/SiGe spin qubit in the presence of an induced frequency shift'. *npj Quantum Information* (Oct. 2018), vol. 4(1): p. 54 (cit. on p. 100).

[Tak16] Takeda, K., J. Kamioka, T. Otsuka, J. Yoneda, T. Nakajima, M. R. Delbecq, S. Amaha, G. Allison, T. Kodera, S. Oda, and S. Tarucha: 'A fault-tolerant addressable spin qubit in a natural silicon quantum dot'. *Science Advances* (2016), vol. 2(8): pp. 1–7 (cit. on p. 104).

[The17] Theis, T. N. and H.-S. P. Wong: 'The End of Moore's Law: A New Beginning for Information Technology'. *Computing in Science & Engineering* (Mar. 2017), vol. 19(2): pp. 41–50 (cit. on p. 2).

[Tur37] Turing, A. M.: 'On Computable Numbers, with an Application to the Entscheidungsproblem'. *Proceedings of the London Mathematical Society* (1937), vol. s2-42(1): pp. 230–265 (cit. on p. 2).

[Und23a] Undseth, B., X. Xue, M. Mehmandoost, M. Rimbach-Russ, P. T. Eendebak, N. Samkharadze, A. Sammak, V. V. Dobrovitski, G. Scappucci, and L. M. Vandersypen: 'Nonlinear Response and Crosstalk of Electrically Driven Silicon Spin Qubits'. *Physical Review Applied* (Apr. 2023), vol. 19(4): p. 044078 (cit. on p. 100).

[Und23b] Undseth, B. et al.: 'Hotter is Easier: Unexpected Temperature Dependence of Spin Qubit Frequencies'. *Physical Review X* (Oct. 2023), vol. 13(4): p. 041015 (cit. on pp. 100, 101).

[Urd19] Urdampilleta, M. et al.: 'Gate-based high fidelity spin readout in a CMOS device'. *Nature Nanotechnology* (Aug. 2019), vol. 14(8): pp. 737–741 (cit. on pp. 9, 34, 73, 75, 77).

[Van13] Van Meter, R. and D. Horsman: 'A blueprint for building a quantum computer'. *Communications of the ACM* (Oct. 2013), vol. 56(10): pp. 84–93 (cit. on pp. 8, 9, 73).

[Van17] Vandersypen, L. M. K., H. Bluhm, J. S. Clarke, A. S. Dzurak, R. Ishihara, A. Morello, D. J. Reilly, L. R. Schreiber, and M. Veldhorst: 'Interfacing spin qubits in quantum dots and donors—hot, dense, and coherent'. *npj Quantum Information* (Dec. 2017), vol. 3(1): p. 34 (cit. on p. 110).

[Van01] Vandersypen, L. M. K., M. Steffen, G. Breyta, C. S. Yannoni, M. H. Sherwood, and I. L. Chuang: 'Experimental realization of Shor's quantum factoring algorithm using nuclear magnetic resonance'. *Nature* (Dec. 2001), vol. 414(6866): pp. 883–887 (cit. on p. 5).

[Vel15] Veldhorst, M., C. H. Yang, J. C. C. Hwang, W. Huang, J. P. Dehollain, J. T. Muhonen, S. Simmons, A. Laucht, F. E. Hudson, K. M. Itoh, A. Morello, and A. S. Dzurak: 'A two-qubit logic gate in silicon'. *Nature* (Oct. 2015), vol. 526(7573): pp. 410–414 (cit. on p. 9).

[Vel17] Veldhorst, M., H. G. J. Eenink, C. H. Yang, and A. S. Dzurak: 'Silicon CMOS architecture for a spin-based quantum computer'. *Nature Communications* (Dec. 2017), vol. 8(1): p. 1766 (cit. on p. 12).

[Vel14] Veldhorst, M., J. C. C. Hwang, C. H. Yang, A. W. Leenstra, B. de Ronde, J. P. Dehollain, J. T. Muhonen, F. E. Hudson, K. M. Itoh, A. Morello, and A. S. Dzurak: 'An addressable quantum dot qubit with fault-tolerant control-fidelity'. *Nature Nanotechnology* (2014), vol. 9(12): pp. 981–985 (cit. on pp. 9, 10, 69, 85, 89).

[Voi14] Voisin, B., V.-H. Nguyen, J. Renard, X. Jehl, S. Barraud, F. Triozon, M. Vinet, I. Duchemin, Y.-M. Niquet, S. de Franceschi, and M. Sanquer: 'Few-Electron Edge-State Quantum Dots in a Silicon Nanowire Field-Effect Transistor'. *Nano Letters* (Apr. 2014), vol. 14(4): pp. 2094–2098 (cit. on p. 76).

[Vol21] Volmer, F., I. Seidler, T. Bisswanger, J. S. Tu, L. R. Schreiber, C. Stampfer, and B. Beschoten: 'How to solve problems in micro- and nanofabrication caused by the emission of electrons and charged metal atoms during e-beam evaporation'. *Journal of Physics D: Applied Physics* (2021), vol. 54(22) (cit. on p. 40).

[Wat18] Watson, T. F., S. G. J. Philips, E. Kawakami, D. R. Ward, P. Scarlino, M. Veldhorst, D. E. Savage, M. G. Lagally, M. Friesen, S. N. Coppersmith, M. A. Eriksson, and L. M. K. Vandersypen: 'A programmable two-qubit quantum processor in silicon'. *Nature* (Mar. 2018), vol. 555(7698): pp. 633–637 (cit. on p. 100).

[Wee88] Wees, B. J. van, H. van Houten, C. W. J. Beenakker, J. G. Williamson, L. P. Kouwenhoven, D. van der Marel, and C. T. Foxon: 'Quantized conductance of point contacts in a two-dimensional electron gas'. *Physical Review Letters* (Feb. 1988), vol. 60(9): pp. 848–850 (cit. on p. 22).

[Wie02] Wiel, W. G. van der, S. De Franceschi, J. M. Elzerman, T. Fujisawa, S. Tarucha, and L. P. Kouwenhoven: 'Electron transport through double quantum dots'. *Reviews of Modern Physics* (Dec. 2002), vol. 75(1): pp. 1–22 (cit. on pp. 13, 21, 77).

[Wil20] Willsch, D., M. Willsch, H. De Raedt, and K. Michielsen: 'Support vector machines on the D-Wave quantum annealer'. *Computer Physics Communications* (Mar. 2020), vol. 248: p. 107006 (cit. on p. 1).

[Xue22] Xue, X., M. Russ, N. Samkharadze, B. Undseth, A. Sammak, G. Scappucci, and L. M. K. Vandersypen: 'Quantum logic with spin qubits crossing the surface code threshold'. *Nature* (Jan. 2022), vol. 601(7893): pp. 343–347 (cit. on pp. 9, 73).

[Yan20] Yang, C. H., R. C. C. Leon, J. C. C. Hwang, A. Saraiva, T. Tanttu, W. Huang, J. Camirand Lemyre, K. W. Chan, K. Y. Tan, F. E. Hudson, K. M. Itoh, A. Morello, M. Pioro-Ladrière, A. Laucht, and A. S. Dzurak: 'Operation of a silicon quantum processor unit cell above one kelvin'. *Nature* (Apr. 2020), vol. 580(7803): pp. 350–354 (cit. on p. 9).

[Yon18] Yoneda, J., K. Takeda, T. Otsuka, T. Nakajima, M. R. Delbecq, G. Allison, T. Honda, T. Kodera, S. Oda, Y. Hoshi, N. Usami, K. M. Itoh, and S. Tarucha: 'A quantum-dot spin qubit with coherence limited by charge noise and fidelity higher than 99.9 %'. *Nature Nanotechnology* (Feb. 2018), vol. 13(2): pp. 102–106 (cit. on pp. 9, 10, 73, 76, 110).

[Yu22] Yu, C. X., S. Zihlmann, J. C. Abadillo-Uriel, V. P. Michal, N. Rambal, H. Niebojewski, T. Bedecarrats, M. Vinet, E. Dumur, M. Filippone, B. Bertrand, S. De Franceschi, Y.-M. Niquet, and R. Maurand: 'Strong coupling between a photon and a hole spin in silicon'. *Nature Nanotechnology* (June 2022), vol.: pp. 1–24 (cit. on pp. 11, 34).

[Zha18] Zhao, R., T. Tanttu, K. Y. Tan, B. Hensen, K. W. Chan, J. C. C. Hwang, R. C. C. Leon, C. H. Yang, W. Gilbert, F. E. Hudson, K. M. Itoh, A. Morello, A. Laucht, and A. S. Dzurak: 'Coherent single-spin control with high-fidelity singlet-triplet readout in silicon'. (2018), vol.: pp. 1–11 (cit. on p. 73).

[Zha19] Zhao, R. et al.: 'Single-spin qubits in isotopically enriched silicon at low magnetic field'. *Nature Communications* (Dec. 2019), vol. 10(1): p. 5500 (cit. on p. 38).

[Zu22] Zu, H., W. Dai, and A. de Waele: 'Development of dilution refrigerators—A review'. *Cryogenics* (Jan. 2022), vol. 121: p. 103390 (cit. on p. 42).

[Zwa13] Zwanenburg, F. A., A. S. Dzurak, A. Morello, M. Y. Simmons, L. C. L. Hollenberg, G. Klimeck, S. Rogge, S. N. Coppersmith, and M. A. Eriksson: 'Silicon quantum electronics'. *Reviews of Modern Physics* (2013), vol. 85(3): pp. 961–1019 (cit. on pp. 13, 77).

[Zwe22] Zwerver, A. M. J. et al.: 'Qubits made by advanced semiconductor manufacturing'. *Nature Electronics* (Mar. 2022), vol. 5(3): pp. 184–190 (cit. on pp. 10, 11, 73, 100, 110).

List of Figures

1.1 Bloch Sphere . . . 3
1.2 Qubit realizations . . . 6
1.3 Silicon spin qubits: State of the art . . . 10
1.4 CMOS spin qubits . . . 11

2.1 Electrostatic model of a single quantum dot . . . 15
2.2 Transport through a single quantum dot. . . . 17
2.3 Electrostatic model of a double quantum dot. . . . 18
2.4 Stability diagram in different regimes. . . . 21
2.5 Charge sensing via a QPC and a SET . . . 24
2.6 Energy band diagram of two spins in a double quantum dot . . . 27
2.7 Energy selective spin readout . . . 29
2.8 Schematic of PSB. . . . 30

3.1 Lithography and Lift-off process . . . 33
3.2 Industrial process . . . 36
3.3 Academic process . . . 38
3.4 Post-processing . . . 42
3.5 Measurement setup . . . 49

4.1 Design Hall bar . . . 54
4.2 Design quantum dots . . . 55
4.3 Transistor characteristics . . . 57
4.4 Setup Hall bar . . . 59
4.5 4 terminal resistance . . . 60
4.6 SdH oscillations and conductance plateaus . . . 62
4.7 SdH oscillations for different gate voltages . . . 64
4.8 Sheet resistance and transversal resistance plotted against the magnetic field and the gate voltage . . . 66
4.9 Gate voltage, electron density and electron mobility . . . 67
4.10 Localization effects . . . 68
4.11 Charge stability . . . 70

5.1 Device design . . . 77
5.2 Charge characterization . . . 80
5.3 Fidelity analysis . . . 82
5.4 Measurement window . . . 83

5.5 Spin relaxation 88
5.6 Larmor precession and micro-magnet hysteresis 91
5.7 Rabi oscillations. 93
5.8 Rabi oscillations for different input powers. 94
5.9 Valley enhanced EDSR 96
5.10 Theory valleys 99
5.11 Population for non resonant driving and correlation to the Rabi frequency . 102
5.12 Larmor spectroscopy 103
5.13 Coherence times 105

List of Tables

4.1 Comparison to the Literature 71

Acknowledgments

First of all, I would like to thank Tristan for giving me the opportunity to join the QuantECA team and the quantum silicon project in Grenoble. I would also like to thank Matias for co-supervising my thesis and many insight full discussions throughout my thesis, as well as Vivien for guiding me in the beginning and getting me started in the clean room. Further, I would like thank Dominique Bougeard and Takis Kontos for reviewing my manuscript. Anasua Chatterjee and Philippe Galy for being examiners and Mairbek Chshiev for taking the role of the president of the jury. I would also like to acknowledge the QuEnG and GreQuE program (G.A. No 754303) for the financial support.
The realization of this thesis would have not been possible without the administrative and technical services of Institut Néel. First, I would like to thank Florence Pois, Anne-Laure Jaussent and Angélique Simones for navigating me through the abyss of French bureaucracy. On the side of technical services, I would like to thank the team of the mechanical workshop and the pole cyogenie for their work. The electronics workshop, in particular Christophe Guttin for all the custom made hardware and their support with any broken device we have. To the team of the liquefier for enabling me to keep my experiment cold for more than one year. A special thank you goes out to the team Nanofab and everyone that I have met in the clean room. A big thank you goes to Thierry for all the support with the Nanobeam and for evaporating the best Nb, to Bruno for keeping the evaprators running and all the HF dips, to Latifa for countless HF dips and for keeping the Nanochemie alive, to Gwénaëlle for your help with the RIE and the scriber and to Jeff for support with the SEM and for the organization. In addition, I would like to thank the team of PTA and BCAi for their support, in particular Irène for dicing countless samples for us.
To Mikael, Eduardo, Laurianne and Quentin who gave me a warm welcome in the LETI Characterization lab during my industrial internship. To Biel and Yann-Michel for theoretical support and useful discussions. Mikael and Romain for being a very nice, encouraging and helpful comité de suivi de thèse.
A big thank you to all present and former team members in Bat. M and Bat. V. and whoever I missed. In particular I would like to thank my office mates Bruna, Victor, Pierre, David, Martin S. and Everton for all the discussions on and off topic.
To Farshad for welcoming me in beginning and countless via ferratas. To Hermann for introducing me to rock climbing and all the bonfires. To Marco, Dennis and Dina the members of the Sauerbratengruppe for keeping me entertained weekly and welcoming me in Hamburg and Erftstadt. To Michael and Luca for keeping me up to date about Aachen and for our great bike tour. To my father and my sister for always supporting me and listening to all the obscure problems that I faced during my PhD.
Most importantly, I would like to dedicate this thesis to Margarita for her love, support and for building our future together.